

# Transition Metal Borides: Synthesis, Characterization and Superconducting Properties



TECHNISCHE  
UNIVERSITÄT  
DARMSTADT

Vom Fachbereich Chemie  
der Technischen Universität Darmstadt

zur Erlangung des akademischen Grades eines

Doctor rerum naturalium (Dr. rer. nat.)

genehmigte

Dissertation

vorgelegt von

MSc. Mehmet Kayhan  
aus Bursa, Türkei

Referent: Prof. Dr. Barbara Albert  
Korreferent: Prof. Dr. Rolf Schäfer

Tag der Einreichung: 03. Juni 2013  
Tag der mündlichen Prüfung: 12. Juli 2013

Darmstadt 2013  
D17

---



---

*To my daughter, my wife and my parents*

---

## ACKNOWLEDGEMENT

I express my sincere gratitude towards Prof. Barbara Albert for allowing me to be a part of her research group and closely following my work during the course of my doctoral thesis with her inspiring suggestions and discussions. I am grateful to her for the constant motivation throughout this period and her support and help in professional as well as personal life.

I appreciate the help of Dr. Kathrin Hofmann for the structure analysis with Rietveld refinement despite of her busy schedule. I'm indebted to Dr. Christian F. Litterscheid for his invaluable time, help and support through my studies. I am also thankful to all of my group members for their friendship, scientific comments and suggestions.

I reserve my special thanks to Prof. Lambert Alff and Erwin Hildebrandt for the collaboration work on superconductivity measurements. I would like to also thank Dr. Anatoliy Senyshyn for neutron diffraction analysis and Dr. Dmytro Dzivenko for hardness measurements.

I would like to keep the most special thanks to Emine Kayhan as my colleague, friend and my eternal love who did SEM-EDX measurements for me and as always, has given me endless love and support throughout my life.

I would like to thank my parents and all my family for their endless love and moral support during my stay in Germany.

And last but not least, I want to thank my daughter Ikra Asya Kayhan. With her, I experienced the biggest happiness that a man can ever feel. She has been my regeneration gemstone through this challenging level of my life.

---

### Results from this work already published

“Neutron diffraction and observation of superconductivity for tungsten borides, WB and W<sub>2</sub>B<sub>4</sub>” Kayhan M., Hildebrandt E., Frotscher M., Senyshyn A., Hofmann K., Alff L., Albert B.\* *Solid State Sciences*, 14, **2012**, 11–12, 1656-1659.

### Conferences presentation

September 17-19, 2012 16th Conference of the GDCh Division for Solid State Chemistry and Materials Research, Darmstadt, Germany (poster presentation)

September 11-17, 2011 International Symposium on Boron, Borides and Related Materials in Istanbul, Turkey (oral presentation, session-chair)

August 8-21, 2010 Summer School on Preparative Strategies in Solid State and Materials Chemistry at University of California Santa Barbara, Santa Barbara, United States (poster presentation)

---

## Abstract

### Transition Metal Borides: Synthesis, Characterization and Superconducting Properties

A systematic study was done on the synthesis and superconducting properties of metal-rich transition metal borides. Five different binary systems were investigated including the boride systems of niobium, tantalum, molybdenum, tungsten and rhenium. High-temperature solid state methods were used in order to synthesize samples of different transition metal borides of the composition  $M_2B$ ,  $MB$ ,  $M_3B_2$ ,  $MB_2$ , and  $M_2B_4$ . The reactions were carried out in three different furnaces with different sample containers: the electric arc (copper crucible), the high frequency induction furnace (boron nitride, tantalum or glassy carbon crucibles), and the conventional tube furnace (sealed evacuated quartz ampoules).

The products obtained were characterized with X-ray powder diffractometry, scanning electron microscopy and energy-dispersive X-ray spectroscopy. Phase analyses and crystal structure refinements using the Rietveld method and based on structure models known from literature were performed. A neutron diffraction measurement was done for  $W_2B_4$  to allow for a complete crystal structure determination, because of the presence of a heavy element like tungsten and a light element like boron that made it difficult to determine the accurate determination of the boron atom positions and occupancies from X-ray data. A new structure model for  $W_2B_4$  was proposed.

Magnetic measurements in a SQUID magnetometer down to temperatures as low as 1.8 K were performed to several of the products in order to see if the transition metal borides become superconducting at low temperatures, and the results were compared with data from literature. Superconducting properties were found for the following compounds:  $NbB_2$  ( $T_C = 3.5$  K),  $\beta$ - $MoB$  ( $T_C = 2.4$  K),  $\beta$ - $WB$  ( $T_C = 2.0$  K),  $\alpha$ - $WB$  ( $T_C = 4.3$  K),  $W_2B_4$  ( $T_C = 5.4$  K),  $Re_7B_3$  ( $T_C = 2.4$  K).

A relationship between the superconducting properties and the compositional and structural features was discussed for metal diborides. Also it was found that there is an influence of particle sizes on the superconductivity of  $WB$  and  $W_2B_4$ .

---

## Kurzzusammenfassung

### Übergangsmetallboride: Synthese, Charakterisierung und supraleitenden Eigenschaften

Eine systematische Studie über die Synthese und die supraleitenden Eigenschaften von metall-reichen Übergangsmetallboriden wurde durchgeführt. Fünf verschiedene binäre Systeme der Boride von Niob, Tantal, Molybdän, Wolfram und Rhenium wurden hierzu untersucht. Proben von verschiedenen Übergangsmetallboriden der allgemeinen Zusammensetzungen  $M_2B$ ,  $MB$ ,  $M_3B_2$ ,  $MB_2$  und  $M_2B_4$  wurden mittels Hochtemperatur-Festkörper-Synthesen dargestellt. Die Reaktionen wurden in drei unterschiedlichen Ofentypen mit verschiedenen Tiegelmaterien durchgeführt: elektrischer Lichtbogenofen (Kupfertiegel), Hochfrequenz-Induktionsofen (Bornitrid-, Tantal- oder Glaskohlenstofftiegel) sowie gebräuchliche Rohröfen (geschlossene evakuierte Quarzampullen).

Die erhaltenen Produkte wurden mittels Röntgenpulverdiffraktometrie, Rasterelektronenmikroskopie und energiedisperser Röntgenspektroskopie charakterisiert. Phasenanalysen und Kristallstruktur Verfeinerungen basierend auf bekannten Strukturmodellen aus der Literatur wurden mit der Rietveld-Methode durchgeführt.

Eine Neutronenbeugungsmessung wurde an  $W_2B_4$  durchgeführt, die eine vollständige Bestimmung der Kristallstruktur ermöglichte. Die Messung war notwendig, da die akkurate Bestimmung von Bor-Atompositionen und Besetzungsfaktoren bei Anwesenheit eines schweren Elements, wie Wolfram, anhand von Röntgenbeugungsdaten schwierig ist. Ein neues Struktur Modell für  $W_2B_4$  wurde vorgeschlagen.

Mit einem SQUID-Magnetometer wurden bei Temperaturen herab bis zu 1,8 K an einigen der Produkte magnetische Messungen durchgeführt, um zu sehen, ob diese Übergangsmetallboride bei niedrigen Temperaturen supraleitend werden. Die Ergebnisse wurden mit Daten aus der Literatur verglichen.

Supraleitende Eigenschaften wurden für die folgenden Verbindungen gefunden:  $NbB_2$  ( $T_C = 3,5$  K),  $\beta$ - $MoB$  ( $T_C = 2,4$  K),  $\beta$ - $WB$  ( $T_C = 2,0$  K),  $\alpha$ - $WB$  ( $T_C = 4,3$  K),  $W_2B_4$  ( $T_C = 5,4$  K),  $Re_7B_3$  ( $T_C = 2,4$  K).

Ein Zusammenhang zwischen den supraleitenden Eigenschaften, der Zusammensetzung und den Strukturmerkmalen wurde für die Metaldiboride diskutiert. Es wurde auch festgestellt, dass es einen Einfluss der Partikelgröße auf die Supraleitung von  $WB$  und  $W_2B_4$  gibt.

<b>1. INTRODUCTION.....</b>	<b>1</b>
<b>2. PREPARATION METHODS.....</b>	<b>3</b>
2.1. SCHLENK (VACUUM-ARGON) LINE.....	3
2.2. ARC MELTING .....	3
2.2.1. <i>General</i> .....	3
2.2.2. <i>Sample preparation for arc melting</i> .....	5
2.3. REACTIONS IN SEALED QUARTZ AMPOULES .....	7
2.3.1. <i>General</i> .....	7
2.3.2. <i>Sample preparation for reactions in quartz ampoules</i> .....	8
2.4. HIGH FREQUENCY INDUCTION FURNACE .....	8
2.4.1. <i>General</i> .....	8
2.4.2. <i>Working principle of the high frequency induction furnace</i> .....	9
2.4.3. <i>Sample preparation for the high frequency induction furnace</i> .....	9
<b>3. CHARACTERIZATION AND ANALYSIS TECHNIQUES .....</b>	<b>11</b>
3.1. X-RAY DIFFRACTION .....	11
3.2. NEUTRON DIFFRACTION.....	14
3.3. CRYSTAL STRUCTURE ANALYSIS .....	15
3.4. SUPERCONDUCTIVITY MEASUREMENTS .....	16
3.4.1. <i>General</i> .....	16
3.4.2. <i>Sample preparation for superconductivity measurements</i> .....	18
3.5. MORPHOLOGICAL ANALYSIS VIA SCANNING ELECTRON MICROSCOPY .....	19
<b>4. METAL-RICH TRANSITION METAL BORIDES.....</b>	<b>20</b>
4.1. GENERAL.....	20
4.2. STRUCTURES OF TRANSITION METAL BORIDES.....	20
4.3. NIOBIUM-BORON SYSTEM .....	28
4.3.1. <i>Phase diagram of the Nb-B system</i> .....	28
4.3.2. <i>Literature review</i> .....	29
4.3.3. <i>Synthesis and structural characterization of Nb<sub>3</sub>B<sub>2</sub></i> .....	30
4.3.4. <i>Synthesis, structural characterization and superconductivity measurements of NbB</i> .....	33
4.3.5. <i>Synthesis and structural characterization of Nb<sub>5</sub>B<sub>6</sub></i> .....	36
4.3.6. <i>Synthesis, structural characterization and superconductivity measurements of NbB<sub>2±x</sub></i> ....	39
4.3.7. <i>Concluding remarks on the Nb-B system</i> .....	44
4.4. TANTALUM-BORON SYSTEM .....	46
4.4.1. <i>Phase diagram of the Ta-B system</i> .....	46
4.4.2. <i>Literature review</i> .....	47

4.4.3.	<i>Synthesis and structural characterization of Ta<sub>2</sub>B</i> .....	48
4.4.4.	<i>Synthesis, structural characterization and superconductivity measurements of TaB</i> .....	50
4.4.5.	<i>Synthesis and structural characterization of Ta<sub>3</sub>B<sub>4</sub></i> .....	53
4.4.6.	<i>Synthesis, structural characterization and superconductivity measurements of TaB<sub>2±x</sub></i> .....	55
4.4.7.	<i>Concluding remarks on the Ta-B system</i> .....	60
4.5.	MOLYBDENUM-BORON SYSTEM .....	62
4.5.1.	<i>Phase diagram of the Mo-B system</i> .....	62
4.5.2.	<i>Literature review</i> .....	63
4.5.3.	<i>Synthesis, structural characterization and superconductivity measurements of Mo<sub>2</sub>B</i> .....	64
4.5.4.	<i>Synthesis, structural characterization and superconductivity measurements of β-MoB</i> ....	66
4.5.5.	<i>Synthesis, structural characterization and superconductivity measurement of α-MoB</i> .....	69
4.5.6.	<i>Synthesis, structural characterization and superconductivity measurement of Mo<sub>2</sub>B<sub>4</sub></i> .....	72
4.5.7.	<i>Synthesis, structural characterization and superconductivity measurements of MoB<sub>2</sub></i> .....	77
4.5.8.	<i>Concluding remarks on Mo-B system</i> .....	80
4.6.	TUNGSTEN-BORON SYSTEM .....	81
4.6.1.	<i>Phase diagram of the W-B system</i> .....	81
4.6.2.	<i>Literature review</i> .....	82
4.6.3.	<i>Synthesis, structural characterization and superconductivity measurements of β-WB</i> .....	83
4.6.4.	<i>Synthesis, structural characterization and superconductivity measurements of α-WB</i> .....	86
4.6.5.	<i>Synthesis, structural characterization and superconductivity measurements of W<sub>2</sub>B<sub>4</sub></i> .....	90
4.6.6.	<i>Concluding remarks on the W-B system</i> .....	97
4.7.	RHENIUM-BORON SYSTEM .....	99
4.7.1.	<i>The phase diagram of the Re-B system</i> .....	99
4.7.2.	<i>Literature review</i> .....	100
4.7.3.	<i>Synthesis and structural characterization of Re<sub>3</sub>B</i> .....	100
4.7.4.	<i>Synthesis, structural characterization and superconductivity measurements of Re<sub>7</sub>B<sub>3</sub></i> ...	102
4.7.5.	<i>Synthesis, structural characterization and superconductivity measurements of ReB<sub>2</sub></i> .....	104
4.7.6.	<i>Concluding remarks on the Re-B system</i> .....	106
4.8.	CORRELATION BETWEEN THE CRYSTAL STRUCTURES AND SUPERCONDUCTING PROPERTIES OF DIBORIDES.....	107
5.	<b>SUMMARY AND OUTLOOK</b> .....	<b>109</b>
6.	<b>REFERENCES</b> .....	<b>111</b>



---

## 1. Introduction

---

Borides are a very large group of compounds composed of boron and a less electronegative element without containing oxygen in the system. They have high melting points and non-ionic properties. Borides can have very useful physical, chemical and mechanical properties like high chemical stability, high hardness and good thermoelectric properties. Borides can be classified in two groups as metal-rich and boron-rich borides. If the boron to metal ratio is 4:1 or higher than that, it is called boron-rich and if it is less, then it is called metal-rich boride.

Typical physical properties of borides can be high melting points, high hardnesses, low thermal conductivities, and high Seebeck coefficients <sup>[1] [2] [3] [4] [5]</sup>. In addition to those properties many borides have chemical inertness, and interesting magnetic and electrical properties <sup>[6] [7] [8] [9] [10]</sup>.

The discovery of superconductivity of magnesium diboride ( $\text{MgB}_2$ ) with a  $T_c = 39 \text{ K}$  <sup>[11]</sup> attracted researchers to investigate certain borides, especially those that have a similar structure like  $\text{MgB}_2$ . The planar structure of hexagonally ordered boron atoms is believed to have a big influence on the superconductivity in  $\text{MgB}_2$  <sup>[12]</sup>. In metal boride systems there are many binary borides that crystallize with the same structure, called  $\text{AlB}_2$ -type. It can be expected to see a correlation between structural changes and superconductivity also for the metal-rich transition metal borides. There are some reports on the superconductivities of different transition metal borides but a systematical investigation of the binary systems is still missing <sup>[13] [14] [15]</sup>.

In this work, five different binary phase systems of borides of transition metals, niobium, tantalum, molybdenum, tungsten and rhenium, were investigated in terms of synthesis, structural characterization and superconducting properties. Three different methods were used to synthesize the samples: arc-melting, reaction in quartz ampoules and synthesis in a high frequency induction furnace. Crystal structures were investigated using X-ray and neutron diffraction data.

Superconductivity measurements were carried out using a superconducting quantum interference device (SQUID). Superconductivity was observed for the first time for some of the borides investigated. The relationship between superconductivity and crystal

---

---

structure was examined by comparing the relative change in unit cell parameters and transition temperatures ( $T_C$ ). Moreover, the influence of particle sizes on superconductivity was investigated for WB and  $W_2B_4$ .

---

## 2. Preparation methods

---

### 2.1. Schlenk (vacuum-argon) line

Most of the steps of the preparation of metal borides were carried out under inert atmosphere in order to prevent reaction with oxygen or water <sup>[16] [17]</sup>. A schlenk line (invented by Wilhelm Schlenk) was used to handle air-sensitive compounds. The schlenk line is a double manifold of integrated vacuum and argon lines that are connected by double oblique valves giving the opportunity to the user to switch between vacuum and argon when necessary. The line is formed of glass pieces that are connected via tightly fitting and high vacuum greased ground glass joints. Vacuum of  $10^{-3}$  mbar is achieved by the rotary valve vacuum pump connected to the line via a metal bellows tube and the pressure read-out is established by the vacuum gauge connected to the system. A liquid nitrogen trap is used between the vacuum pump and the schlenk line to prevent the contamination of the pump. In order to prevent the possible oxidation of the sample connected to the schlenk line, prior to the introduction of argon to the line, it is purified by passing through four towers. These contain in sequence silica gel, potassium hydroxide, molecular sieve (mesh size 3) and phosphorus pentoxide that eliminate the impurities in the argon gas. Afterwards, argon flows through a quartz glass tube filled with titanium sponge of which temperature is kept at 700 °C in a tube oven. By this way, remaining humidity, oxygen and nitrogen are eliminated from argon.

### 2.2. Arc Melting

#### 2.2.1. General

Reaction of solids in an electric arc furnace is a widely used method in solid state chemistry for high temperature experiments, especially when temperatures higher than 2000 °C are needed <sup>[18] [19]</sup>. It is a very practical, quick and powerful method. It is possible to reach temperatures higher than 3000 °C in a time as short as a few seconds. While in conventional high furnaces energy is consumed to heat the inner volume of the furnace which is then used for the reaction, in arc melting the energy is directly heating the reactants because the electrical current passes through the charged material between the electrodes of the furnace.

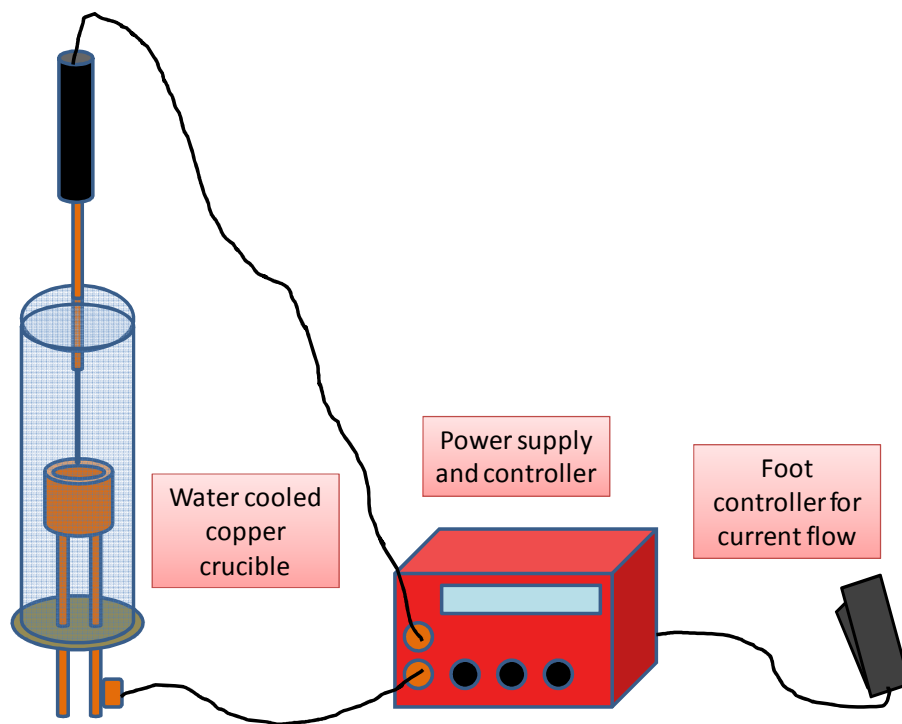


Figure 1: Scheme of a laboratory type arc melting apparatus.

In an arc furnace the power supply is connected to a welding electric rectifier and the power can be controlled by a foot pedal during the melting process. The welding rectifier is located in an air tight reaction chamber which is made out of Duran glass. The electrical arc is formed between the tungsten electrode and the copper crucible which is water cooled. The whole reaction chamber is connected to a schlenk line and the reaction takes place under slight vacuum with 0.7 bar argon pressure. As well as the copper crucible, the glass chamber is surrounded with a water cooling section. In addition to water cooling, a quartz tube is used as a protection shield for the glass chamber during the reaction.

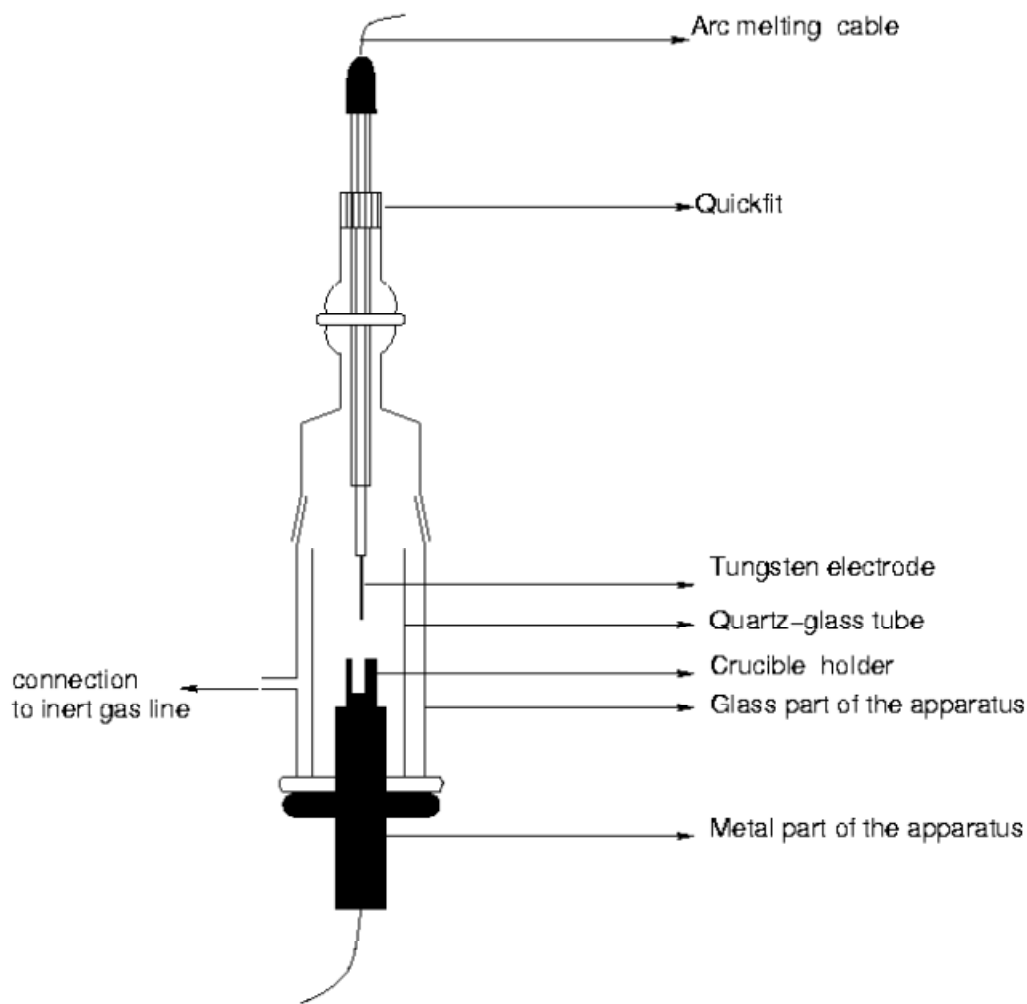


Figure 2: Arc melting reaction chamber <sup>[16]</sup>

### 2.2.2. Sample preparation for arc melting

Elemental powders were used as reactants for the synthesis of various borides in varying stoichiometric ratios. The powders were mixed in a weighing boat by shaking for a few minutes. Shaking in a weighing boat was preferred over mixing by using a mortar or a ball mill in order to prevent the loss of any of the reactants which might cause a change in the stoichiometry. This change can be dramatic since the total amount of the reactants was about 250 mg and the molar mass difference between the metal and boron is very large.

Mixed powders were then pressed into pellets with a load of five tons on a five mm diameter cylindrical pressing tool for about five minutes. The pellet was placed in the

---

copper crucible and then sealed in the reaction chamber. The chamber was evacuated and filled with argon and then evacuated again. This flushing process was repeated for three times to get rid of traces of oxygen and water vapor in the chamber. After the third cycle of flushing, the pressure in the chamber was set to 0.7 bars of argon.

The sample was melted in the arc directly on the sample until it became a molten sphere. The melting process was repeated for at least three times with turning the sample around in between each melting process to assure homogeneity. At the end of the third melting process the chamber was filled with argon and the sample was taken out after cooling. If a slightly slower cooling rate is desired, the venting step can be delayed since the heat transfer between the sample and the surroundings is much slower under vacuum. The final product is in the shape of a sphere and some of the samples exhibit a faceted surface (Figure 3).

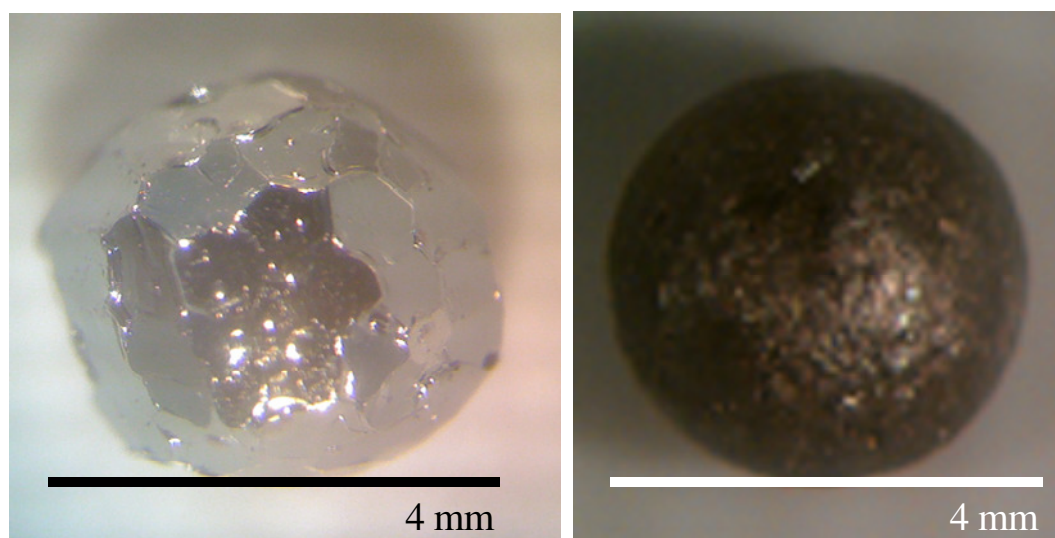


Figure 3: Products of arc melting procedure with varying surfaces.

The samples were then ground in a boron carbide mortar or by using a tungsten carbide ball mill to get fine powders for further characterization.

---

## 2.3. Reactions in sealed quartz ampoules

### 2.3.1. General

In solid state chemistry conventional high temperature furnaces are widely used. Especially with air or moisture sensitive samples, a protective reaction chamber is needed<sup>[20]</sup>. For this purpose, sealed quartz ampoules were used in this work.

The reactants were put into the quartz tube and then the tube was heated with a hydrogen-oxygen flame in order to reduce the diameter of the tube and taper it. By pulling, a capillary was made in the middle of the tube. Then the tube was connected to a schlenk line and the reactants were filled in the ampoule. After evacuating and flushing with argon the ampoule was sealed by closing the capillary while being connected to the schlenk line. In Figure 4, a sample in a sealed quartz ampoule can be seen.



Figure 4: Quartz ampoule with sample.

High temperature reactions between solids are based on diffusion. Since the reactants are powders it takes a lot of time to diffuse into each other. In order to accelerate the diffusion process, iodine was used as a mineralizer. Iodine reacts with boron to form boron iodide which goes into gas phase at high temperatures. Boron iodide then reacts with the metal powder to form the desired metal boride. At the end of the reaction  $\text{BI}_3$  crystallizes at the cold end of the ampoule. In order to keep the stoichiometry in the desired range it is crucial to use some excess boron in the starting mixture. In Figure 4 crystals of  $\text{BI}_3$  can be seen at the right side of the ampoule.

---

### 2.3.2. Sample preparation for reactions in quartz ampoules

The powders were mixed in a weighing boat by shaking for a few minutes. In order to increase the interaction between the reactants physically, the mixture of boron and metal powders was pressed into pellets as described in 2.2.2. Pellets or un-pressed mixtures (in case of reactions under addition of iodine) of powders were put into quartz tubes.

After sealing the ampoule it was put into the furnace. The samples were heated up to 1050 °C and kept at that temperature for three to seven days. At the end of the reaction time, the sample was cooled down to room temperature and the ampoule was cut and opened. The products were then washed with acetone several times till the yellow color of the iodine disappeared from the filter paper. The final product was then ready for characterization after drying in the oven.

## 2.4. High frequency induction furnace

### 2.4.1. General

The induction furnace, as can be understood by the name itself, heats the material without contact by induction. This clean and non-contact process gives the opportunity to use the furnace in a vacuum or inert atmosphere and enables the production of air sensitive samples e.g. alloys <sup>[21] [22] [23]</sup>.

Induction furnace is extensively used in clean, efficient and controlled heating applications of metals and non-metals. Heating of the anti-tamper caps of medicine or drink bottles to seal them is one of the most common applications <sup>[24]</sup>. Besides, ultra-high temperature carbon composites production, brazing, welding and melting of metals are just some other applications of induction heating.

For the implementation of induction heating, a high frequency electrical power source, an alternating magnetic field generator surrounding refractory material and an electrically conductive material to be heated are the main requirements. For nonconductive materials, the sample is placed into metal crucibles to be heated. Besides, a water or air cooling system is also essential to remove waste heat from the work coil.

---

Herein, we report on experiments performed in a high frequency induction furnace equipped with an air-cooling system which can be modified with a water-cooling system as well. The advantage of the high frequency induction furnace among the other techniques in our case is that heating and melting of the samples were achieved in a controllable way at the high temperatures.

#### **2.4.2. Working principle of the high frequency induction furnace**

In the induction heating process an electrical conducting material is heated by electromagnetic induction. A high frequency electrical power source supplies an alternating electric current flowing into a furnace through the copper coils surrounding the refractory material. So, the electromagnetic field is generated and penetrates the reaction chamber which is under argon atmosphere. Upon coupling with conductive material (metal crucible or the sample itself) inside the furnace, an electric current inside the sample is induced. That leads to heat production inside the metal and increase of the temperature rapidly to the set point value. As the frequency of the alternating current increases, the amount of power applied to a furnace increases as well. So, the melting occurs faster or the set point temperature value is reached more quickly.

#### **2.4.3. Sample preparation for the high frequency induction furnace**

The powders were mixed in a weighing boat by shaking for a few minutes. The mixtures of boron and metals were pressed into pellets as for the arc melting. The pellet or the mixture of the powders was put into boron nitride crucibles to prevent interaction of the reactants with the surroundings. BN is not reacting with metal and boron powders and not heated in the magnetic field. The BN crucible was put into a tantalum or a glassy carbon crucible which can be heated and transfers the heat to the sample. The reaction chamber was flushed with argon and kept under slight vacuum at about 0.7 bars in argon atmosphere.

The sample was heated and cooled according to a heating profile ramp. During heating the temperature is controlled by changing the applied current. The current is increased step by step from three amperes which is the lower limit for the set-up used, to the desired level with steps of 0.5 amperes every three to five minutes. The temperature of the system is checked with a non-contact laser thermocouple. The maximum

---

temperatures were about 1800 °C to 2200 °C depending on the temperature range of the desired product. When the desired temperature was reached, the sample was kept at that temperature for one to five hours which was followed by a quick cooling at three amperes decrease per minute.

---

### 3. Characterization and analysis techniques

---

#### 3.1. X-ray diffraction

X-rays are produced by accelerated electrons to strike a metal cathode. By this collision, they ionize some of the electrons in the shell. After the removal of a 1s electron from the inner part of the shell 2p outer electrons fall into that lower energy state and loose some of their energy. That energy loss is observed as X-ray radiation which is specifically called  $K\alpha$  radiation.

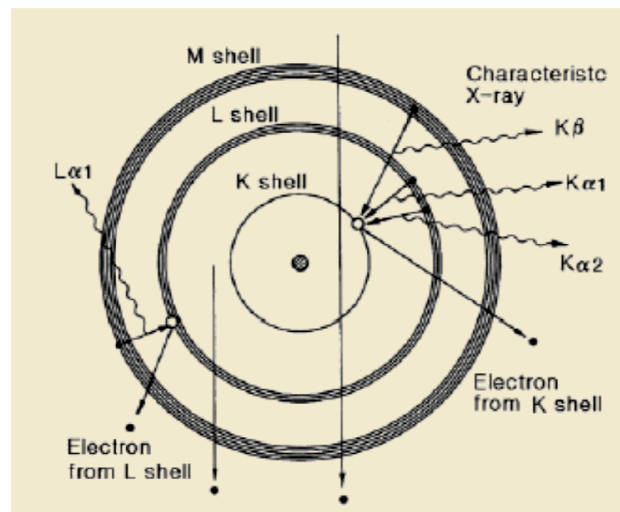


Figure 5: Generation of X-rays

In the working principle of the X-ray diffraction, X-rays are directed to the sample after being diffracted at a monochromator in order to select the wavelength and then hit on the sample. The incoming X-ray beam scatters from atoms as waves. Since crystals are composed of orderly repeating small segments which are called unit cells, this order causes a constructive interference of diffracted X-rays as waves and creates a pattern.

---

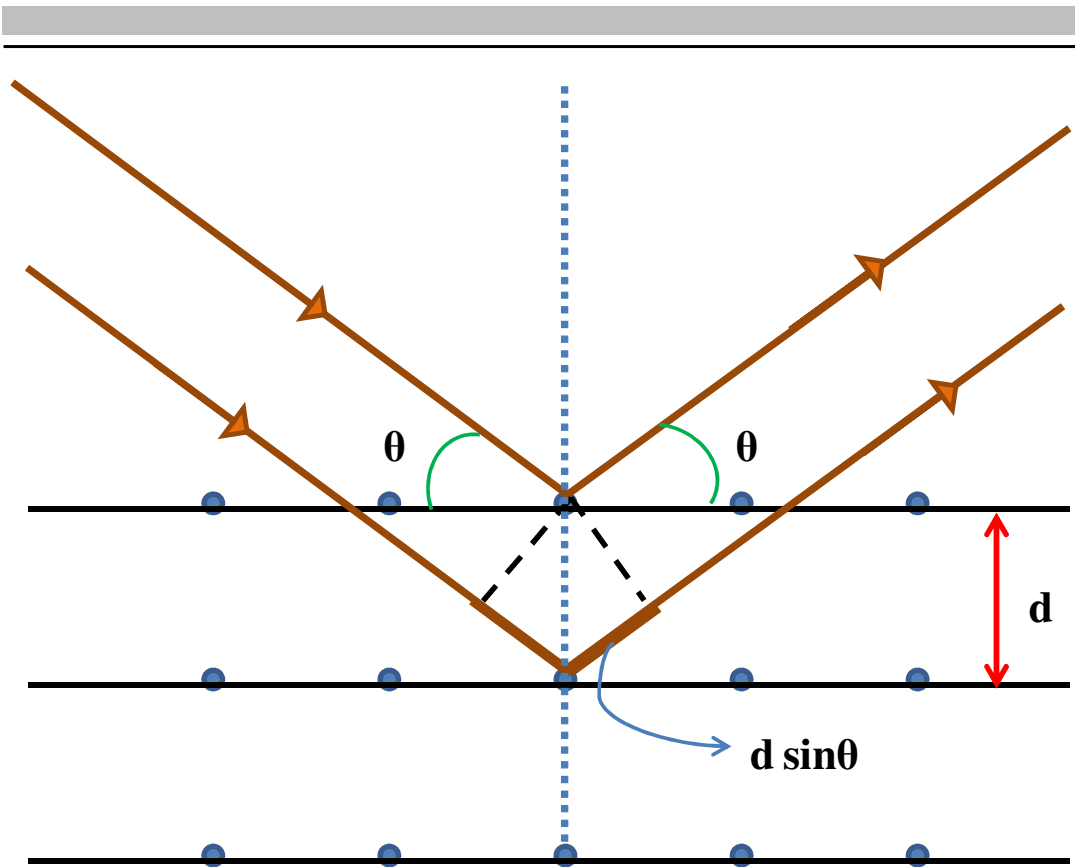


Figure 6: Bragg geometry for the diffraction

If the atoms are in a systematically ordered structure then the scattered waves interfere constructively only in directions where their path-length difference  $2d \sin \theta$  equals an integer multiple of the wavelength  $\lambda$  in accordance to Bragg's law and the incoming beam is deflected by an angle  $2\theta$ , producing a reflection spot in the diffraction pattern. Bragg's law can be formulated as:

$$2 d \sin \theta = n \lambda$$

where:

- $d$  is the distance between lattice planes;
- $\theta$  is the diffraction angle;
- $n$  is the order of diffraction;
- $\lambda$  is the wavelength ;

---

The X-ray diffraction method is one of the most important characterization methods especially for inorganic materials. X-rays are useful because of their wavelength is about 1 Å which is very close to inter-atomic distances in a crystal. Each material has its own characteristic  $d$  spacings between different planes which causes different characteristic diffraction patterns.

If the sample is an unknown compound or in other words a new phase, the lattice parameters and the crystal symmetry as well as the crystal structure can be determined very accurately.

Diffraction patterns are like fingerprints for each material. If the compound which is subject to the analysis is already described in literature, then just by comparing the observed pattern with the data from PDF <sup>[25]</sup> database a qualitative analysis can be done and the sample can be analyzed in terms of number of phases, impurities and crystallinity. Crystal size can be analyzed by using the Scherrer equation <sup>[26] [27]</sup>.

The Scherrer equation can be written as:

$$\tau = \frac{K \lambda}{\beta \cos\theta}$$

where:

- $\tau$  is the mean size of the ordered (crystalline) domains, which may be smaller or equal to the grain size;
- $K$  is a dimensionless shape factor, with a value close to unity. The shape factor has a typical value of about 0.9, but varies with the actual shape of the crystallite;
- $\beta$  is the line broadening at half of the maximum intensity (FWHM), after subtracting the instrumental line broadening, in radians;

X-ray diffraction measurements were performed in transmission mode using a powder diffractometer (STOE Stadi P) with a linear position sensitive detector, a Germanium monochromator, copper radiation ( $\lambda = 1.540598 \text{ \AA}$ ) and a flat plate sample holder.

### 3.2. Neutron diffraction

Neutron diffraction is a powerful and accurate analysis technique to elucidate the structural properties of crystalline materials. It is widely used as a supporting technique to X-ray diffraction in order to determine the crystal structure. Neutron diffraction has some advantages compared to X-ray diffraction. Due to the great penetrating power of neutrons, complicated sample environments can be handled and the full sample can be analyzed. Neutron diffraction is much more sensitive to light elements like boron.

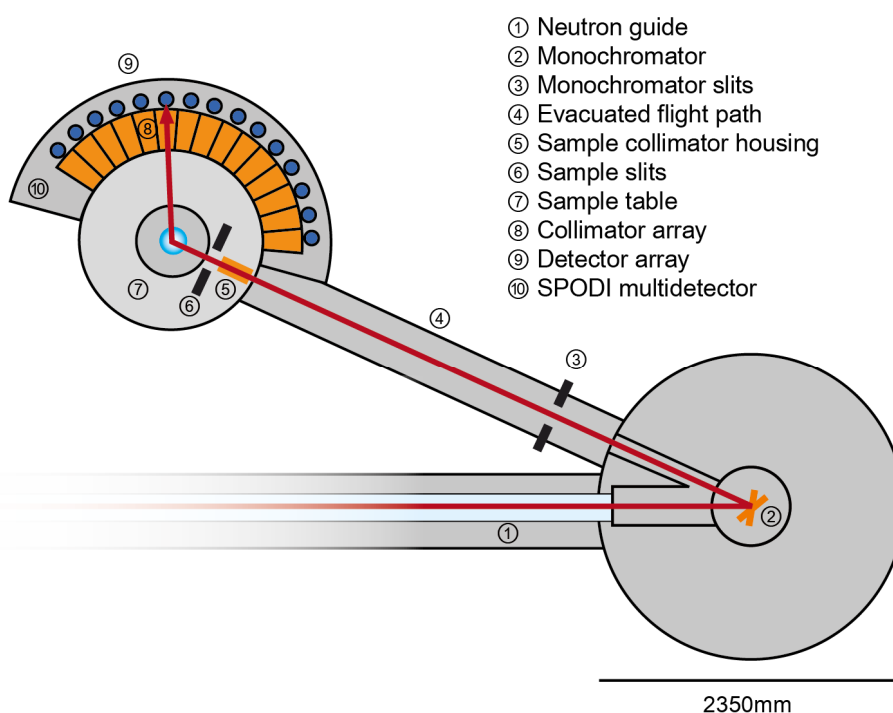


Figure 7: Scheme of the high resolution powder neutron diffractometer SPODI in FRMII, Munich.

X-rays are diffracted at electron density. Differently neutrons are diffracted by the nucleus. X-ray diffraction can give inadequate information especially for light elements in a chemical closeness to a heavy atom, neutrons are scattered also by light elements like boron. However, some elements are not suitable for neutron diffraction due to absorption or poor scattering. These are cadmium, gadolinium and vanadium. In order to analyze, isotopes of those elements needed to be used.

---

Neutron diffraction data was collected at the FRM-II neutron reactor (Garching, SPODI beamline, Ge (551) monochromator, He-3 counter,  $\lambda = 1.54816 \text{ \AA}$ , vanadium container with a diameter of 6 mm) in Munich.

### 3.3. Crystal structure analysis

Crystal structures of materials can be determined by using special calculations. The Rietveld refinement method, which was described and found by Hugo Rietveld in 1966 [28] [29], is a technique that allows a quantitative phase analysis to determine the amounts of the phases in the mixture and the refinement of the crystal structure based on a known structure model. In a diffraction pattern, height, width and position of the reflections give information about the structure of the crystalline material. At the first stage, the theoretical pattern can be simulated if the space group symmetry, unit cell dimensions, atom types, relative coordinates of the atoms, atomic site occupancies and displacement parameters are known for a compound. It is possible to create a theoretical pattern and refine the instrumental and structural parameters until this theoretical line fits to the observed profile by using a least square approach. The goodness of the Rietveld refinement can be estimated visually from the difference curve because the perfect fit results in a straight line for the difference curve.

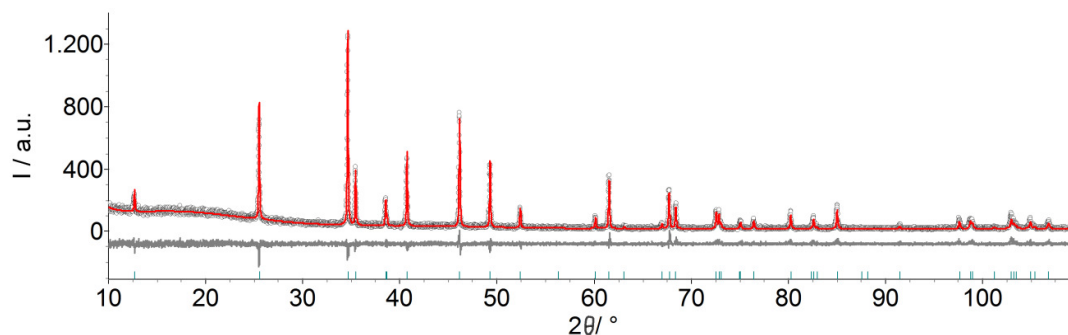


Figure 8: Example of a Rietveld refinement image. Black circles belong to the observed pattern, the red line is the calculated curve and the grey line is the difference curve. The green thickmarks at the bottom are representing the positions of the Bragg reflections.

The quality of the refinement can be checked quantitatively by determining the residuals of the refinement. Goodness values can be summarized as follows:

$$R_p = \frac{\sum_{i=1}^N [I_i^{exp} - I_i^{calc}]^2}{\sum_{i=1}^N I_i^{exp}}$$

$$R_{wp} = \sqrt{\frac{\sum_{i=1}^N [w_i (I_i^{exp} - I_i^{calc})]^2}{\sum_{i=1}^N [w_i I_i^{exp}]^2}}, w_i = \frac{1}{\sqrt{I_i^{exp}}}$$

$$R_{exp} = \sqrt{\frac{(N-P)}{\sum_{i=1}^N [w_i I_i^{exp}]^2}}, w_i = \frac{1}{\sqrt{I_i^{exp}}}$$

$$GOF = \frac{R_{wp}}{R_{exp}}$$

where:

- $I_i^{exp}$  is the observed intensity at point i
- $I_i^{calc}$  is the calculated intensity at point i
- $N$  is the number of points
- $P$  is the number of parameters

For a perfect refinement GOF would be equal to one. If GOF is much higher than one that means a poor refinement and if GOF is much lower than one that indicates an inadequate fit of the model.

### 3.4. Superconductivity measurements

#### 3.4.1. General

Superconductivity is a phenomenon of zero electrical resistance below a critical temperature ( $T_c$ ). In the case of superconductivity, when the sample is cooled down below a characteristic  $T_c$  expulsion of magnetic fields occurs in superconducting materials. Superconductivity can be determined by several methods and one of the most effective and sensitive method to detect superconductivity is SQUID (*Superconducting QUantum Interference Device*) magnetometry. In particular, SQUID is the only method which allows determining the overall magnetic moment of a sample in absolute units.



Figure 9: Quantum Design MPMS SQUID Magnetometer in the institute of Materials Science - TU Darmstadt

The magnetic signal of the sample is obtained via a superconducting pick-up coil with four windings. An alternating magnetic flux is formed in the pick-up coil with the movement of the sample up and down which leads to an alternating output voltage of the SQUID device. By locking the frequency of the readout to the frequency of the movement, the magnetometer system can achieve the extremely high sensitivity for ultra small magnetic signals.

Magnetization measurements were carried out using a SQUID magnetometer (Quantum design MPMS), using a magnetic field of 50 Oe under field cooled and zero field cooled conditions between 1.8 K and 15 K.

A Quantum design MPMS SQUID magnetometer (Institute of Materials Science - TU Darmstadt) was used to recall the data in this work.

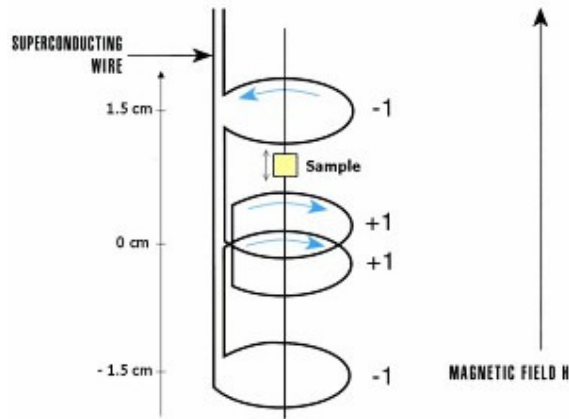


Figure 10: Pick-up coil in SQUID Magnetometer <sup>[30]</sup>.

### 3.4.2. Sample preparation for superconductivity measurements

Solid pieces or powders can be used for the superconductivity measurements in the SQUID magnetometer. At first, the sample has to be weighted as about 20 – 50 mg. Then the sample is placed into a polymeric capsule which is not giving any magnetic signal the sample and compacted as much as possible to densify the sample. The capsule is then fixed in the middle point of a polymeric rod like a straight straw which is then placed into the SQUID magnetometer.

After the sample is introduced into the machine, the chamber is evacuated. A magnetic field of about 10 Oersted (Oe) is applied to the sample and a centering process is done before starting the measurement. The centering process can be done at room temperature or at lower temperatures. After the centering, the magnetic field is set to 0 and the sample is cooled down to 1.8 K without applying a magnetic field. At 1.8 K the magnetic field is set to a desired value (50 Oe in this work) which should not be lower than the value used during the centering process. Then the measurement can be done by using a pre-determined measurement ramp (heating and measurement steps in a desired temperature range starting from 1.8 K to 10 or 15 K). This measurement is called zero field cooled measurement since the system is cooled down to 1.8 K with zero magnetic field. Field cooled measurement can also be done by applying a magnetic field during cooling the sample. In case of a superconducting sample, the transition intensity of field cooled measurement is slightly lower than that of zero field cooled measurement.

---

### **3.5. Morphological analysis via scanning electron microscopy**

The morphology of the samples was examined by means of a scanning electron microscope (SEM, Philips XL 30 FEG) coupled with an energy dispersive X-ray (EDX) analyzer. The microscope is equipped with a LaB<sub>6</sub> electron gun, a secondary electron (SE) detector and a back scattered electron detector (BSD). Therefore, the instrument can be operated in different modes. The SEM investigation was performed using a SE detector under vacuum (pressure is typically at  $\leq 5 \times 10^{-5}$  Torr inside the SEM chamber) with the acceleration voltage of 10-20 kV.



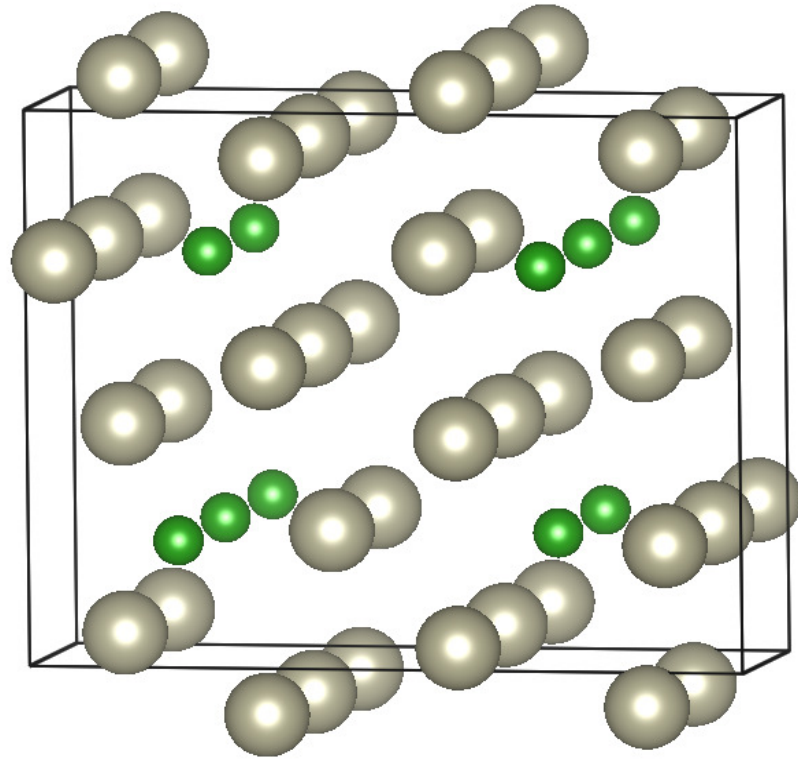


Figure 12: Unit cell of  $\text{Re}_3\text{B}$  (gray = Re, green = B).

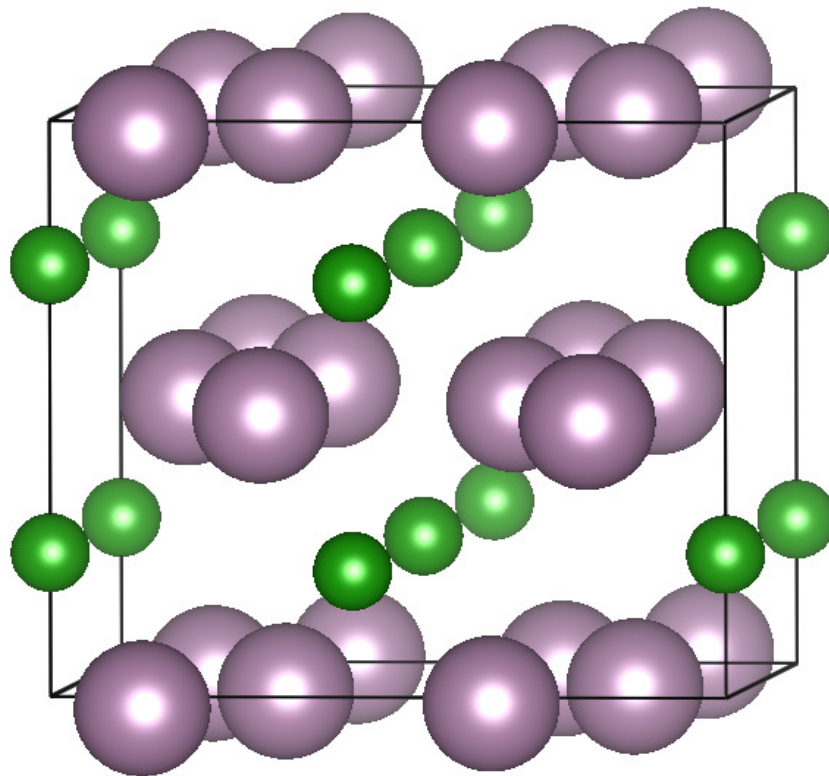


Figure 13: Unit cell of  $\text{Mo}_2\text{B}$  (purple = Mo, green = B).

The second type of possible boron atom arrangement can be described as isolated boron pairs. This kind of isolated boron pairs is observed in  $\text{M}_5\text{B}_3$  and  $\text{M}_3\text{B}_2$  (e.g.,  $\text{Nb}_3\text{B}_2$  and  $\text{Ta}_3\text{B}_2$ ). Generally the distance between the two boron atoms in the pair is between 1.79 Å and 1.80 Å. The crystal structure for  $\text{Nb}_3\text{B}_2$  is given as an example for isolated boron pairs in Figure 14.

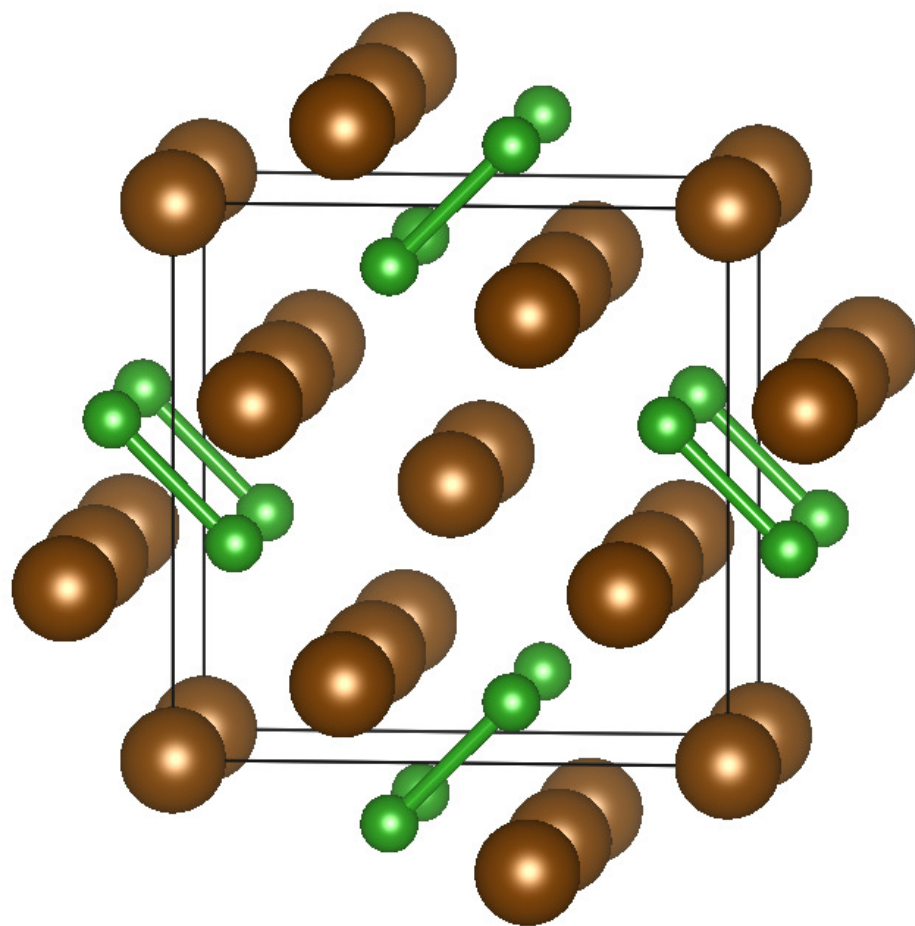


Figure 14: Unit cell of  $\text{Nb}_3\text{B}_2$  (brown = Nb, green = B).

The third type of boron atom ordering in metal borides is described as a zigzag boron chain in metal monoborides (e.g., NbB, TaB, MoB and WB). In the case of the monoborides of niobium, tantalum, molybdenum and tungsten, there are two different types of crystal structures. One of the modifications crystallizes in the orthorhombic and the other one in the tetragonal crystal system. The most significant difference between the orthorhombic and the tetragonal structures is the alignment of the boron atom chains in between the metal atoms. In the orthorhombic structure, boron atoms form a chain aligned in  $c$  direction (Figure 15). In the tetragonal structure there are two different boron atom chains aligning in the  $a$  and  $b$  directions perpendicular to each other (Figure 16). Of those systems included in this work, only molybdenum and tungsten form tetragonal monoborides.

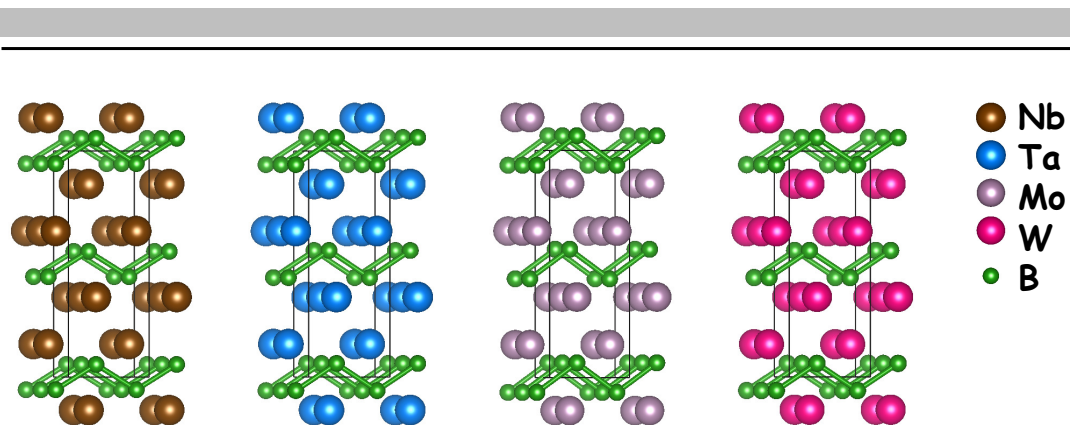


Figure 15: Structures of transition metal monoborides included in this study which crystallize in the orthorhombic crystal system.

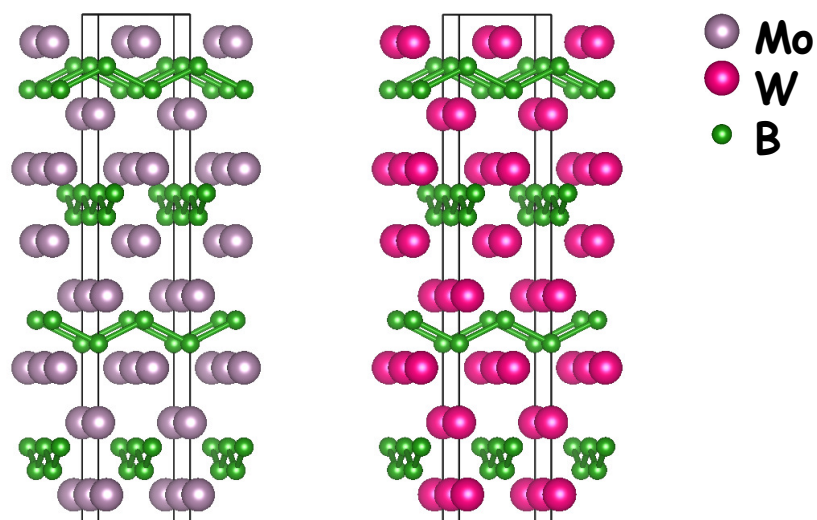


Figure 16: Structures of molybdenum and tungsten monoborides which crystallize in the tetragonal crystal system.

A group of borides with the general formula  $M_3B_4$  (e.g.,  $Nb_3B_4$  and  $Ta_3B_4$ ) exhibits another boron network in their structures which is called double chains. Double chains are composed of two zigzag boron atom chains which are the mirror images connected to each other to form boron atom hexagons in a row as can be seen in Figure 17.

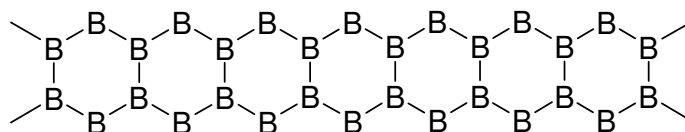


Figure 17: Structure of a "double chain" boron network.

---

Double chain boron atom networks can be seen in the structure of  $Ta_3B_4$  in Figure 18. The boron-boron bond distances between the zigzag chains are shorter than the boron-boron bond distances within the chains.

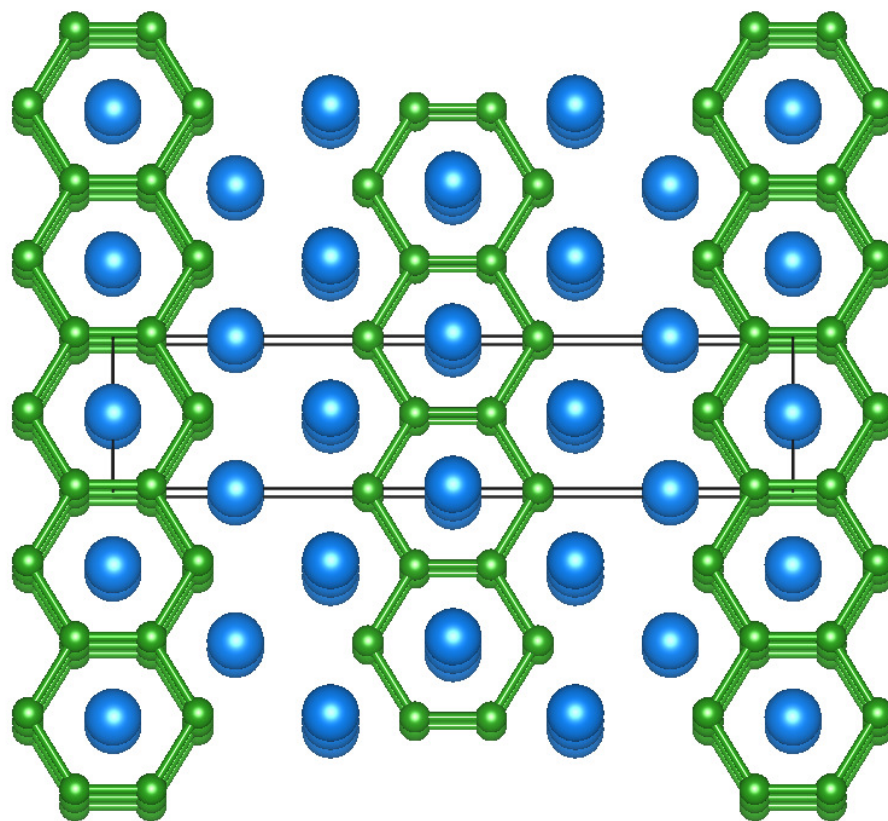


Figure 18: Crystal structure of  $Ta_3B_4$  (blue = Ta, green = B).

Boron atoms in metal boride structures can form two dimensional layers which are hexagonally ordered. Those boron layers can be either planar or they form corrugated layers of condensed cyclohexane-like boron atom rings in chair conformation. Metal atoms are placed on top of the center of the boron atom hexagons. Two dimensional planar boron layers can be seen in diborides  $NbB_2$ ,  $TaB_2$ ,  $MoB_2$  and  $WB_2$  (Figure 19).  $Mo_2B_4$  and  $W_2B_4$  structures contain both of planar and corrugated layers (Figure 20). In the  $ReB_2$  structure all of the planes are in the form of corrugated layers of condensed boron atom six-rings in chair conformation (Figure 21).

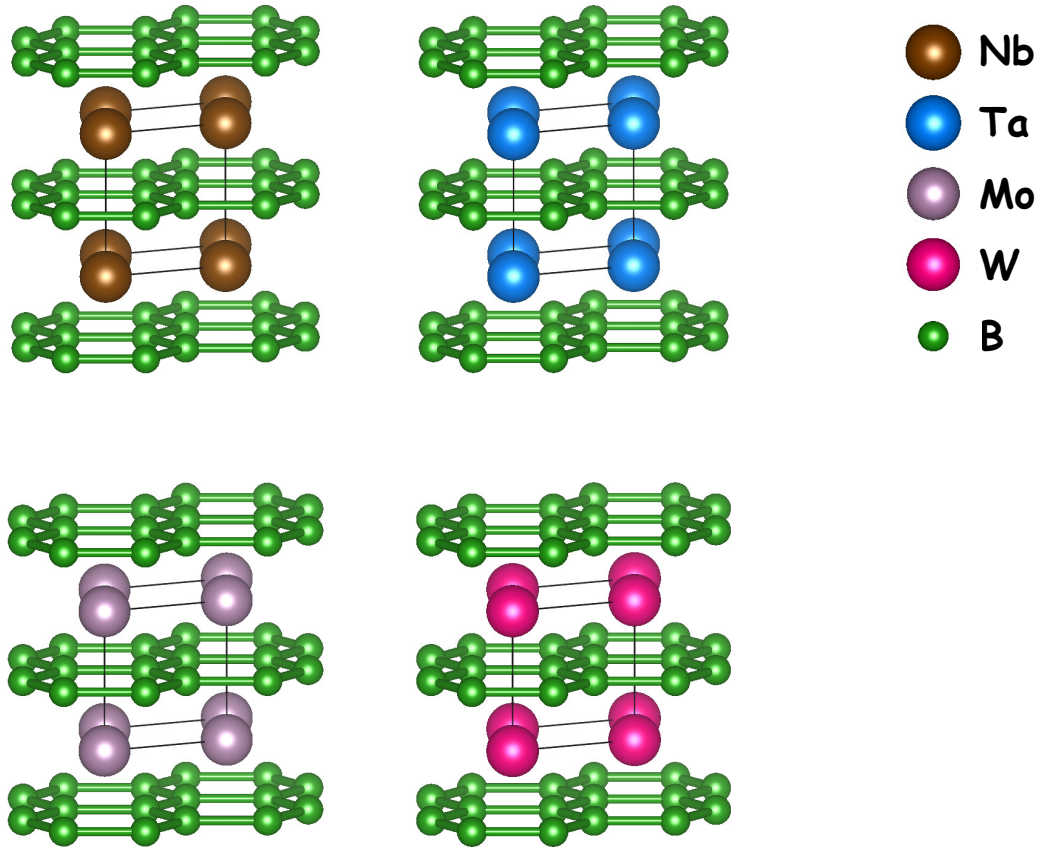


Figure 19: Structures of diborides with planar boron atom layers with  $MB_2$  formula which are included in this study.

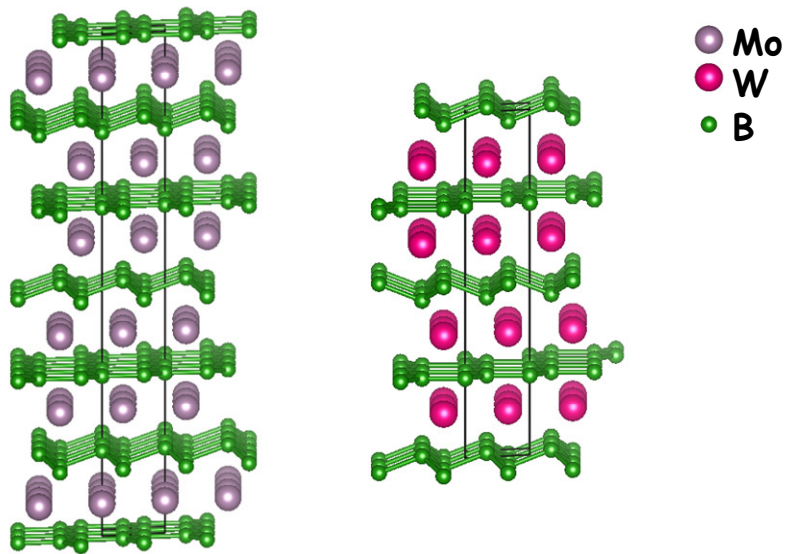


Figure 20: Structures of molybdenum (left) and tungsten (right) diborides containing planar and corrugated boron atom layers with  $M_2B_4$  formula according to the literature <sup>[31]</sup>.

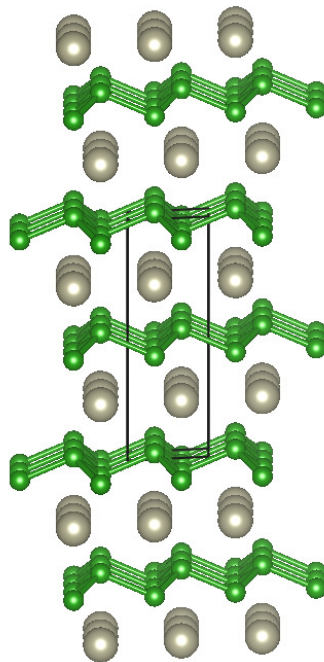


Figure 21: Unit cell of  $\text{ReB}_2$  with corrugated boron atom layers (gray = Re, green = B).

There are some boride structures in transition metal borides which are called hybrid structures.  $\text{Nb}_5\text{B}_6$  and  $\text{Ta}_5\text{B}_6$  which are isomorphous with each other are examples of those types of structures. The structure of those borides is a combination of  $\text{M}_3\text{B}_4$  and MB structures. As can be seen in Figure 22 there are double chains and zigzag chains of boron atoms at the same time.

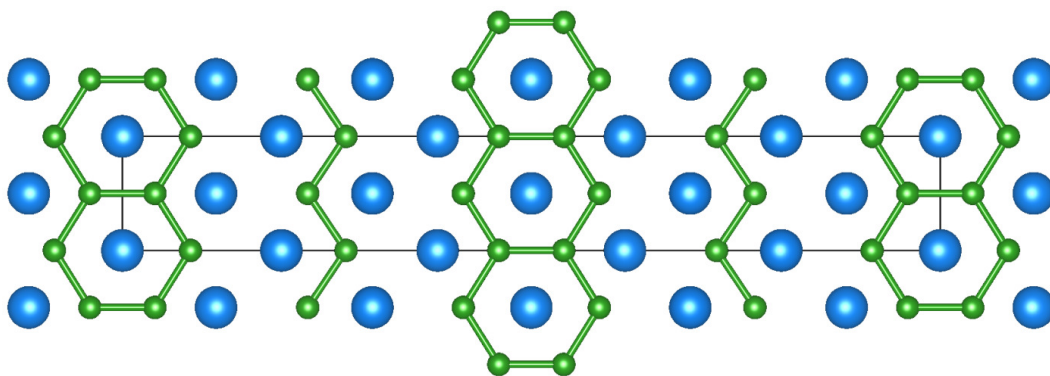


Figure 22: Unit cell of  $\text{Ta}_5\text{B}_6$  (blue = Ta, green = B).

### 4.3. Niobium-boron system

#### 4.3.1. Phase diagram of the Nb-B system

The phase diagram of niobium and boron shows seven different phases including elemental niobium and boron (Figure 23).

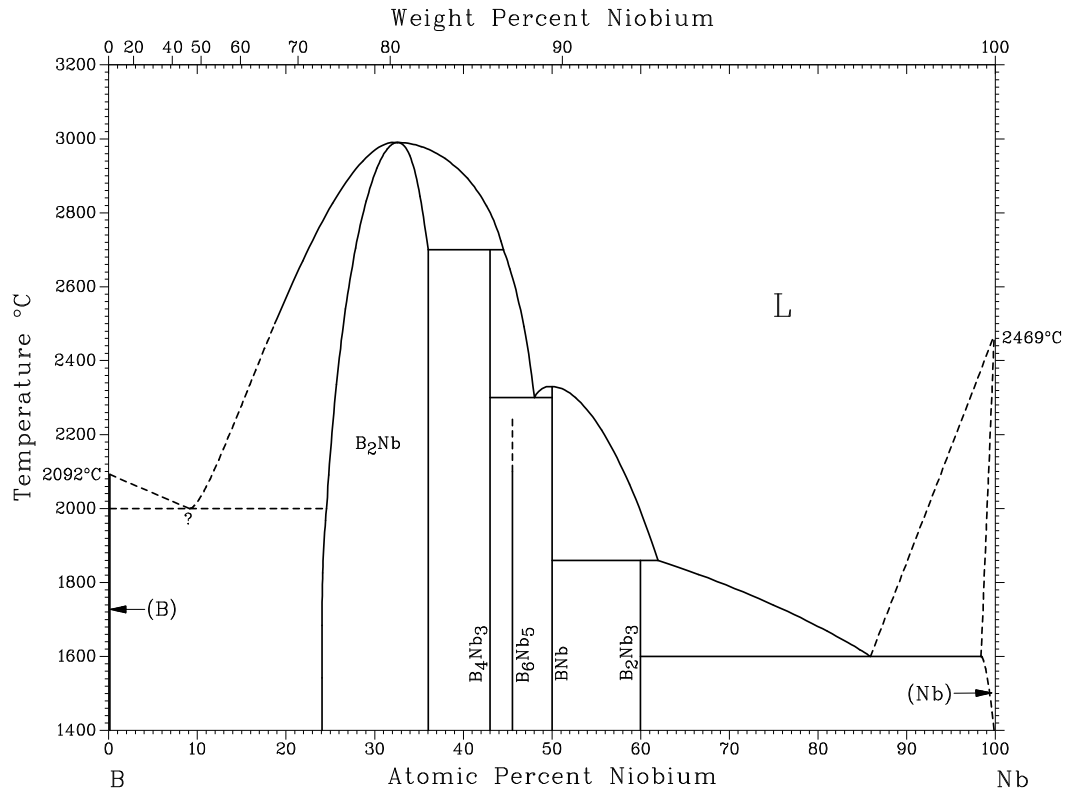


Figure 23: Binary phase diagram of the niobium - boron system <sup>[32]</sup>.

Known binary niobium borides are listed in Table 1 with their compositional range and structure type. To obtain a monophasic sample within a certain stability range (temperature, composition) it is crucial to choose the right synthesis method. Like almost all transition metal borides, niobium borides need to be synthesized at very high temperatures. In some cases, for example when synthesizing Nb<sub>3</sub>B<sub>2</sub>, exceeding the temperature by heating higher than 2050 °C causes decomposition of the desired phase.

Table 1: Binary phases known in the niobium - boron system.

Phase	Composition at. % Nb	Space Group	Structure type
$\text{Nb}_3\text{B}_2$	60	$P4/mbm$	$\text{Si}_2\text{U}_3$
$\text{NbB}$	50	$Cmcm$	$\text{CrB}$
$\text{Nb}_5\text{B}_6$	45.5	$Cmmm$	$\text{Ta}_5\text{B}_6$
$\text{Nb}_3\text{B}_4$	42.9	$Immm$	$\text{Ta}_3\text{B}_4$
$\text{NbB}_2$	24 to 36	$P6/mmm$	$\text{AlB}_2$

#### 4.3.2. Literature review

$\text{Nb}_3\text{B}_2$  was synthesized in 1958 and its crystal structure was determined with tetragonal symmetry (space group  $P4/mbm$ ) by Nowotny *et al.* [33]. The structure determination was done using an X-ray diffraction powder pattern.  $\text{Nb}_3\text{B}_2$  phase was reported as not superconducting down to the temperatures as low as 1 K [34].

The first report on the synthesis and structure of  $\text{NbB}$  was published by Andersson *et al.* in 1950 [35]. The crystal structure was described in the orthorhombic crystal system with space group  $Cmcm$  by using X-ray diffraction single crystal data.  $\text{NbB}$  was reported to be superconducting below 8.5 K [36].

$\text{Nb}_5\text{B}_6$  was not discovered till 1990, when Bolmgren and Lundström surprisingly found it as a new binary phase in the niobium boron system [37]. The unit cell parameters were refined by using X-ray powder diffraction data, but no complete crystal structure determination was performed.  $\text{Nb}_5\text{B}_6$  was described to be isomorphous with  $\text{V}_5\text{B}_6$  and  $\text{Ta}_5\text{B}_6$ . There are no literature reports on the superconductivity of  $\text{Nb}_5\text{B}_6$ .

The existence of the phase  $\text{Nb}_3\text{B}_4$  was reported in a publication of Andersson and Kiessling in 1950 together with  $\text{NbB}$  [35]. The crystal structure was determined in the orthorhombic crystal system (space group  $Immm$ ) based on X-ray diffraction powder data.  $\text{Nb}_3\text{B}_4$  was reported to be superconducting below 1.28 K. [34, 36]

The most interesting phase in the niobium and boron binary system is  $\text{NbB}_2$ , because of the different reports on its superconductivity.  $\text{NbB}_2$  was firstly synthesized in 1949 by Norton *et al.* [38]. The crystal structure was described in the hexagonal crystal system (space group  $P6/mmm$ ). Cooper *et al.* and Leyarovska *et al.* reported a  $T_C$  of 3.87 K [39]

---

and 0.62 K <sup>[40]</sup>, respectively. In an investigation on the pressure dependence of the superconducting transition temperature Schirber *et al.* reported a  $T_C$  at 9.4 K <sup>[41]</sup> for a single crystal sample of  $NbB_2$  which is much higher than the values reported earlier. In 2006, Takagiwa *et al.* found an explanation on those different values of  $T_C$  by showing a correlation between superconductivity and composition of  $NbB_{2+x}$  <sup>[42]</sup>. In their study  $T_C$  varied between 2.2 K and 5.8 K with boron to niobium ratios that varied between 1.95 and 2.4.

Nunes *et al.* showed that the homogeneity range of  $NbB_2$ -type phases ranges from  $NbB_{1.86}$  up to  $NbB_{2.34}$  <sup>[43]</sup>.

### 4.3.3. Synthesis and structural characterization of $Nb_3B_2$

$Nb_3B_2$  is one of the most challenging binary phases in the niobium-boron system to synthesize because of its small thermal stability range. Low temperature synthesis by using the quartz ampoule technique up to 1050 °C did not result in the synthesis of  $Nb_3B_2$ . The same problem was observed in the high frequency induction furnace up to 1800 °C. On the other hand, using the arc melting technique meant to exceed the upper limit of the thermal stability of  $Nb_3B_2$  which is around 1900 °C. In order to obtain the phase, it was necessary to use special quenching methods after arc melting.

The desired phase was prepared by combining different synthesis steps. At first, elemental powders were mixed together by using a ball mill for one minute at fifteen rpm and then the mixture was pressed into pellets of five mm diameter. The pellet was put into the electrical arc melting chamber. The melting process was repeated for three times with flipping the sample in between in order to obtain a homogeneous product. The product from the arc melting process contained only  $NbB$  and  $Nb$  (Figure 24(a)). The product was then ground and mixed in a ball mill for three minutes. The mixture was put into a boron nitride crucible which was then placed into the high frequency induction furnace. After heating the sample for one hour at 1800 °C, the final product was taken out from the furnace after fast cooling. The phase analysis (Figure 24(b)) showed that the formation of  $Nb_3B_2$  was successfully achieved with  $NbB$  and  $Nb$  as byproducts. An increase in reaction time had no effect on the number of phases present in the final product.  $Nb_3B_2$  is apparently in equilibrium with  $Nb$  and  $NbB$  which are the neighbor phases of  $Nb_3B_2$ .

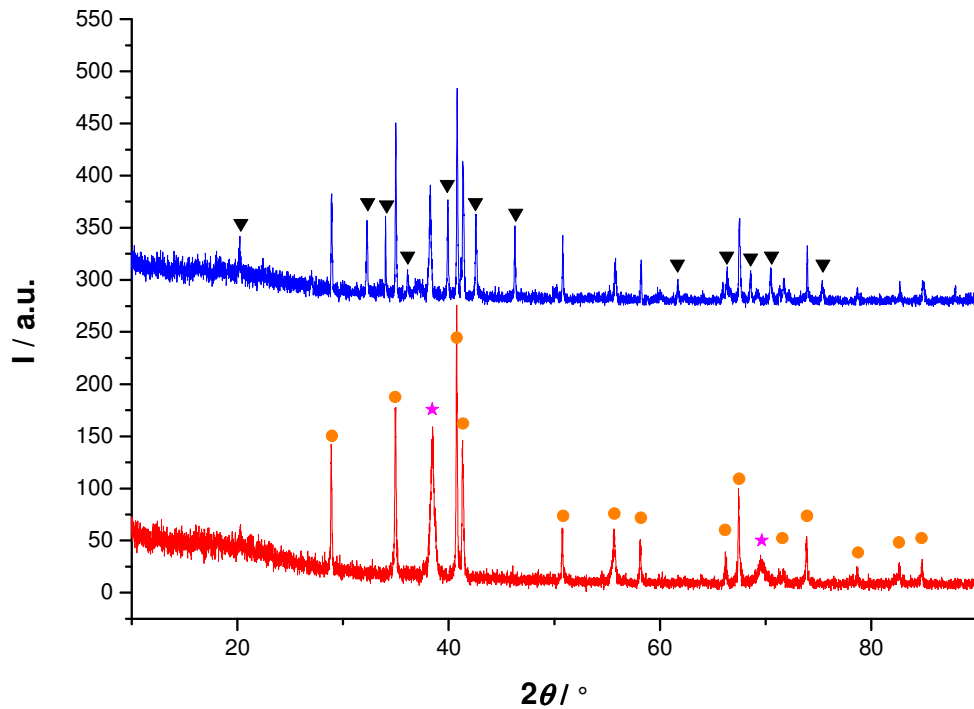


Figure 24: XRD patterns for the intermediate (bottom) and the final product (top) in the synthesis of  $\text{Nb}_3\text{B}_2$ . (a) The intermediate (bottom) contains only NbB (orange circle) and metallic Nb (star). The final product (top) contains also  $\text{Nb}_3\text{B}_2$  (black triangles).

Phase analysis by X-ray powder diffraction showed that the amount of  $\text{Nb}_3\text{B}_2$  is about 30 – 35 % of the total sample. The amount of Nb and NbB was determined to be approximately 21 % and 46 %, respectively. The pattern shows unidentified reflections with low intensities at  $36.1$  and  $37.2^\circ 2\theta$  which decreases the quality of the refinement (Figure 25). The structure model from literature <sup>[44]</sup> was confirmed but not refined. The unit cell parameters were refined with the Rietveld method.  $\text{Nb}_3\text{B}_2$  as synthesized in this work has slightly larger unit cell parameters compared to the literature values (Table 2).

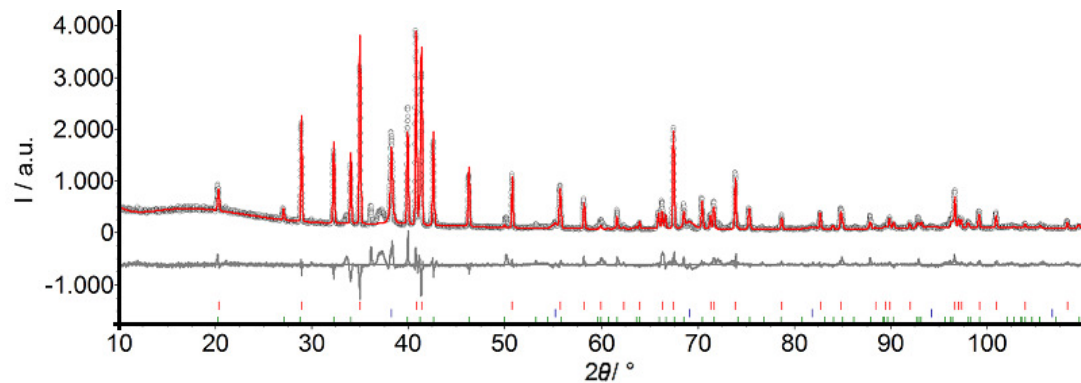


Figure 25: X-ray diffraction pattern of  $\text{Nb}_3\text{B}_2$  fitted using the Rietveld method. The black circles are the observed data, the red line is the calculated curve, and the gray curve is the difference curve between the observed and the calculated curves. The tickmarks with different colors at the bottom are representing the positions of the reflections for each phase. (green =  $\text{Nb}_3\text{B}_2$ , blue = Nb, red = NbB)

Table 2: Unit cell parameters and residuals of the refinement of  $\text{Nb}_3\text{B}_2$ . Literature <sup>[44]</sup> values are given in brackets.

Phase	$\text{Nb}_3\text{B}_2$
Diffractometer	STOE Stadi-P-Diffractometer
Wavelength / Å	1.54056
Temperature / K	293
Max. $2\theta / ^\circ$	110
$R_{\text{exp}}$	6.51
$R_{\text{wp}}$	16.41
$R_{\text{p}}$	11.27
GOF	2.52
Crystal system	tetragonal
Space group	$P4/mbm$ (no. 127)
$a / \text{Å}$	6.1980(2) – [6.192(2)]
$c / \text{Å}$	3.2917(1) – [3.289(2)]
$V / \text{Å}^3$	126.45(1) – [126.1]
Calc. density / $\text{g cm}^{-3}$	7.8880(5)
Sample code	CR022

In the morphological analysis of the  $\text{Nb}_3\text{B}_2$  sample it was seen that the particle size distribution is in a wide range between a few nanometers and a few micrometers. The particles do not have well defined shapes since the sample was ground in a boron carbide mortar in between two heating processes of arc melting and high frequency induction furnace. It was also possible to see that the particles are sticking together after the heat

treatment in the induction furnace. EDX analysis showed that there are no other elements than niobium and boron in the sample (Figure 26).

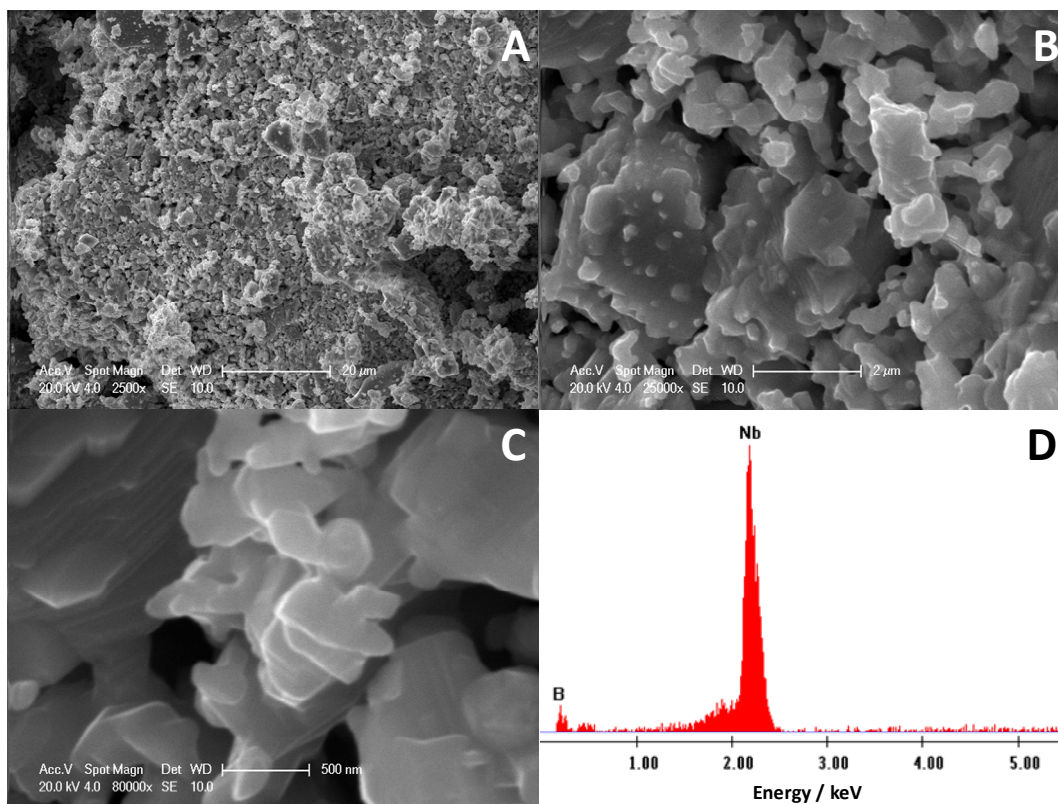


Figure 26: SEM images of  $\text{Nb}_3\text{B}_2$  in magnification (A) 2500, (B) 25000, (C) 80000 and (D) EDX analysis.

#### 4.3.4. Synthesis, structural characterization and superconductivity measurements of $\text{NbB}$

The synthesis of niobium monoboride was possible both in quartz ampoules and in the electric arc furnace. In order to get monophasic niobium monoboride, an excess of boron of 15 % was used. Unless the excess boron was added to the starting materials, elemental niobium or phases with lower boron content form in the final product.

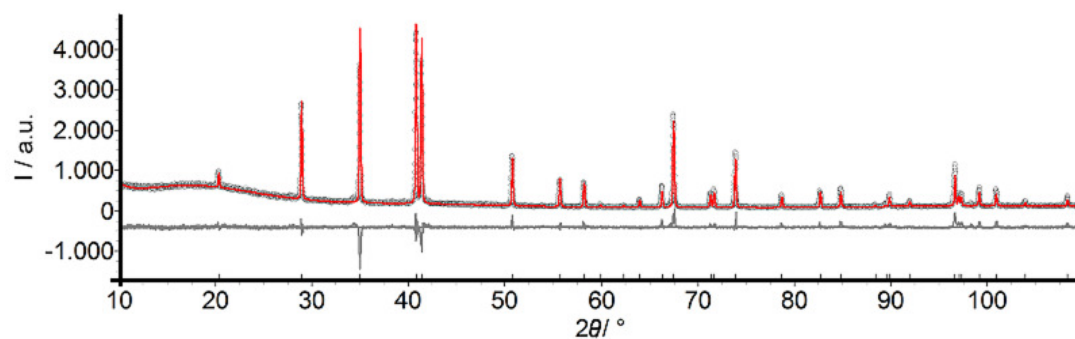


Figure 27: X-ray diffraction pattern of NbB fitted using the Rietveld method. The black circles are the observed data, the red line is the calculated curve, and the gray curve is the difference curve between the observed and the calculated curves. The tickmarks at the bottom are representing the positions of the reflections for NbB phase.

As can be seen in Figure 27, niobium monoboride was obtained as a well crystalline powder and no impurities or side phases were observable. The refinement of the unit cell parameters from the XRD data was done by using the Rietveld method based on the structure model from literature <sup>[35]</sup>. The information from literature was confirmed. Unit cell parameters and residuals of the refinement are given in Table 3.

Table 3: Unit cell parameters and residuals of the refinement of NbB. Literature <sup>[45]</sup> values are given in brackets.

Phase	NbB
Diffractometer	STOE Stadi-P-Diffractometer
Wavelength / Å	1.54056
Temperature / K	293
Max. $2\theta$ / °	110
$R_{\text{exp}}$	6.27
$R_{\text{wp}}$	10.33
$R_{\text{p}}$	7.34
GOF	1.65
Crystal system	Orthorhombic
Space group	<i>Cmcm</i> (63)
$a$ / Å	3.2967(1) – [3.2961(6)]
$b$ / Å	8.7228(2) – [8.7224(8)]
$c$ / Å	3.1664(1) – [3.1653(4)]
$V$ / Å <sup>3</sup>	91.055(3) – [91.00]
Calc. density / g cm <sup>-1</sup>	7.5660(2)
Sample code	CR018

SEM analysis of the NbB sample showed that the particle size distribution is in a wide range between a few nanometers and a few micrometers. The particles look compact and have sharp edges possibly caused by the grinding process in the boron carbide mortar. There was no agglomeration of the small particles in the sample. EDX analysis showed no other elements than niobium and boron in the sample (Figure 28).

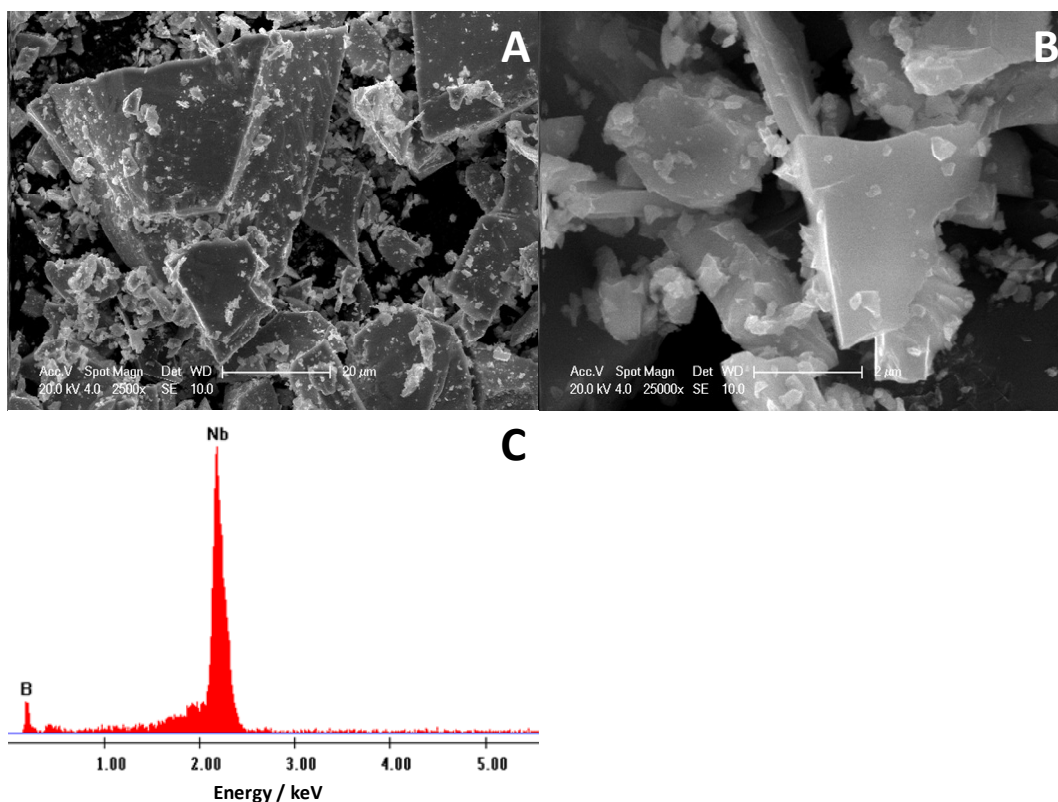


Figure 28: SEM images of NbB in magnification (A) 2500, (B) 25000 and (C) EDX analysis.

Superconductivity measurements of NbB were performed in a SQUID magnetometer. A zero-field cooled measurement was done between 1.8 K and 15 K. Superconductivity measurements showed a clear transition with an onset temperature of 9.3 K (Figure 29), which is fitting with the  $T_C$  value of metallic niobium. Although in the XRD pattern no elemental niobium had been observed, the value of the  $T_C$  at 9.3 K indicates the presence of traces of Nb in the sample. Since it is possible to detect superconductivity even with very small amounts of a superconducting phase it is not possible to conclude from these measurements that NbB becomes superconducting, although NbB was reported to become superconducting below 8.25 K <sup>[36]</sup>.

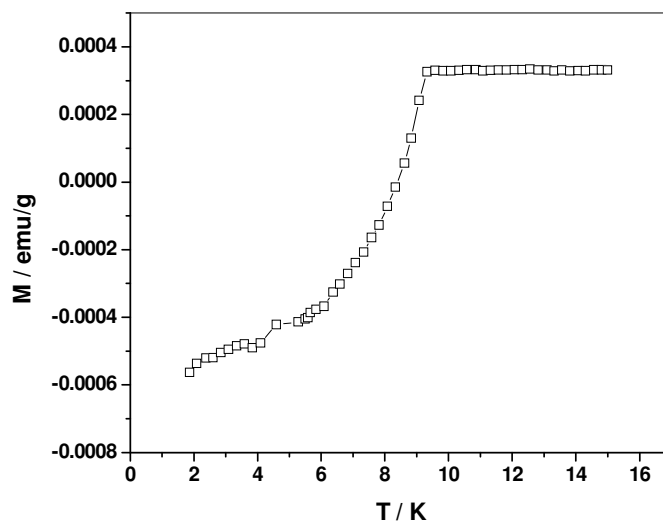


Figure 29: Superconductivity measurement (ZFC) for NbB.

#### 4.3.5. Synthesis and structural characterization of Nb<sub>5</sub>B<sub>6</sub>

Nb<sub>5</sub>B<sub>6</sub> is one of the most interesting phases in the niobium boron system. In the phase diagram it is marked with a question mark (Figure 23). The upper level of the temperature range which characterizes the stability range of Nb<sub>5</sub>B<sub>6</sub> is not certain.

Nb<sub>5</sub>B<sub>6</sub> was synthesized by arc melting as described in section 2.2.2. It was not possible to get Nb<sub>5</sub>B<sub>6</sub> in monophasic form. When Nb and B were reacting with a metal to boron ratio of 1:1.2 to 1:2.0 the formation of Nb<sub>5</sub>B<sub>6</sub> was observed.

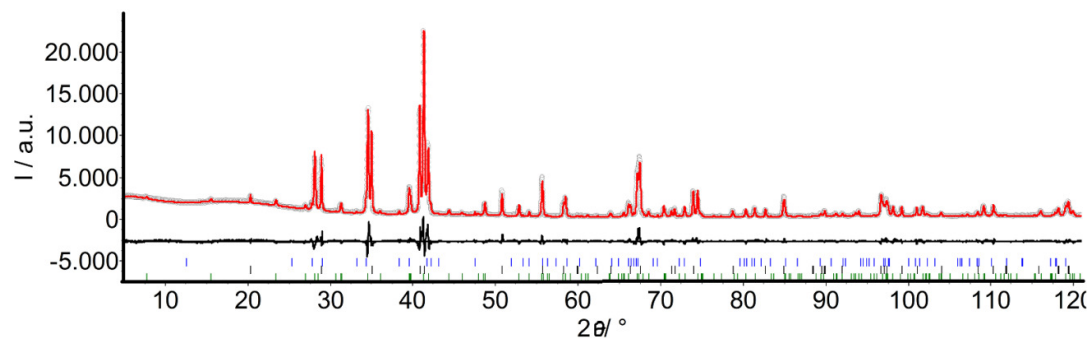


Figure 30: X-ray diffraction pattern of  $\text{Nb}_5\text{B}_6$  fitted using the Rietveld method. The black circles are the observed data, the red line is the calculated curve, and the gray curve is the difference curve between the observed and the calculated curves. The tickmarks at the bottom are representing the positions of the reflections for each phase (blue =  $\text{Nb}_3\text{B}_4$ , black =  $\text{NbB}$  and green =  $\text{Nb}_5\text{B}_6$ ).

XRD data was refined based on the literature model for  $\text{Ta}_5\text{B}_6$  <sup>[46]</sup> using the Rietveld method. The sample contained 36 %  $\text{NbB}$  and 3%  $\text{Nb}_3\text{B}_4$  in addition to  $\text{Nb}_5\text{B}_6$ . Residuals of the Rietveld refinement and crystallographic information on the unit cell are listed in Table 4.

Table 4: Unit cell parameters and the residuals of the refinement for the X-ray diffraction data of  $\text{Nb}_5\text{B}_6$ . Literature <sup>[37]</sup> values are given in brackets.

Phase	$\text{Nb}_5\text{B}_6$
Diffractometer	STOE Stadi-P-Diffractometer
Wavelength / Å	1.54056
Temperature / K	293 (2)
Max. $2\theta / ^\circ$	120
$R_{\text{exp}}$	3.00
$R_{\text{wp}}$	9.45
$R_{\text{p}}$	6.68
GOF	3.15
Crystal system	Orthorhombic
Space group	$Cmmm$ (65)
$a / \text{Å}$	22.771(1) – [22.768(2)]
$b / \text{Å}$	3.1538(1) – [3.1539(3)]
$c / \text{Å}$	3.3014(1) – [3.2992(3)]
$V / \text{Å}^3$	237.09(1) – [236.8]
Calc. density / $\text{g cm}^{-3}$	7.4158(2)
Sample code	CR031

Cell parameters were found to be very close to the literature values of Nb<sub>5</sub>B<sub>6</sub> but slightly larger than Ta<sub>5</sub>B<sub>6</sub> [46] phase which is isotypic with Nb<sub>5</sub>B<sub>6</sub>. Refinement of the occupancies of the niobium atomic positions gave values close to one and they were fixed to one. Unit cell parameters, the atomic positions and the displacement parameters of the atoms were refined. Displacement parameters for three boron atoms were coupled together. Refined atomic positions, displacement parameters and occupancy values are given in Table 5.

Table 5 Refined structural parameters of the X-ray powder diffraction data of Nb<sub>5</sub>B<sub>6</sub>

Atom	Wyck. Site	$x/a$	$y/b$	$z/c$	Occupancy	$B_{eq}$
<b>Nb1</b>	$2a$	0	0	0	1	0.35(6)
<b>Nb2</b>	$4g$	0.3851(1)	0	0	1	0.30(4)
<b>Nb3</b>	$4h$	0.1935(1)	0	1/2	1	0.18(5)
<b>B1</b>	$4h$	0.089(2)	0	1/2	1	0.4(2)
<b>B2</b>	$4g$	0.281(2)	0	0	1	0.4(2)
<b>B3</b>	$4h$	0.461(1)	0	1/2	1	0.4(2)

SEM analysis of the sample of Nb<sub>5</sub>B<sub>6</sub> showed big particles with a size of around 20 micrometers. The particles look compact and have sharp edges probably caused by the grinding process in the boron carbide mortar. There was no agglomeration of the small particles in the sample. EDX analysis showed no other elements than niobium and boron (Figure 31).

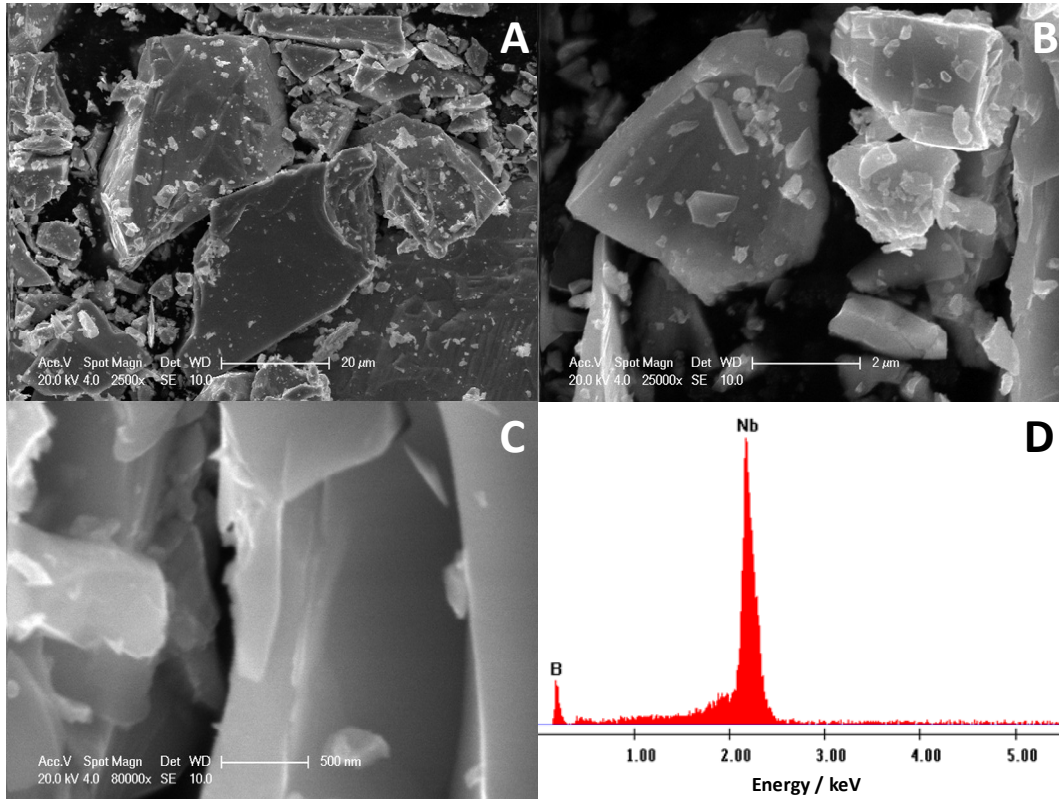


Figure 31: SEM images of  $\text{Nb}_5\text{B}_6$  in magnification (A) 2500, (B) 25000, (C) 80000 and (D) EDX analysis.

Since the sample was not monophasic, a superconductivity measurement was not done for  $\text{Nb}_5\text{B}_6$ .

#### 4.3.6. Synthesis, structural characterization and superconductivity measurements of $\text{NbB}_{2\pm x}$

Niobium diboride is the phase with the highest compositional range in the niobium-boron phase diagram. The preparation of niobium diboride is not a problem in terms of varying reactant composition. Using different ratios of niobium and boron in the starting mixture results in varying values of the occupancies of the atoms in the structure. In literature [42-43] different niobium diborides which have niobium-to-boron ratios (1:1.934 and 0.848:2) were reported. They crystallize with the same crystal structure but exhibit slightly different lattice parameters. It was also described that in the presence of a niobium or boron deficiency in the system, niobium diborides show different transition temperatures (Table 6).

Table 6: The nominal compositions,  $T_c$  values and the refined lattice parameters of  $\text{NbB}_{2\pm x}$  from literature <sup>[42]</sup>

Nominal composition	$\text{NbB}_{1.95}$	$\text{NbB}_2$	$\text{NbB}_{2.05}$	$\text{NbB}_{2.1}$	$\text{NbB}_{2.4}$
$a / \text{\AA}$	3.10762(1)	3.10485(1)	3.10211(1)	3.09922(1)	3.09672(1)
$c / \text{\AA}$	3.28444(2)	3.29903(2)	3.3075(2)	3.31183(2)	3.31584(2)
$T_c / \text{K}$	2.2	4.6	5.5	5.7	5.8

The synthesis of  $\text{NbB}_2$  was possible in quartz ampoules, but also in the high frequency induction furnace and via arc melting. Samples of  $\text{NbB}_{2\pm x}$  were synthesized in the electric arc with varying boron to metal ratios (2.0:1 to 2.2:1) were synthesized. According to the XRD data they appeared to be monophasic.

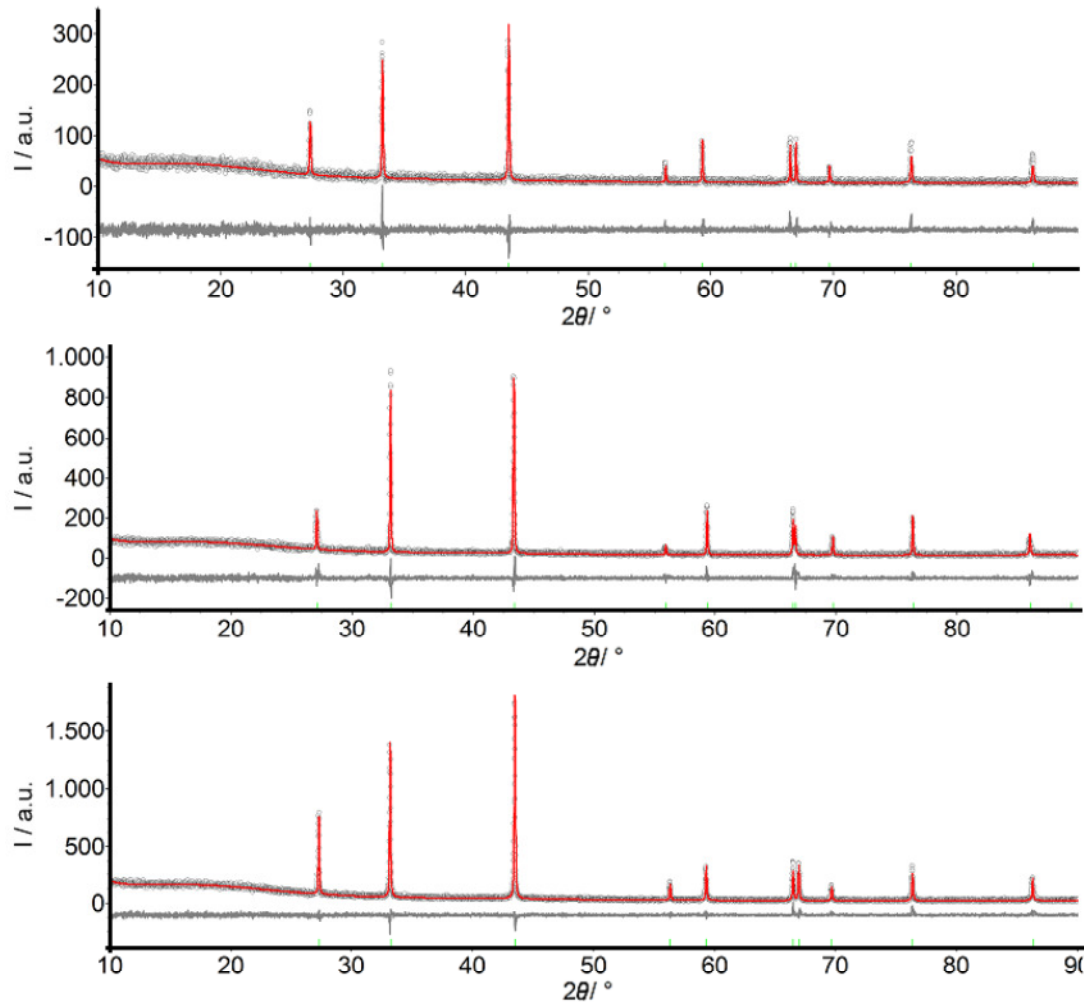


Figure 32: Rietveld analysis for  $\text{NbB}_{2\pm x}$  samples produced with varying amount of boron, B:Nb = 2.0 (top), = 2.2 (middle), = 2.1 (bottom). The black circles are the observed data, the red line is the calculated curve, and the gray curve is the difference curve between the observed and the calculated curves. The tickmarks at the bottom are representing the positions of the reflections for  $\text{NbB}_2$ .

XRD powder patterns were recorded for three different NbB<sub>2±x</sub> samples (Figure 32). It was not possible to refine the positional parameters and the occupancies of the boron sites. The refinements of the unit cell parameters were done by using the Rietveld method based on the structure model for stoichiometric NbB<sub>2</sub> from literature <sup>[42]</sup> (Figure 32). The information about the structure model of NbB<sub>2</sub> from literature was confirmed. Unit cell parameters for three different NbB<sub>2</sub> samples are given in Table 7.

Table 7: The refined unit cell parameters for three different NbB<sub>2±x</sub> samples with varying boron to niobium ratios.

Phase	NbB <sub>2±x</sub>		
Diffractometer	STOE Stadi-P-Diffractometer		
Wavelength / Å	1.54056		
Temperature / K	293		
Max. 2θ / °	90		
Crystal system	Hexagonal		
Space group	<i>P6/mmm</i> (191)		
Starting composition, Nb:B	1:2.0	1:2.2	1:2.1
<i>a</i> / Å	3.1139(1)	3.1110(1)	3.1122(1)
<i>c</i> / Å	3.2651(2)	3.2837(1)	3.2621(1)
<i>V</i> / Å <sup>3</sup>	27.419(3)	27.523(2)	27.362 (1)
Calc. density / g cm <sup>-1</sup>	6.81(6)	6.6(2)	6.70(1)
Sample code	CR037	MK123	MK094

SEM analysis of the NbB<sub>2</sub> sample showed big particles with a size of around 20 micrometers. The particles look compact and have sharp edges. There was no agglomeration of the particles in the sample. A carbon signal was detected in the EDX analysis in addition to niobium and boron, which can be explained because carbon tape was used to fix the powder sample (Figure 33).

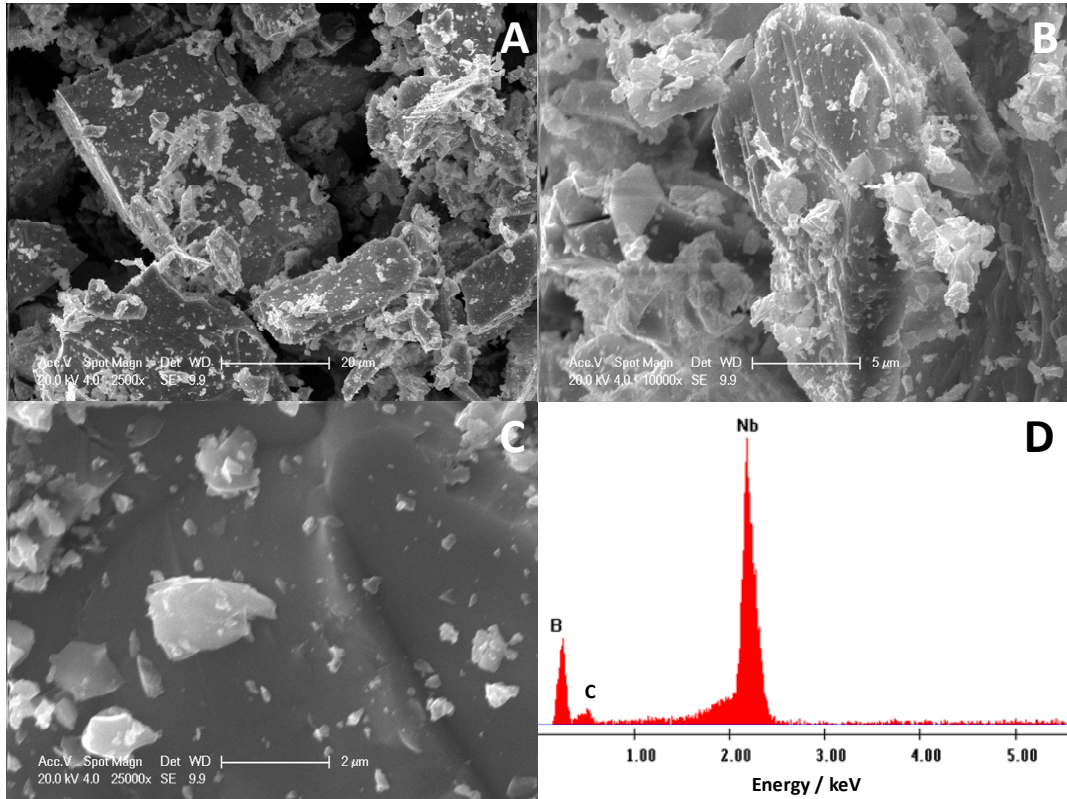


Figure 33: SEM images of NbB<sub>2</sub> in magnification (A) 2500, (B) 10000, (C) 25000 and (D) EDX analysis.

As mentioned above, previous reports were showing different values of transition temperature for superconductivity, and even non-superconductivity for NbB<sub>2</sub> [39-42] was observed. Takagiwa *et al.* found a relationship between T<sub>C</sub> and the unit cell parameters. They reported increasing T<sub>C</sub> values from 2.2 K to 5.8 K for increasing boron to niobium ratios from 1.95 up to 2.4. (Table 6).

In order to clarify the observation of non-superconductivity described in literature for some of the NbB<sub>2</sub> samples, superconductivity measurements were done with zero-field cooling between 1.8 K and 10 K for three samples of NbB<sub>2±x</sub> that were synthesized with varying boron to niobium ratios and that exhibited different unit cell parameters.

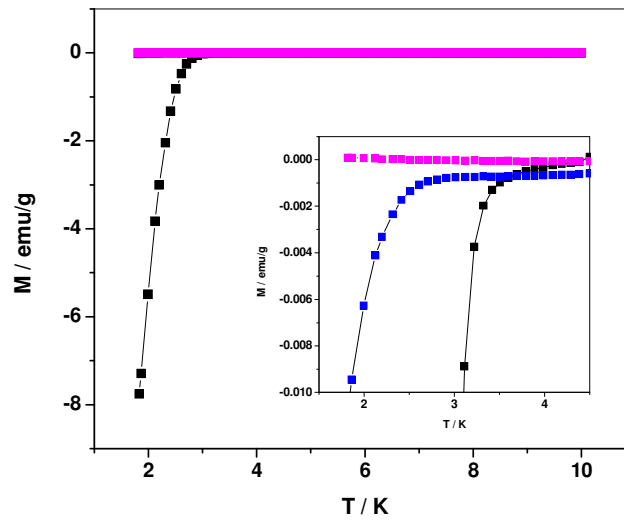


Figure 34: Superconductivity measurements (ZFC) for three different  $\text{NbB}_2$  samples. The inset shows the magnetization versus temperature graph in a smaller scale which is zoomed into the area where the superconducting transitions of two of the  $\text{NbB}_2$  samples are. (M:B = 1:2.0 pink, M:B = 1:2.1 blue, M:B = 1:2.2 Black)

The results of the measurements showed different transition temperatures. The sample with a boron to metal ratio of 2.2 showed a superconducting transition at 3.5 K, the one with 2.1 was showing a superconducting  $T_C$  at 2.8 K and the third sample with boron to metal ratio of 2.0 was not showing any transition in the magnetization versus temperature plot, down to temperatures as low as 1.8 K (Figure 34).

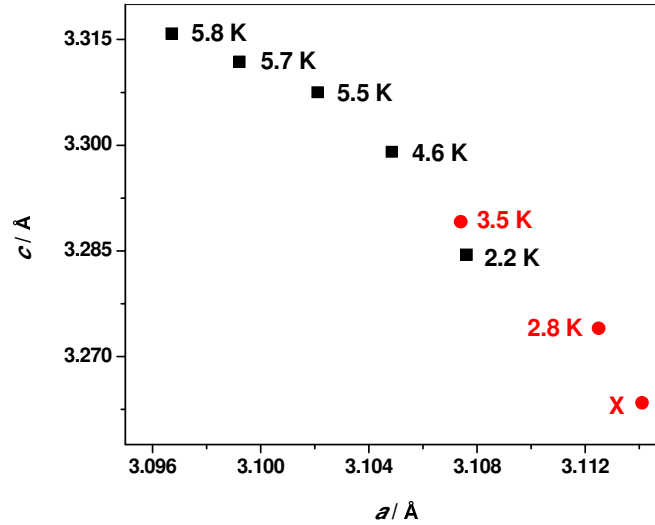


Figure 35: Unit cell parameters for different samples of  $\text{NbB}_{2\pm x}$ .  $c$  values are decreasing with increasing  $a$ . The black squares are from the report of Takagiwa *et al.* [42] and the red circles are the three different  $\text{NbB}_{2\pm x}$  samples produced in this work. The standard deviations for  $a$  and  $c$  are smaller than the symbol sizes. Numbers in the plot give  $T_C$  values observed in [42] and measured in this work.

Comparing these results to the results of Takagiwa *et al.*, it can be seen that the unit cell parameters  $a$  and  $c$  are following a trend.  $T_C$  values decrease with increasing  $a$  and decreasing  $c$  (Figure 35). Our results are in good agreement with those described in literature. Takagiwa *et al.* reported 2.2 K as the lowest  $T_C$ . Here an  $\text{NbB}_{2+x}$  sample with low  $c$  and high  $a$  was non-superconducting down to 1.8 K (X in Figure 35).

#### 4.3.7. Concluding remarks on the Nb-B system

It was possible to synthesize  $\text{Nb}_3\text{B}_2$  and  $\text{Nb}_5\text{B}_6$ , but these phases were obtained only in the presence of side phases.  $\text{NbB}$  and several samples of  $\text{NbB}_{2\pm x}$  were synthesized as monophasic phases without any traceable impurities. Although in the phase diagram

---

$\text{Nb}_3\text{B}_4$  was mentioned to be present, it could not be proved to exist. Three different synthetic attempts did not result in the formation of  $\text{Nb}_3\text{B}_4$ , not even in a mixture.

The samples obtained in arc melting for each phase showed big and compact particles which have sharp edges in SEM. EDX analysis disproved the existence of any impurities in the samples.

In terms of superconductivity the most interesting phase is  $\text{NbB}_{2\pm x}$  with its different  $T_C$  values for different Nb:B ratios. In this study it was seen that  $T_C$  correlates with the unit cell parameters. The changing boron amount influences the structure and the properties.

One of the interesting observations during the synthesis of the binary niobium borides was that reactions in quartz ampoules can lead to the formation of niobium silicides if the metal to boron ratio in the starting composition is higher than one.

## 4.4. Tantalum-boron system

### 4.4.1. Phase diagram of the Ta-B system

The phase diagram of tantalum and boron shows seven different phases including elemental tantalum and boron (Figure 36).

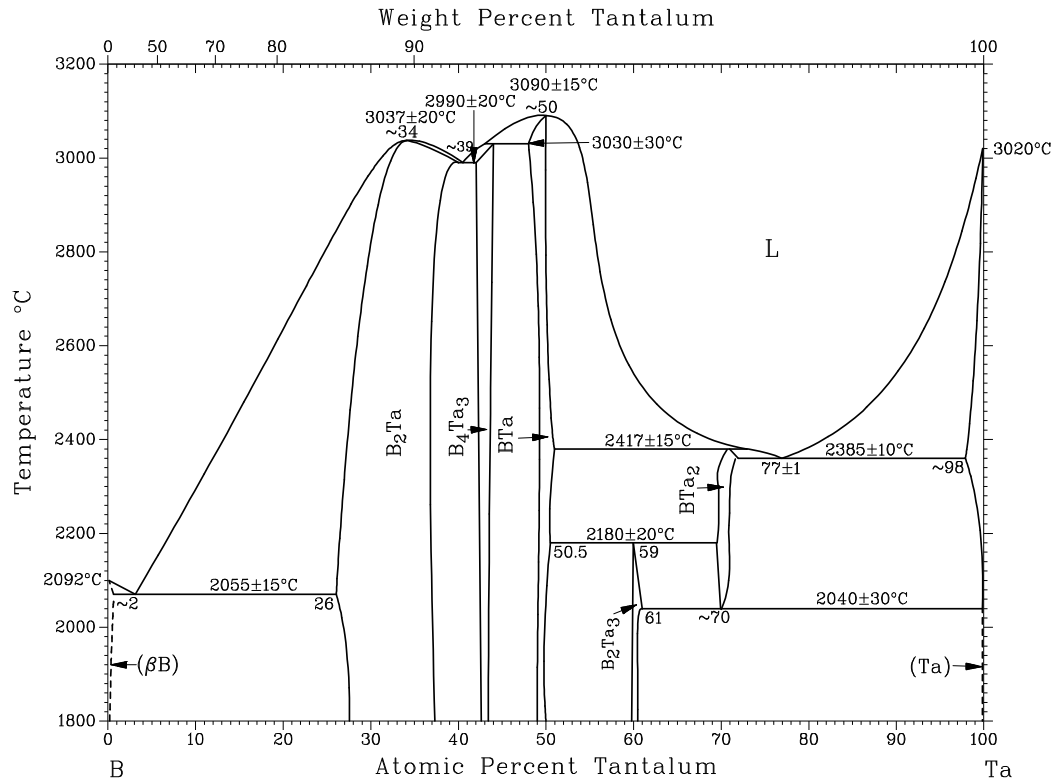


Figure 36: Binary phase diagram of the tantalum - boron system [32].

Known binary tantalum borides are listed in Table 8 with their compositional range and structure type. The systems of tantalum and boron and niobium and boron are closely similar to each other. In addition to the phases known from Nb-B, Ta<sub>2</sub>B is observed in the system. Ta<sub>5</sub>B<sub>6</sub> is not shown in the phase diagram but was observed. Tantalum diboride has the widest compositional stability range in the system.

Table 8: Binary phases known in the tantalum - boron system.

Phase	Composition at. % Ta	Space Group	Structure type
Ta <sub>2</sub> B	69 to 72	<i>I4/mcm</i>	Al <sub>2</sub> Cu
Ta <sub>3</sub> B <sub>2</sub>	60 to 61	<i>P4/mbm</i>	U <sub>3</sub> Si <sub>2</sub>
TaB	48 to 51	<i>Cmcm</i>	CrB
Ta <sub>5</sub> B <sub>6</sub>	?	<i>Cmmm</i>	Ta <sub>5</sub> B <sub>6</sub>
Ta <sub>3</sub> B <sub>4</sub>	41 to 44	<i>Immm</i>	Ta <sub>3</sub> B <sub>4</sub>
TaB <sub>2</sub>	26 to 37	<i>P6/mmm</i>	AlB <sub>2</sub>

#### 4.4.2. Literature review

Ta<sub>2</sub>B was synthesized in 1949<sup>[47]</sup> and reported with a tetragonal structure in space group *I4/mcm* by Kiessling. Kiessling used X-ray powder diffraction data to determine the crystal structure and then in 1972, Havinga *et al.* confirmed the structure by using X-ray diffraction single crystal data<sup>[48]</sup>. Hardy and Hulm reported Ta<sub>2</sub>B to become superconducting at a T<sub>C</sub> of 3.12 K<sup>[49]</sup>.

In 1958, Nowotny firstly synthesized Ta<sub>3</sub>B<sub>2</sub> and used X-ray powder diffraction data to determine the crystal structure<sup>[33]</sup>. Later on, the structure was confirmed by using single crystal X-ray diffraction by Portnoi *et al.*<sup>[50]</sup>. There is no report on the superconductivity of Ta<sub>3</sub>B<sub>2</sub> in literature.

The monoboride of tantalum – TaB – was firstly synthesized by Kiessling in 1949 and its structure was determined in the orthorhombic crystal system with space group *Cmcm*<sup>[47]</sup>. The crystallographic investigation was done by using single crystal X-ray diffraction data. TaB was previously reported as not being superconducting in various reports<sup>[36, 49]</sup>. Although the previous reports were claiming non-superconductivity for TaB, this phase is listed as a superconducting boride with an onset T<sub>C</sub> of 4.0 K in a handbook of condensed matter and material data<sup>[34]</sup>.

Ta<sub>5</sub>B<sub>6</sub> was reported for the first time with its crystal structure by Bolmgren *et al.* in 1990<sup>[46]</sup>. It was described that Ta<sub>5</sub>B<sub>6</sub> crystallizes with orthorhombic symmetry in space group *Cmmm*. The structure was determined using single crystal X-ray diffraction data. As in Ta<sub>3</sub>B<sub>2</sub>, there is no report published on the superconductivity of Ta<sub>5</sub>B<sub>6</sub>.

Kiessling showed the existence of  $Ta_3B_4$  as well as that of  $Ta_2B$  and  $TaB$  for the first time in his publication in 1949 <sup>[47]</sup> and described its orthorhombic structure in space group *Immm*. The crystal structure data was based on the X-ray powder diffraction.  $Ta_3B_4$  was found to be a non-superconducting boride by Mathias and Hulm <sup>[36]</sup>.

The synthesis and characterization of  $TaB_2$  was also done for the first time in 1949 by Kiessling <sup>[47]</sup>. Several investigations were published on the crystal structure of  $TaB_2$  which crystallizes in hexagonal symmetry with space group *P6/mmm*. The structural information was based on X-ray diffraction data of powder and single crystals. The theoretical studies on the superconductivity of  $TaB_2$  were predicting superconductivity at 12 K <sup>[51]</sup>, but the experimental studies are showing contradictory results. Some authors are claiming superconductivity with a  $T_C$  at 9.5 K <sup>[52]</sup> while others reported a  $T_C$  value of 4.4 K (for a sample that contained metallic tantalum) <sup>[53]</sup> or even no superconductivity down to 1.28 K <sup>[36, 54]</sup>.

#### 4.4.3. Synthesis and structural characterization of $Ta_2B$

In the tantalum boron system,  $Ta_2B$  is the phase which has the highest metal to boron ratio. Getting the phase in monophasic form could not be achieved in this work since  $Ta_2B$  has a stability range between 2000 °C and 2400 °C. The product finally obtained contained  $TaB$  and metallic tantalum in addition to  $Ta_2B$ . The latter amounted to approximately 50 % of the product (Figure 37). The synthesis of ditantalum monoboride was done using arc melting as described in section 2.2.2 with a quick cooling procedure.

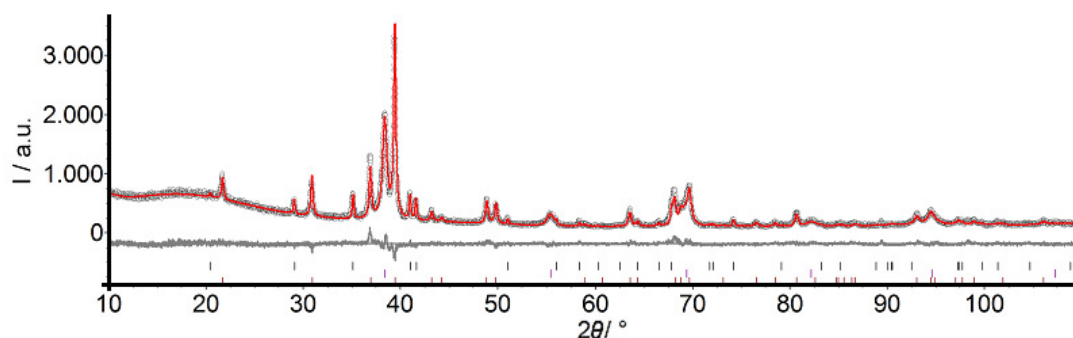


Figure 37: X-ray diffraction pattern of  $Ta_2B$  fitted using the Rietveld method. The black circles are the observed data, the red line is the calculated curve, and the gray curve is the difference curve between the observed and the calculated curves. The tickmarks with different colors at the bottom are representing the positions of the reflections for each phase. (brown =  $Ta_2B$ , purple = Ta, black =  $TaB$ )

Figure 37 shows the X-ray diffraction pattern of a typical product mixture for Ta<sub>2</sub>B. The refinement of the unit cell parameters from the XRD data were done by using the Rietveld method based on the structure model from literature <sup>[47]</sup>. The information from literature was confirmed. Unit cell parameters and residuals of the refinement are given in Table 9.

Table 9: Unit cell parameters and residuals of the refinement of Ta<sub>2</sub>B. Literature <sup>[48]</sup> values are given in brackets.

Phase	Ta <sub>2</sub> B
Diffractometer	STOE Stadi-P-Diffractometer
Wavelength / Å	1.54056
Temperature / K	293
Max. 2θ / °	110
R <sub>exp</sub>	5.84
R <sub>wp</sub>	6.98
R <sub>p</sub>	5.36
GOF	1.20
Crystal system	Tetragonal
Space group	<i>I4/mcm</i> (140)
<i>a</i> / Å	5.7835(2) - [5.783]
<i>c</i> / Å	4.8679(2) - [4.866]
<i>V</i> / Å <sup>3</sup>	162.83(2) - [162.73]
Calc. density / g cm <sup>-1</sup>	15.203(2)
Sample code	EF024

SEM images of the product which was ground in a boron carbide mortar showed non-uniform particle sizes. The shapes of the particles were not well-defined. EDX analysis did not show any impurity (Figure 38).

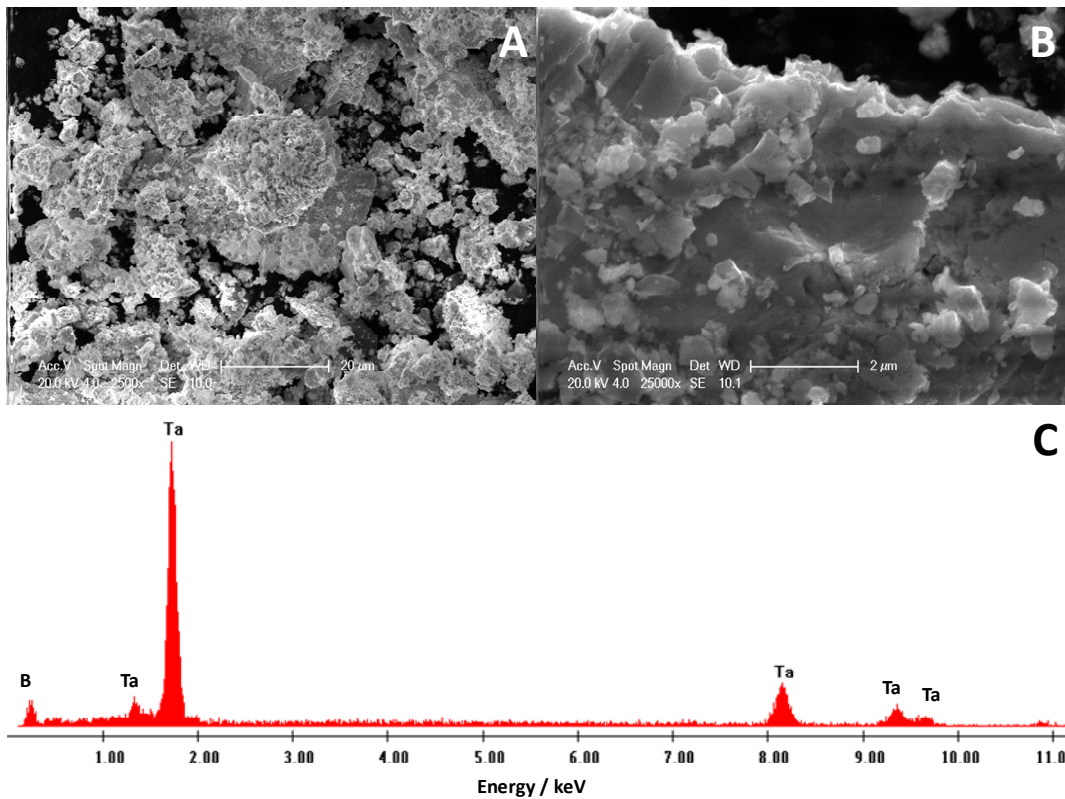


Figure 38: SEM images of Ta<sub>2</sub>B in magnification (A) 2500, (B) 25000 and (C) EDX analysis.

#### 4.4.4. Synthesis, structural characterization and superconductivity measurements of TaB

The synthesis of tantalum monoboride was possible in the electric arc and in quartz ampoules. In order to get monophasic tantalum monoboride, an excess of boron (up to 30 %) was used in the mixture of the starting materials. Since the compositional range is very narrow, the amount of reactants was very critical.

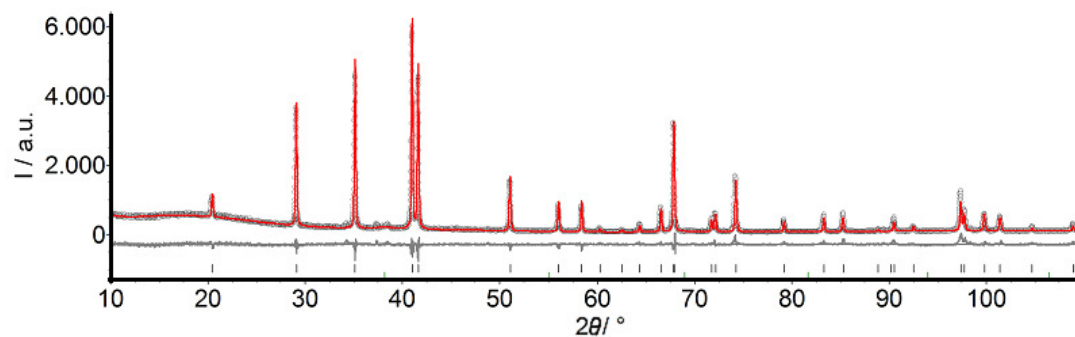


Figure 39: X-ray diffraction pattern of TaB fitted using the Rietveld method. The black circles are the observed data, the red line is the calculated curve, and the gray curve is the difference curve between the observed and the calculated curves. The tickmarks at the bottom are representing the positions of the reflections for TaB phase. (green = Ta, black = TaB)

As it can be seen in Figure 39, tantalum monoboride which was synthesized via arc melting was well crystalline but the sample was containing some traces of elemental tantalum as well. The refinement of the unit cell parameters based on XRD data was done by using the Rietveld method and the structure model from literature <sup>[47]</sup>. The structure information from literature was confirmed. Unit cell parameters and residuals of the refinement are given in Table 10.

Table 10: Unit cell parameters and residuals of the refinement of TaB. Literature <sup>[55]</sup> values are given in brackets.

Phase	TaB
Diffractometer	STOE Stadi-P-Diffractometer
Wavelength / Å	1.54056
Temperature / K	293
Max. $2\theta / ^\circ$	110
$R_{\text{exp}}$	6.13
$R_{\text{wp}}$	9.63
$R_{\text{p}}$	6.92
GOF	1.57
Crystal system	Orthorhombic
Space group	<i>Cmcm</i> (63)
$a / \text{Å}$	3.2792(1) – [3.280(1)]
$b / \text{Å}$	8.6732(2) – [8.670(3)]
$c / \text{Å}$	3.1568(1) – [3.155(2)]
$V / \text{Å}^3$	89.784(2) – [89.72]
Calc. density / $\text{g cm}^{-3}$	13.765(1)
Sample code	EF009

SEM images of the sample which was ground in a boron carbide mortar showed non-uniform particle sizes. The shapes of the particles were not well-defined. EDX analysis showed signal only for tantalum and boron (Figure 40).

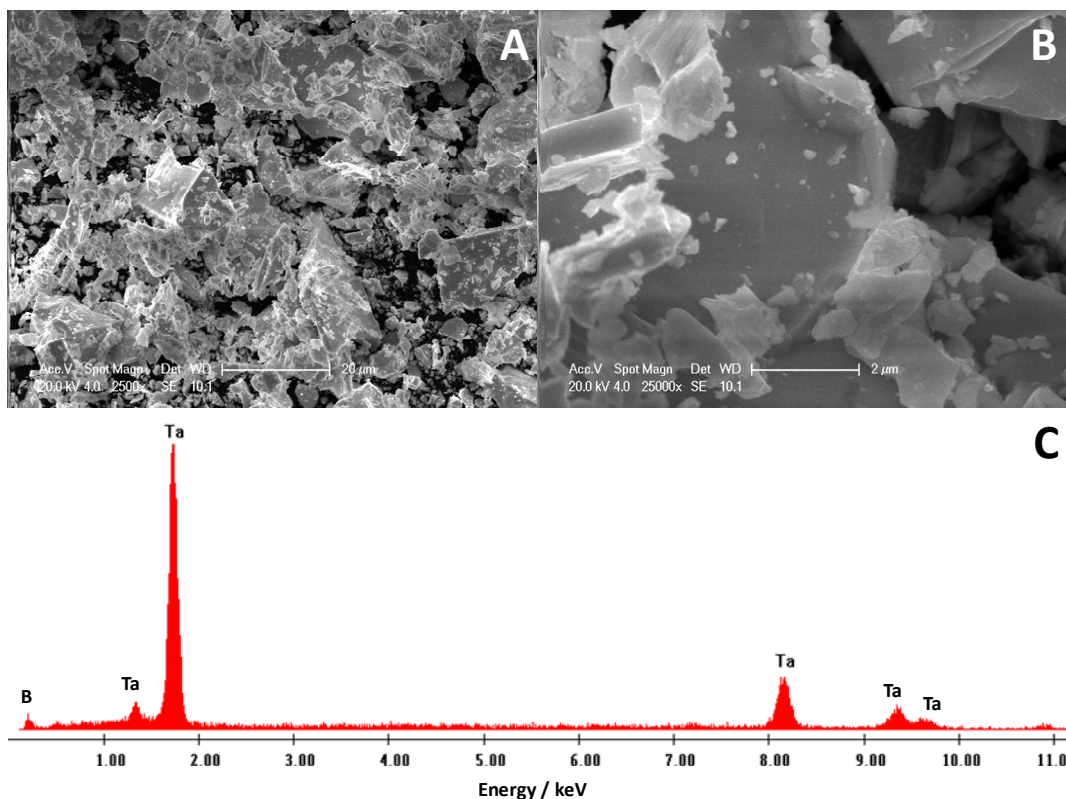


Figure 40: SEM images of TaB in magnification (A) 2500, (B) 25000 and (C) EDX analysis.

A well-crystalline TaB sample which contained traces of elemental tantalum was analyzed for possible superconductivity. A zero-field cooled measurement was done between 1.8 K and 15 K. The measurement showed a clear and sharp transition with an onset temperature of 4.2 K (Figure 41). This  $T_c$  value was previously assigned to elemental tantalum<sup>[34]</sup>. Since there is no additional transition in the magnetization versus temperature graph, it is not possible to conclude that TaB becomes superconducting. This finding supports the previous reports on non-superconductivity for TaB<sup>[36, 49]</sup>.

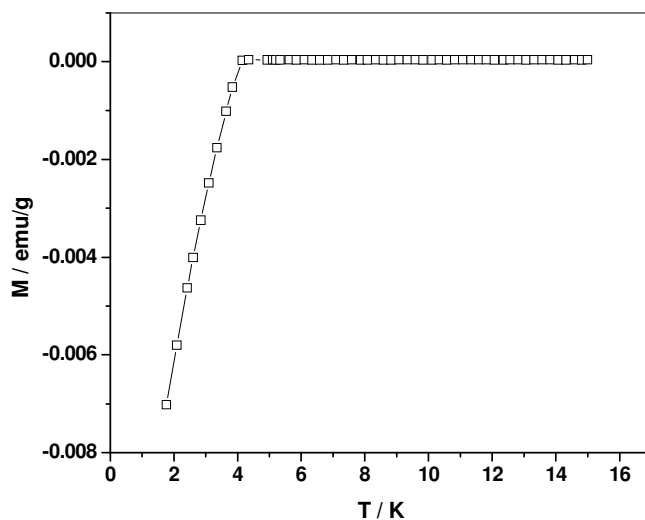


Figure 41: Superconductivity measurement (ZFC) for TaB.

#### 4.4.5. Synthesis and structural characterization of Ta<sub>3</sub>B<sub>4</sub>

Ta<sub>3</sub>B<sub>4</sub> was obtained as the major phase (approximately 60 %) in the products of the reaction of stoichiometric amounts of Ta and B in the electric arc or in quartz ampoules at 1050 °C (See 2.2.2 and 2.3.2). The second phase in the product was found to be TaB<sub>2</sub>.

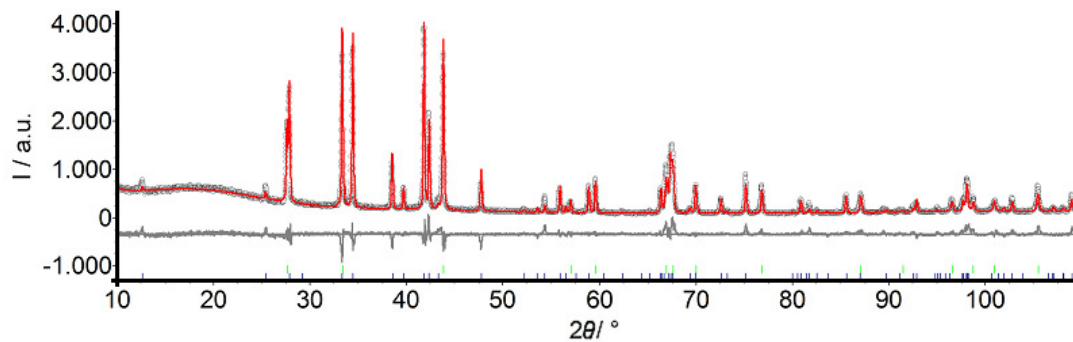


Figure 42: X-ray diffraction pattern of Ta<sub>3</sub>B<sub>4</sub> fitted using the Rietveld method. The black circles are the observed data, the red line is the calculated curve, and the gray curve is the difference curve between the observed and the calculated curves. The tickmarks with different colors at the bottom are representing the positions of the reflections for each phase. (blue = Ta<sub>3</sub>B<sub>4</sub>, green = TaB<sub>2</sub>)

The refinement of the unit cell parameters was done by using the Rietveld method based on the structure model from literature <sup>[55]</sup>. The information from literature was

confirmed. Refined unit cell parameters and residuals of the refinement are given in Table 11.

Table 11: Unit cell parameters and residuals of the refinement of Ta<sub>3</sub>B<sub>4</sub>. Literature <sup>[55]</sup> values are given in brackets.

Phase	Ta <sub>3</sub> B <sub>4</sub>
Diffractometer	STOE Stadi-P-Diffractometer
Wavelength / Å	1.54056
Temperature / K	293
Max. 2θ / °	110
R <sub>exp</sub>	5.86
R <sub>wp</sub>	11.22
R <sub>p</sub>	8.09
GOF	1.92
Crystal system	orthorhombic
Space group	<i>Immm</i> (71)
<i>a</i> / Å	3.2853(1) – [3.2914(8)]
<i>b</i> / Å	14.007(1) – [13.994(3)]
<i>c</i> / Å	3.1332(1) – [3.1327(6)]
<i>V</i> / Å <sup>3</sup>	144.18(1) – [144.29]
Calc. density / g cm <sup>-1</sup>	13.500(1)
Sample code	EF027

Morphological analysis of the Ta<sub>3</sub>B<sub>4</sub> sample by using SEM showed the presence of big particles with sharp edges. There was no agglomeration in the sample and the particles looked compact. EDX analysis did not show any impurity signal but only tantalum and boron (Figure 43).

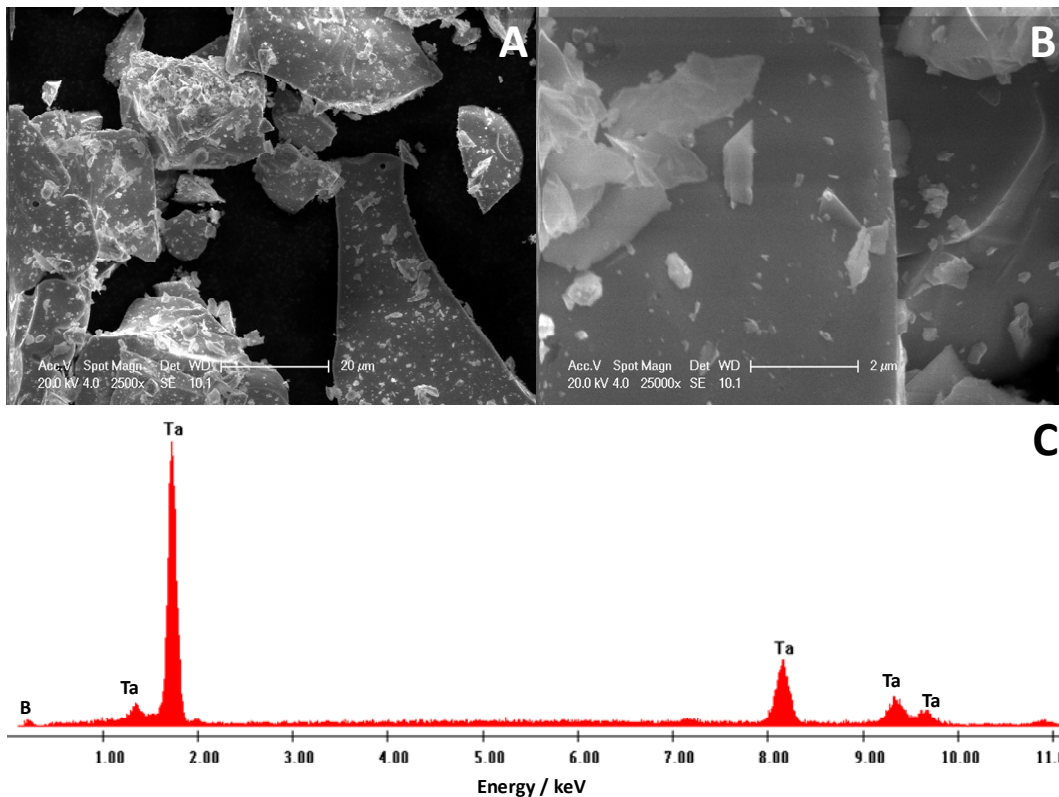


Figure 43: SEM images of  $Ta_3B_4$  in magnification (A) 2500, (B) 25000 and (C) EDX analysis.

#### 4.4.6. Synthesis, structural characterization and superconductivity measurements of $TaB_{2\pm x}$

Tantalum diboride is the phase with the widest compositional range in the phase diagram of tantalum and boron. Because of the wide compositional range compared to other phases in the system the synthesis of tantalum diboride is easier. But, when using different ratios of starting materials differences in the occupancies of the atomic sites result. The ratios of boron to tantalum were varied between 2.0 and 2.6, and this resulted in the formation of  $TaB_{2+x}$  with the same crystal structure but slightly different lattice parameters.

The synthesis of the monophasic samples of  $TaB_{2+x}$  was performed with the ratios of Ta to B varying between 2.0:1 and 2.6:1 in the electric arc or in quartz ampoules at 1050 °C (See 2.2.2 and 2.3.2).

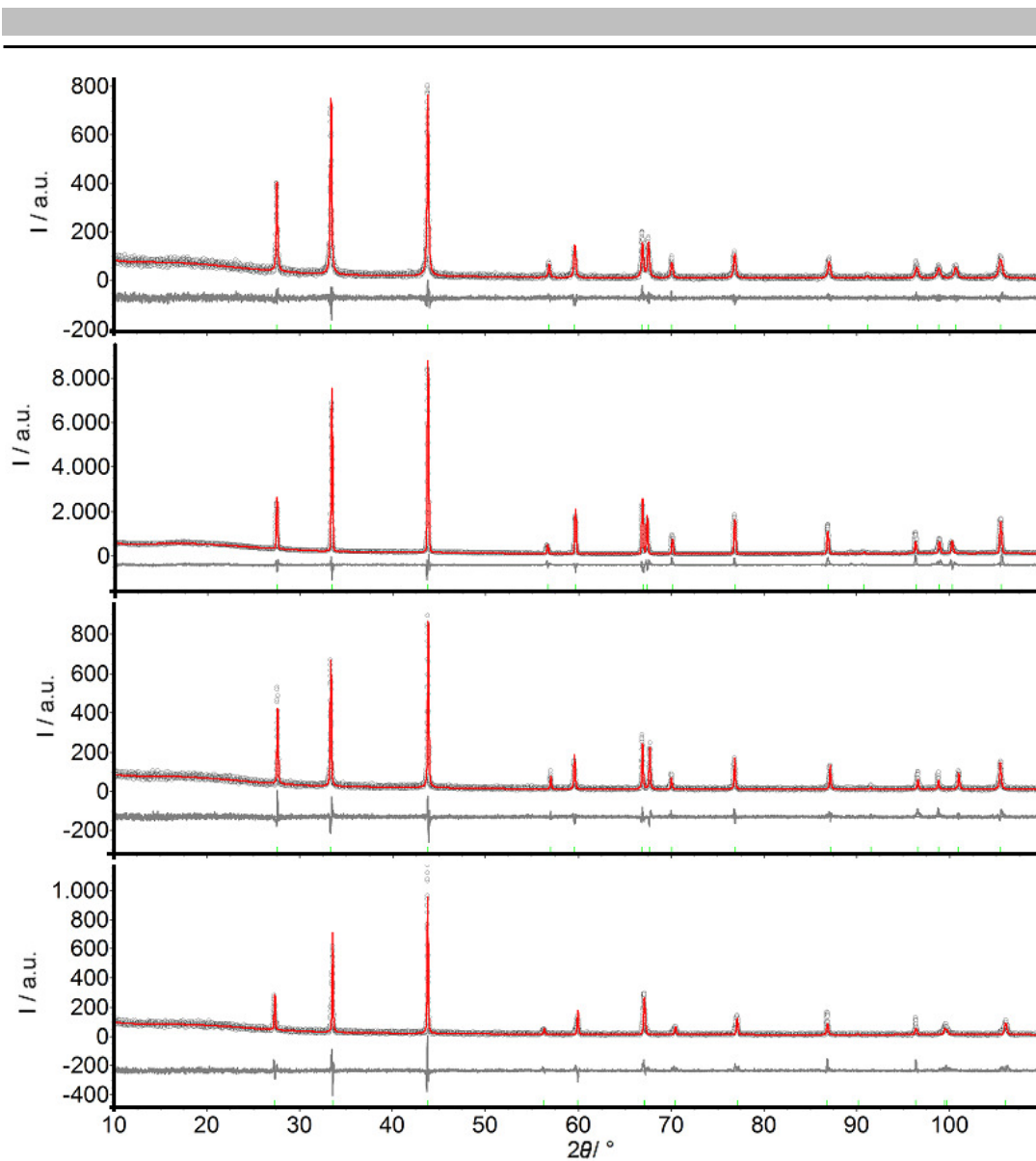


Figure 44: Rietveld analysis for TaB<sub>2±x</sub> samples produced with varying amount of boron. The black circles are the observed data, the red line is the calculated curve, and the gray curve is the difference curve between the observed and the calculated curves. The tickmarks at the bottom are representing the positions of the reflections for TaB<sub>2</sub> phase. B:Ta = 2.0 (top), = 2.4 (second), = 2.5 (third), = 2.6 (bottom)

Table 12: The refined unit cell parameters and residuals of the refinement for three different TaB<sub>2</sub> samples with varying boron to tantalum ratios

Phase	TaB <sub>2</sub>			
Diffractometer	STOE Stadi-P-Diffractometer			
Wavelength / Å	1.54056			
Temperature / K	293			
Max. 2θ / °	110			
Crystal system	hexagonal			
Space group	<i>P6/mmm</i> (191)			
Starting composition, Ta:B	1:2.0	1:2.4	1:2.5	1:2.6
R <sub>exp</sub>	17.63	18.94	18.00	17.39
R <sub>wp</sub>	17.90	23.07	20.40	20.83
R <sub>p</sub>	13.20	16.86	15.35	15.07
GOF	1.02	1.22	1.13	1.20
<i>a</i> / Å	3.0985(1)	3.0951(1)	3.0998(1)	3.0834(1)
<i>c</i> / Å	3.2353(2)	3.2442(1)	3.2266(1)	3.2643(2)
<i>V</i> / Å <sup>3</sup>	26.899(2)	26.914(2)	26.850(2)	26.878(2)
Calc. density / g cm <sup>-1</sup>	12.505 (1)	12.498(1)	12.528(1)	12.515(1)
Sample code	EF003	EF019	EF020	EF021

---

Morphological properties were analyzed with SEM for TaB<sub>2</sub> samples obtained in sealed quartz ampoules and by arc melting to see if there were differences between the final products. Samples obtained from reactions in quartz ampoules showed big particles around 40 micrometers which were composed of agglomerated particles with a size of around 500 nm (Figure 45 A, and B). In the sample which was obtained by arc melting the particles were big and compact with sharp edges (Figure 45, D and E). This type of particle morphology was typical for the samples obtained in arc melting. For both of the samples EDX analysis showed signals for tantalum and boron but not other elements as impurities (Figure 45, C and F).

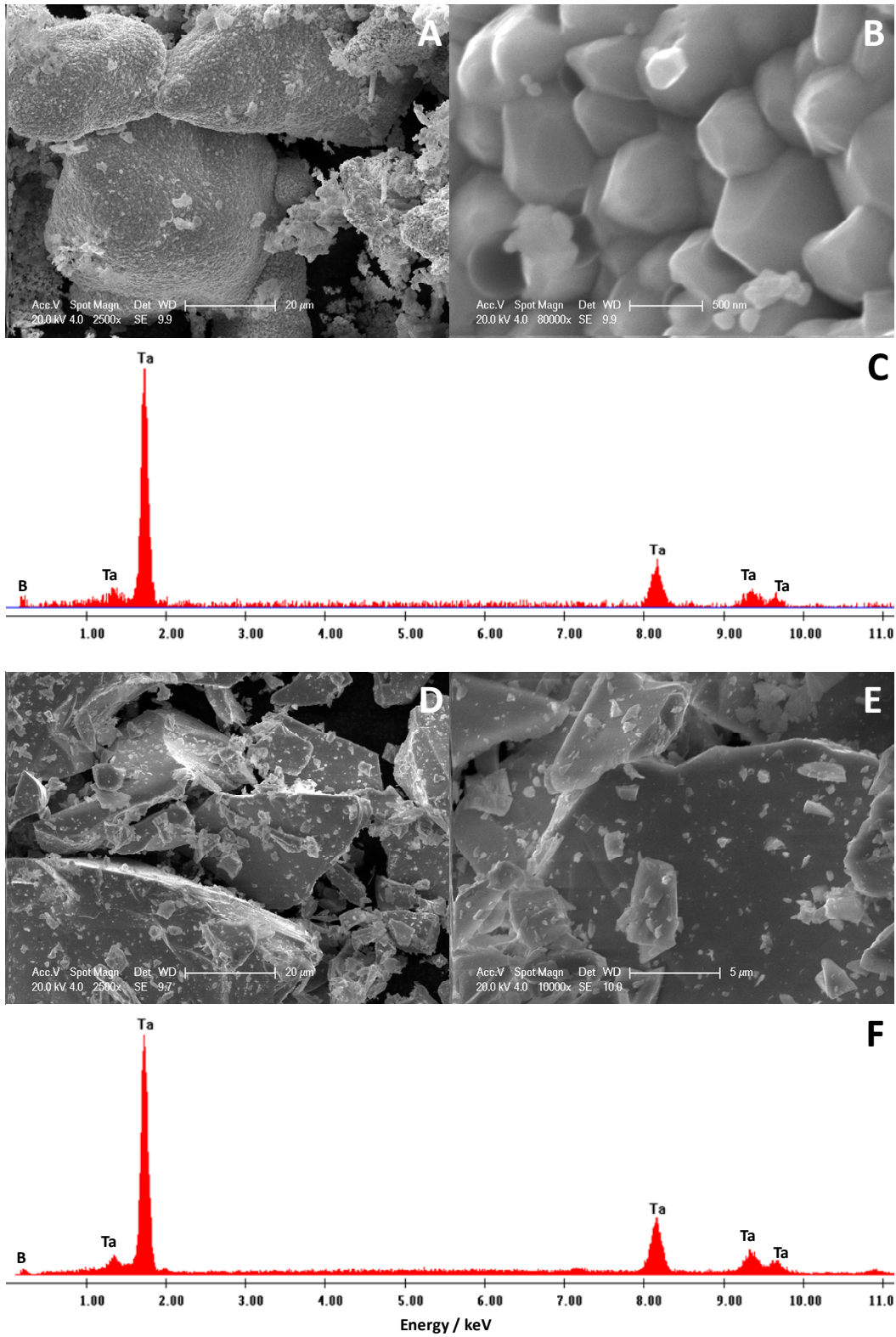


Figure 45: SEM images of TaB<sub>2</sub> obtained in quartz ampoule with a magnification of (A) 2500, (B) 80000 and (C) EDX analysis and TaB<sub>2</sub> obtained in an electric arc with a magnification of (D) 2500, (E) 10000 and (F) EDX analysis.

The structure of tantalum diboride is isotypic to niobium diboride. Data on the X-ray diffraction analysis can be found in Table 12. Zero-field cooled measurements were done for many  $\text{TaB}_{2\pm x}$  samples with slightly different lattice parameters, but in none of them a transition into a superconducting state was observed (Figure 46).

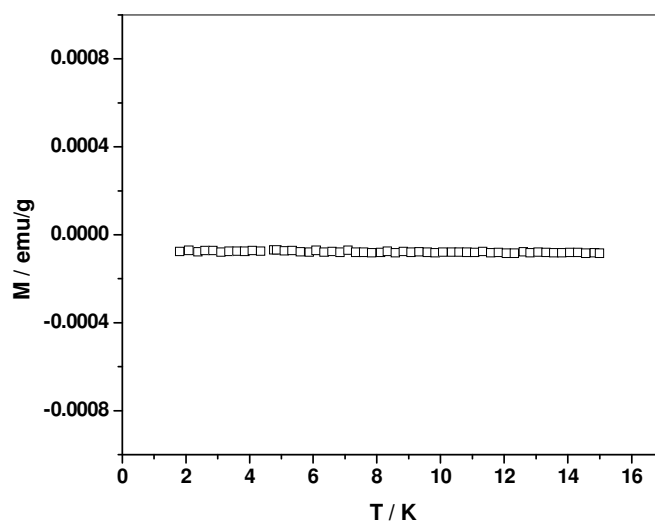


Figure 46: Superconductivity measurement (ZFC) for  $\text{TaB}_2$ .

#### 4.4.7. Concluding remarks on the Ta-B system

It was difficult to obtain pure binary phases in the tantalum – boron system, due to the narrow compositional and thermal stability ranges.  $\text{Ta}_3\text{B}_2$  and  $\text{Ta}_5\text{B}_6$  could not be synthesized even as mixtures with other tantalum borides. Syntheses of  $\text{Ta}_2\text{B}$  and  $\text{TaB}$  were successful although the samples contained elemental tantalum and neighboring phases as side products. All of the trials to improve the synthesis of  $\text{Ta}_2\text{B}$  and  $\text{TaB}$  failed.  $\text{Ta}_3\text{B}_4$  was also synthesized as a mixture with  $\text{TaB}_2$ . The only phases which were obtained as monophasic products were  $\text{TaB}_{2\pm x}$  with slightly different boron contents.

Although, according to the phase diagram  $\text{Ta}_3\text{B}_2$  and  $\text{Ta}_5\text{B}_6$  do exist, those phases were not obtained in this work. None of the three synthetic approaches resulted in the formation of  $\text{Ta}_3\text{B}_2$  and  $\text{Ta}_5\text{B}_6$ .

---

SEM of the samples obtained by arc melting showed big and compact particles with sharp edges in the SEM images. There were clear differences in the morphologies of the samples produced in different furnaces like electric arc and high frequency induction furnaces. EDX analysis disproved the existence of any impurities in the sample.

The interpretation of measurements of superconductivity is difficult if more than one phase in a mixture is exhibiting superconductivity. Because of that, superconductivity measurements were done only for TaB and several samples of TaB<sub>2±x</sub>. TaB contained an impurity of elemental tantalum and showed a T<sub>C</sub> of 4.2 K. No superconducting transition was observed for TaB or TaB<sub>2±x</sub>.

## 4.5. Molybdenum-boron system

### 4.5.1. Phase diagram of the Mo-B system

The phase diagram of molybdenum and boron (Figure 47) shows nine different phases including elemental molybdenum and boron.

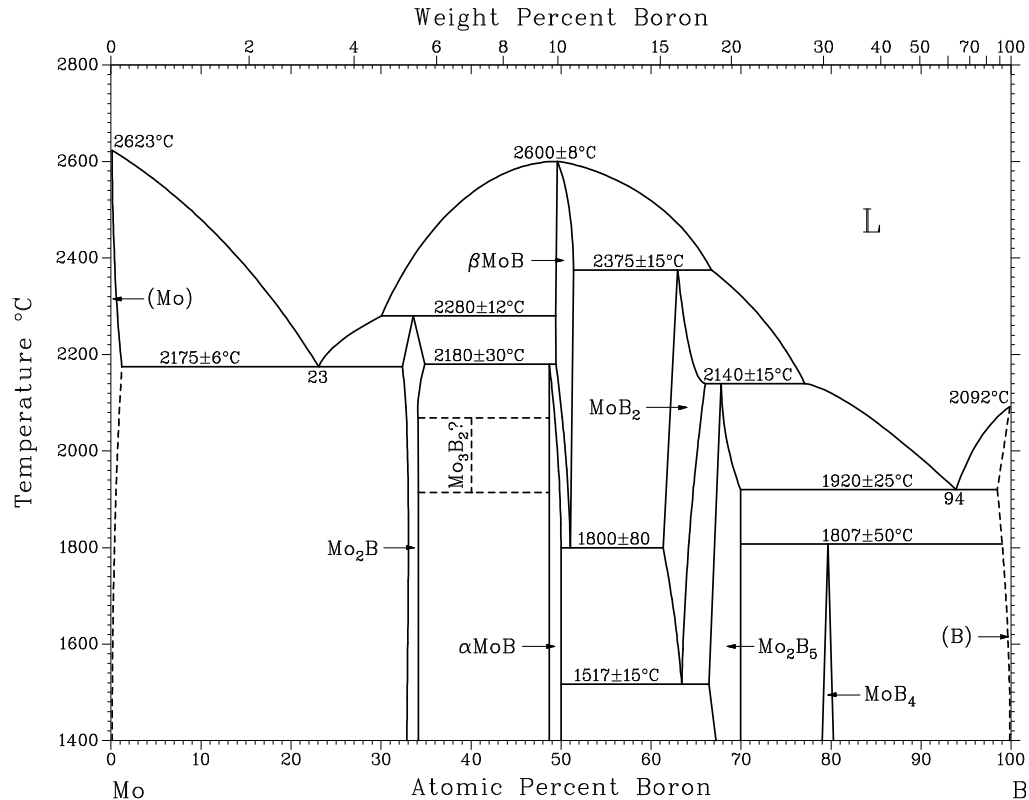


Figure 47: Binary phase diagram of the molybdenum - boron system <sup>[32]</sup>.

Known binary molybdenum borides are listed in Table 13 with their compositional range and structure type. Mo<sub>3</sub>B<sub>2</sub> is one of the most questionable phases in the system. In the phase diagram it is mentioned with a question mark and the stability range is indicated with dashed lines. Although it was found to exist and the structure was determined using a single crystal, there is not much information in the literature except for theoretical calculations on this phase.

In the molybdenum-boron binary system, there are two different modifications of molybdenum monoboride. The high temperature phase of MoB which is called  $\beta$ -MoB has

an orthorhombic crystal structure and the low temperature phase which is called  $\alpha$ -MoB has a tetragonal crystal structure. Orthorhombic and tetragonal molybdenum monoborides show a small difference concerning their compositional stability range (Table 13).

In the range of a molybdenum to boron ratio around 1:2, there are two different diborides of molybdenum. One of them is the stoichiometric diboride MoB<sub>2</sub> and the other one is a nonstoichiometric phase which was described as Mo<sub>2</sub>B<sub>5</sub>. Recently, Mo<sub>2</sub>B<sub>5</sub> was reinvestigated with neutron diffraction and found to be Mo<sub>2</sub>B<sub>4</sub> [31]. MoB<sub>2</sub> has a higher range of thermal stability and according to the phase diagram the composition of Mo<sub>2</sub>B<sub>4</sub> should be slightly richer in boron than the formula suggests.

Table 13: Binary phases known in the molybdenum - boron system.

Phase	Composition at. % B	Space Group	Structure type
Mo <sub>2</sub> B	32 to 35	<i>I4/mcm</i>	Al <sub>2</sub> Cu
Mo <sub>3</sub> B <sub>2</sub>	40	<i>P4/mbm</i>	U <sub>3</sub> Si <sub>2</sub>
$\alpha$ -MoB	48.5 to 50	<i>I4<sub>1</sub>/amd</i>	MoB
$\beta$ -MoB	49 to 51.5	<i>Cmcm</i>	CrB
MoB <sub>2</sub>	61 to 66	<i>P6/mmm</i>	AlB <sub>2</sub>
Mo <sub>2</sub> B <sub>4</sub>	66.5 to 70	<i>R<math>\bar{3}m</math></i>	CaSi <sub>2</sub>
MoB <sub>4</sub>	79 to 80.5	<i>P6<sub>3</sub>/mmc</i>	-

#### 4.5.2. Literature review

Mo<sub>2</sub>B was firstly synthesized and characterized by Kiessling in 1947 [56]. Its crystal structure has tetragonal symmetry (space group *I4/mcm*) The structure determination was done from single crystal X-ray diffraction. In 1972 Havinga *et al.* confirmed the structure [48]. A T<sub>C</sub> value of 5.8 K is reported for Mo<sub>2</sub>B by Cai *et al.* [57] and Engelhardt [58]. On the other hand Matthias and Hulm reported a lower T<sub>C</sub> value of 4.74 K and the compound is listed as becoming superconducting at 5.1 K in the Condensed Matter and Materials Data book [34].

The low-temperature form of MoB was reported by Kiessling in 1947 with a tetragonal crystal structure with space group *I4<sub>1</sub>/amd* [56]. Then in 1963 Rudy *et al.* reported the presence of the high-temperature form of the monoboride of molybdenum with a different crystal structure type which is classified as CrB-type. The structure of the high-

---

temperature form of MoB was described in the orthorhombic crystal system with space group  $Cmcm$  [44]. Crystal structure analysis was done from X-ray diffraction powder data. Tetragonal MoB was reported to be non-superconducting down to temperatures as low as 1.8 K [36, 59], but another author found it to become superconducting with a  $T_C$  of 4.4 K [60].

$Mo_2B_4$  is one of the diboride phases in the molybdenum-boron system which was previously known as  $Mo_2B_5$ . This phase was firstly synthesized and characterized by Kiessling in 1947. It crystallizes with a trigonal crystal structure in space group  $R\bar{3}m$  [56]. Structural information was obtained from single crystal X-ray diffraction data. There were some doubts about the exact stoichiometry of the compound. The question mark was on the presence of the crystallographic position of one of the boron atoms in the unit cell. The existence of this doubtful boron atom was disproved by using synchrotron and neutron data by Frotscher *et al.* in 2007 [31].  $Mo_2B_4 / Mo_2B_5$  was reported by Muzzy *et al.* to remain non-superconducting down to 1.8 K [61].  $MoB_2$  is the second diboride phase.  $MoB_2$  which is actually a non-stoichiometric phase was firstly reported by Bertaut *et al.* [62] and described with hexagonal symmetry (space group  $P6/mmm$ ). It crystallizes in the  $AlB_2$ -structure type and was found to be non-superconducting, but the addition of Zr into the system resulted in the appearance of superconductivity at 5.9 K [61]. With 15 % deficiency of metal atoms in zirconium-stabilized  $MoB_2$ ,  $T_C$  was increased up to 8.2 K.

#### **4.5.3. Synthesis, structural characterization and superconductivity measurements of $Mo_2B$**

The synthesis of dimolybdenum monoboride ( $Mo_2B$ ) was possible in quartz ampoules and in an electric arc. Samples of  $Mo_2B$  which were produced by arc melting contained traces of molybdenum metal. Increasing the boron amount in the mixture of starting materials resulted in the formation of the high-temperature form of molybdenum monoboride and a small amount of molybdenum was also observable in the product. Since the temperature reached the melting temperature of the mixture  $Mo_2B$  decomposes at 2280 °C. In the electric arc higher temperatures were obtained orthorhombic MoB and Mo crystallizes in addition to  $Mo_2B$  upon cooling. The product which was produced at lower temperature as 1050 °C for 3 days in quartz ampoules contained traces of the low-temperature form of MoB.

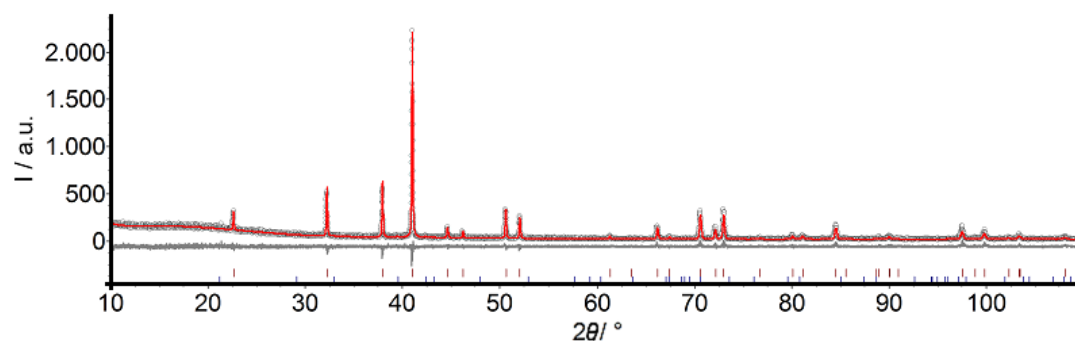


Figure 48: X-ray diffraction pattern of Mo<sub>2</sub>B fitted using the Rietveld method. The black circles are the observed data, the red line is the calculated curve, and the gray curve is the difference curve between the observed and the calculated curves. The tickmarks with different colors at the bottom are representing the positions of the reflections for each phase. (blue = MoB (tetragonal), brown = Mo<sub>2</sub>B)

As can be seen in Figure 48, the X-ray diffraction powder data of the product shows dimolybdenum monoboride and traces of tetragonal MoB. The product was well-crystalline. The refinement of the unit cell parameters from XRD powder data was done by using the Rietveld method. The literature information on the crystal structure was confirmed. Refined unit cell parameters and residuals of the refinement are given in Table 14.

Table 14: Unit cell parameters and residuals of the refinement of Mo<sub>2</sub>B. Literature <sup>[48]</sup> values are given in brackets.

Phase	Mo <sub>2</sub> B
Diffractometer	STOE Stadi-P-Diffractometer
Wavelength / Å	1.54056
Temperature / K	293
Max. 2θ / °	110
R <sub>exp</sub>	13.03
R <sub>wp</sub>	12.96
R <sub>p</sub>	9.55
GOF	0.99
Crystal system	tetragonal
Space group	<i>I4/mcm</i> (140)
<i>a</i> / Å	5.5491(1) – [5.547]
<i>c</i> / Å	4.7378(1) – [4.739]
<i>V</i> / Å <sup>3</sup>	145.88(1) – [145.82]
Calc. density / g cm <sup>-1</sup>	9.2287(4)
Sample code	MK200

---

A zero-field cooled measurement for Mo<sub>2</sub>B was done between 1.8 K and 15 K. The superconductivity measurement showed a clear and sharp transition to superconductivity with an onset temperature of 5.85 K. Although the sample was containing traces of the tetragonal modification of MoB, the transition was assigned to Mo<sub>2</sub>B. Only one step was detected. The observable effect was too strong to be caused by an impurity. Mo<sub>2</sub>B becomes superconducting below 5.85 K (Figure 49). This finding is in accordance with the report of Engelhardt<sup>[58]</sup> on the superconductivity of Mo<sub>2</sub>B at 5.86 K.

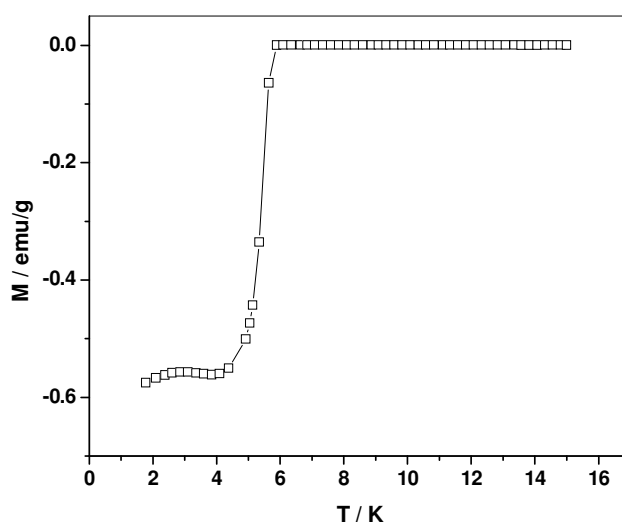


Figure 49: Superconductivity measurement (ZFC) for Mo<sub>2</sub>B.

#### 4.5.4. Synthesis, structural characterization and superconductivity measurements of $\beta$ -MoB

The synthesis of the high-temperature form of molybdenum monoboride ( $\beta$ -MoB) was possible by arc melting. To produce  $\beta$ -MoB an excess of boron of 10 % was used in the starting mixture due to the boron loss during reaction. The product was phase-pure and well-crystalline as can be seen in the X-ray pattern (Figure 50).

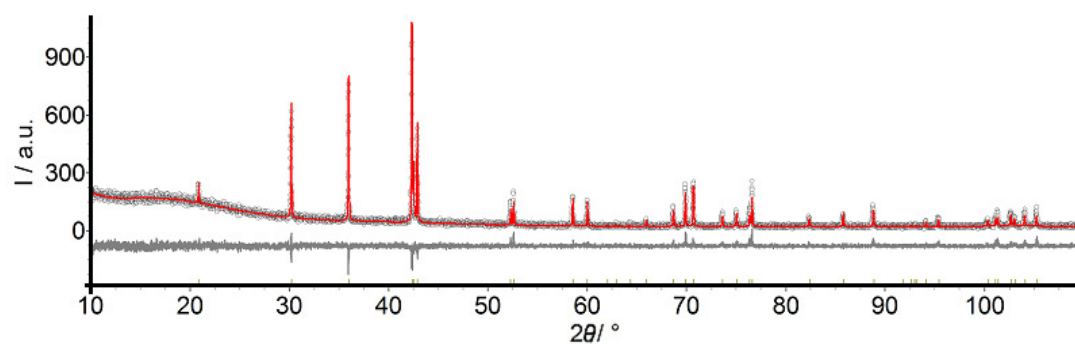


Figure 50: X-ray diffraction pattern of  $\beta$ -MoB fitted using the Rietveld method. The black circles are the observed data, the red line is the calculated curve, and the gray curve is the difference curve between the observed and the calculated curves. The tickmarks at the bottom are representing the positions of the reflections for the phase.

The refinement of the unit cell parameters from the XRD data were done by using the Rietveld method based on the structure model from literature <sup>[44]</sup>. The information from literature was confirmed. Unit cell parameters and residuals of the refinement are given in Table 15.

Table 15: Unit cell parameters and residuals of the refinement of  $\beta$ -MoB. Literature <sup>[44]</sup> values are given in brackets.

Phase	MoB
Diffractometer	STOE Stadi-P-Diffractometer
Wavelength / Å	1.54056
Temperature / K	293
Max. $2\theta$ / °	110
R <sub>exp</sub>	13.05
R <sub>wp</sub>	13.25
R <sub>p</sub>	9.78
GOF	1.02
Crystal system	orthorhombic
Space group	<i>Cmcm</i> (63)
<i>a</i> / Å	3.1482(1) – [3.151]
<i>b</i> / Å	8.4858(2) – [8.470]
<i>c</i> / Å	3.0778(1) – [3.082]
<i>V</i> / Å <sup>3</sup>	82.223(3) – [82.26]
Calc. density / g cm <sup>-1</sup>	8.6237(3)
Sample code	MC008

Morphological analysis of the  $\beta$ -MoB sample showed big particles with sharp edges. There was no agglomeration in the sample and the particles looked compact. EDX analysis did not show any impurity signals of other elements but only molybdenum and boron (Figure 51). A trace of oxygen is attributed to carbon tape that was used.

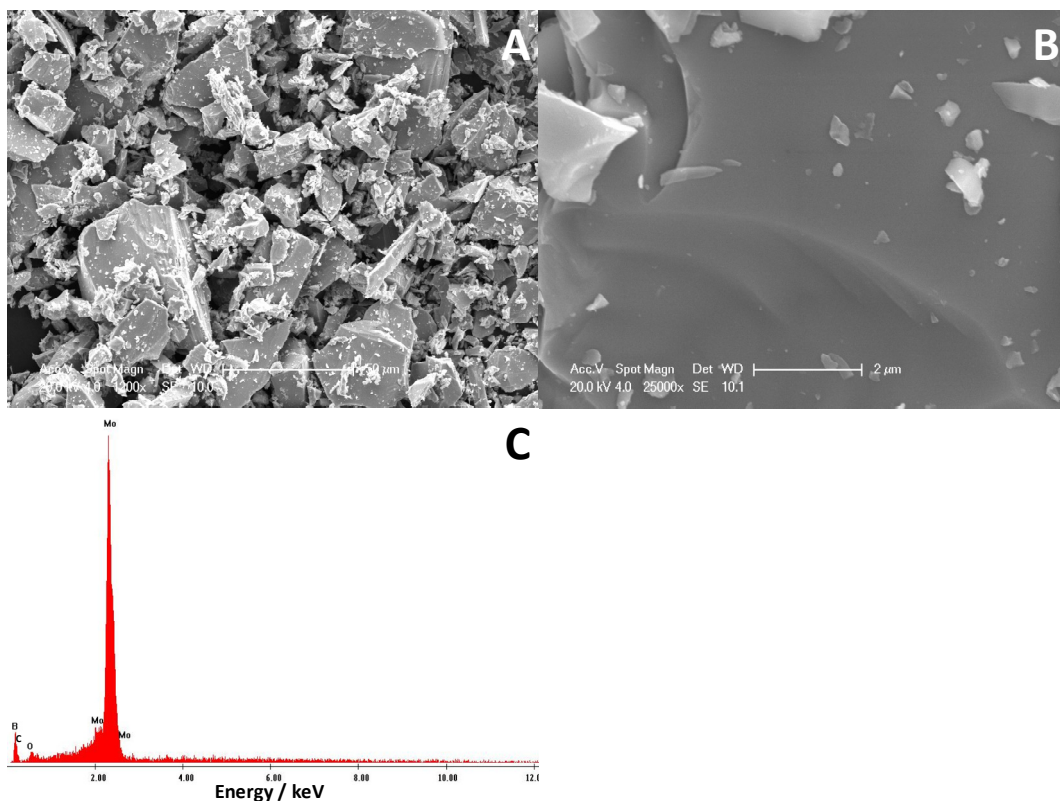


Figure 51: SEM images of  $\beta$ -MoB with a magnification of (A) 1200, (B) 25000 and (C) EDX analysis.

$\beta$ -MoB with orthorhombic crystal symmetry was analyzed for possible superconductivity. A zero-field cooled measurement was done between 1.8 K and 15 K for the sample. The superconductivity measurement showed a clear and sharp transition with an onset temperature of 2.4 K (Figure 52). This finding is the first observation of superconductivity for orthorhombic MoB. Although there were some reports for this phase claiming that it does not become superconducting<sup>[36, 49]</sup>, the reproducibility of our result for several times and the purity of the sample assure the conclusion of superconductivity in orthorhombic MoB below 2.4 K.

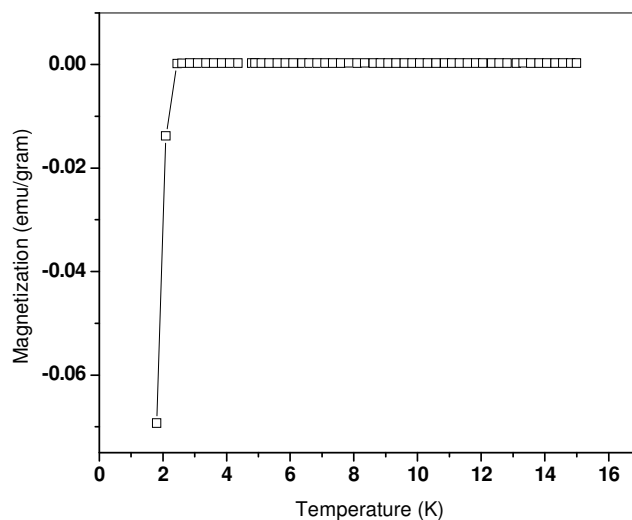


Figure 52: Superconductivity measurement (ZFC) for  $\beta$ -MoB.

#### 4.5.5. Synthesis, structural characterization and superconductivity measurement of $\alpha$ -MoB

The synthesis of the low-temperature form of molybdenum monoboride ( $\alpha$ -MoB) was performed at 1050 °C in quartz ampoules (three days). The reaction took place in the presence of iodine as a mineralizing agent and an excess of 10 to 20 % boron. The sample was phase pure but the X-ray diffraction data indicates a low degree of crystallinity of the sample (Figure 53).

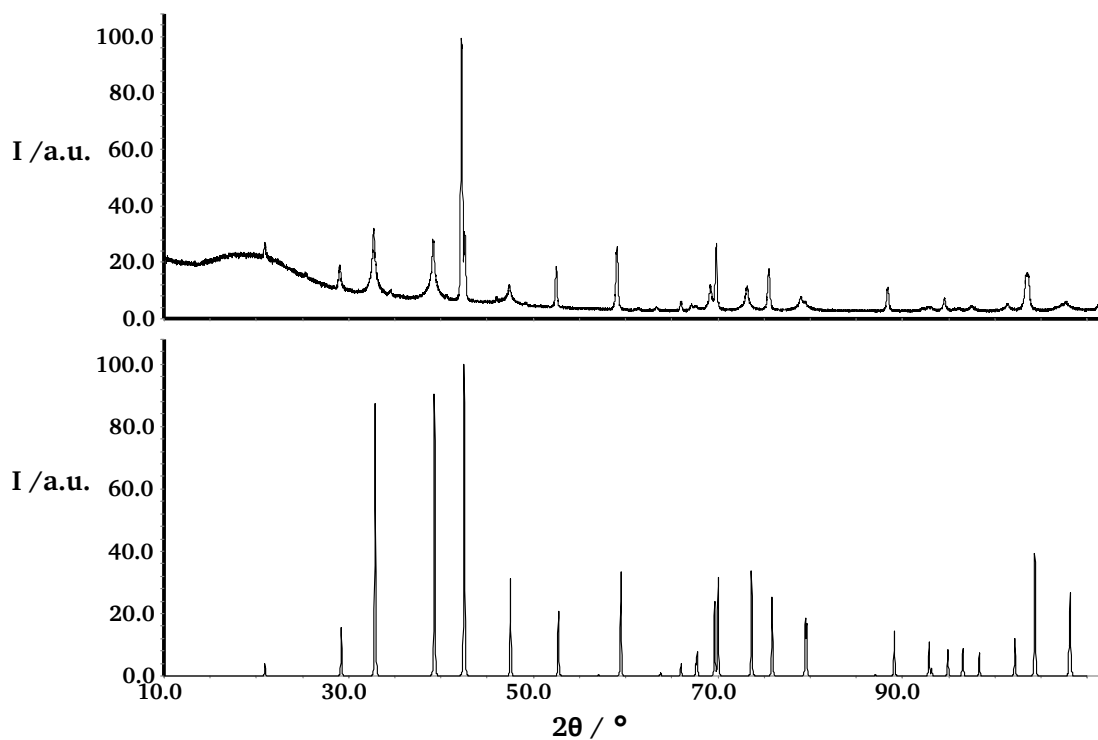


Figure 53: Experimental XRD pattern (top) and the theoretical pattern<sup>[56]</sup> (below) of  $\alpha$ -MoB.

The peak positions of the observed powder pattern confirm those described in literature. The reflections showed different half widths and the Rietveld refinement was not successful.

Morphological analysis of the sample of  $\alpha$ -MoB showed highly agglomerated, very small particles with sizes of 100 to 200 nm. Particle size of  $\alpha$ -MoB was calculated as  $\sim 80$  nm by Scherrer equation using XRD pattern. The shape of the spheres in Figure 54 (A) was identical with the original shape of the molybdenum powder used in the reactions. In order to get a high resolution image from the sample and to prevent charging on it, the sample was sputtered with gold. EDX analysis did not show the presence of any other element than molybdenum, boron and gold (Figure 54).

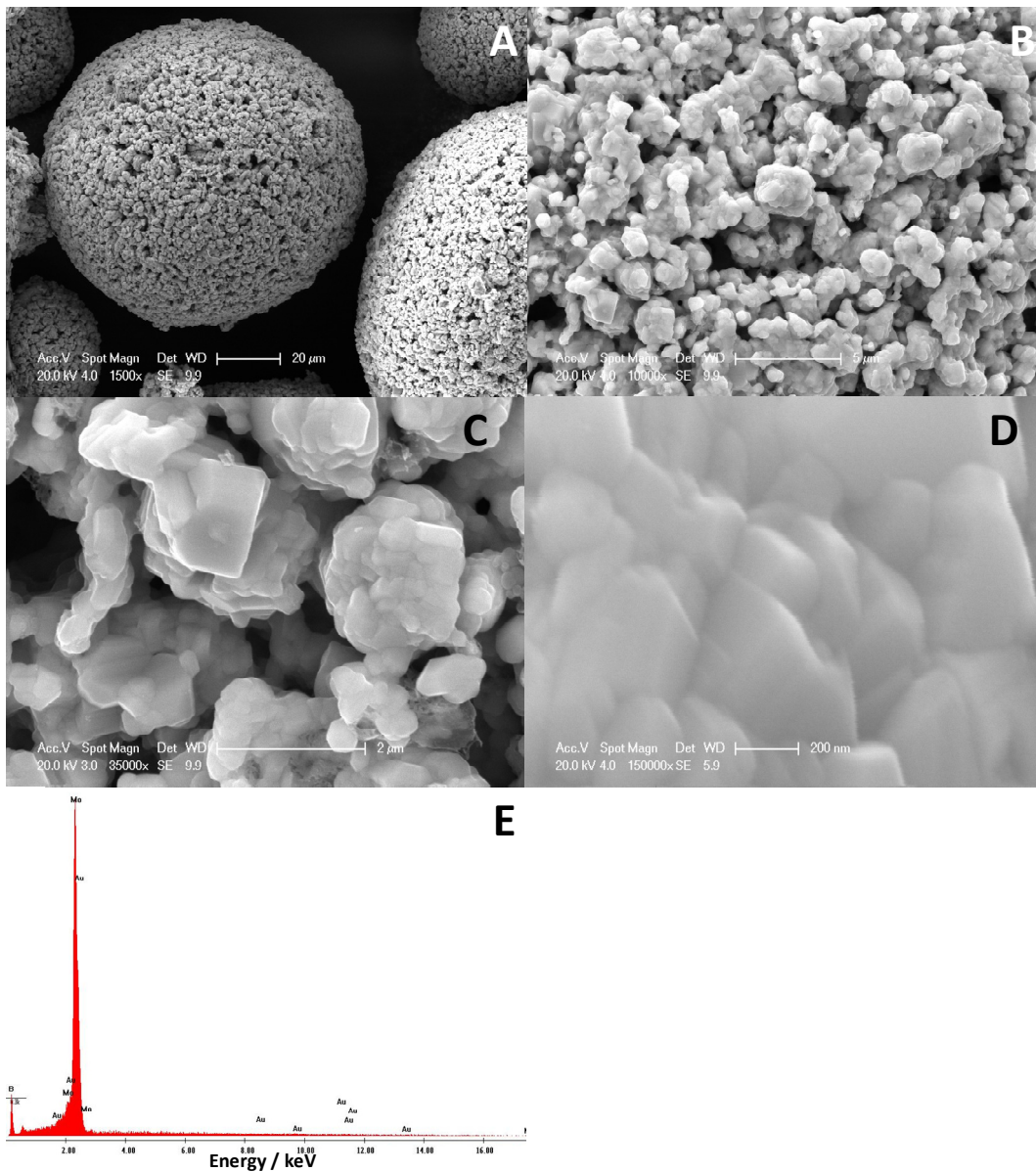


Figure 54: SEM images of  $\alpha$ -MoB with a magnification of (A) 1500, (B) 10000, (C) 35000, (D) 150000 and (E) EDX analysis.

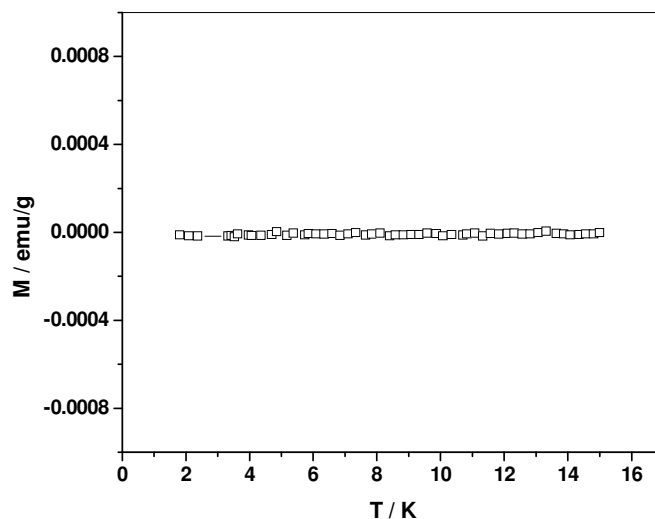


Figure 55: Superconductivity measurement (ZFC) for  $\alpha$ -MoB.

A measurement of superconductivity was performed for the tetragonal modification of MoB in the zero-field cooled mode between 1.8 K and 15 K. No transition was observed down to 1.8 K (Figure 55). This finding is well fitting with earlier reports which described that the tetragonal modification of MoB does not become superconducting <sup>[58]</sup>.

#### 4.5.6. Synthesis, structural characterization and superconductivity measurement of $\text{Mo}_2\text{B}_4$

Although there is a difference in the thermal stabilities of  $\text{MoB}_2$  and  $\text{Mo}_2\text{B}_4$ , the key point concerning the synthesis of  $\text{Mo}_2\text{B}_4$  is the composition of the sample. Synthesis of  $\text{Mo}_2\text{B}_4$  both in an electric arc and in quartz ampoules at 1050 °C for three days resulted in well crystalline, monophasic samples. Using the reaction in the quartz ampoules, the ratio of boron to molybdenum in the starting material was varied between 1.9:1 and 4.0:1 to optimize the conditions. In the samples with ratios lower than 2.1:1, traces of molybdenum monoboride were observed, but in the range B:Mo between 2.1 and 4.0 no additional reflections were observed. All of the reflections belonged to  $\text{Mo}_2\text{B}_4$ , as shown in Figure 56.

The refinements of the unit cell parameters of Mo<sub>2</sub>B<sub>4</sub> from the XRD data was done by using the Rietveld method based on the structure model for Mo<sub>2</sub>B<sub>4</sub> from literature <sup>[31]</sup> (Figure 56). The information from literature was confirmed. Unit cell parameters and residuals of the refinement are given in Table 16.

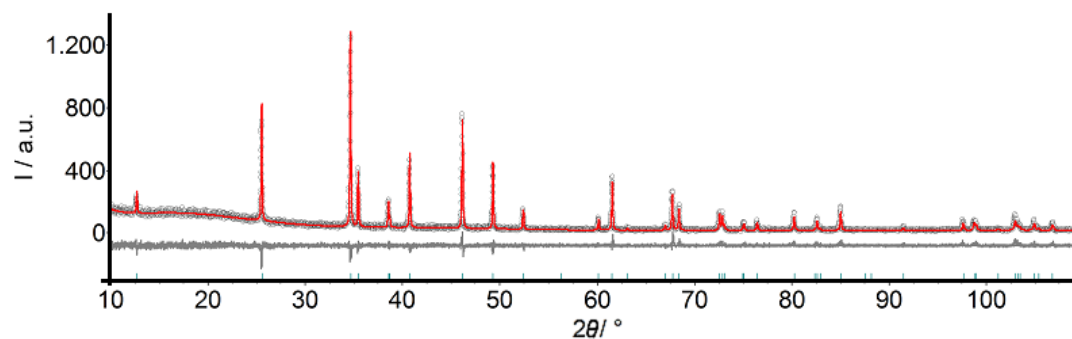


Figure 56: X-ray diffraction pattern of Mo<sub>2</sub>B<sub>4</sub> fitted using the Rietveld method. The black circles are the observed data, the red line is the calculated curve, and the gray curve is the difference curve between the observed and the calculated curves. The tickmarks at the bottom are representing the positions of the reflections for Mo<sub>2</sub>B<sub>4</sub>.

Table 16: Unit cell parameters and residuals of the refinement of Mo<sub>2</sub>B<sub>4</sub>. Literature <sup>[31]</sup> values are given in brackets.

Phase	Mo <sub>2</sub> B <sub>4</sub>
Diffractometer	STOE Stadi-P-Diffractometer
Wavelength / Å	1.54056
Temperature / K	293
Max. 2θ / °	110
R <sub>exp</sub>	13.93
R <sub>wp</sub>	14.23
R <sub>p</sub>	10.68
GOF	1.02
Crystal system	rhombohedral
Space group	<i>R</i> -3 <i>m</i> (166)
<i>a</i> / Å	3.0111(1) – [3.01375(2)]
<i>c</i> / Å	20.935(1) – [20.9541(3)]
<i>V</i> / Å <sup>3</sup>	164.38(1) – [164.82]
Calc. density / g cm <sup>-1</sup>	7.1256(3)
Sample code	MC005

---

Morphological properties of  $\text{Mo}_2\text{B}_4$  were analyzed with SEM for the samples obtained in sealed quartz ampoules and by arc melting to see if there was a difference between the final products. The sample obtained in quartz ampoules showed big particles around 50 to 100 micrometers which are composed of agglomerated particles with a size in the range of 100 nm to 1 micrometer (Figure 57, A, B and C). The sample which was obtained by arc melting consisted of particles that were big and compact with sharp edges (Figure 57, E and F). EDX analysis of the sample obtained from quartz ampoules showed signals for silicon and oxygen which might result from the opening of the quartz ampoule. Other than silicon and oxygen, it was possible to see only tantalum and boron signals. (Figure 57 D).

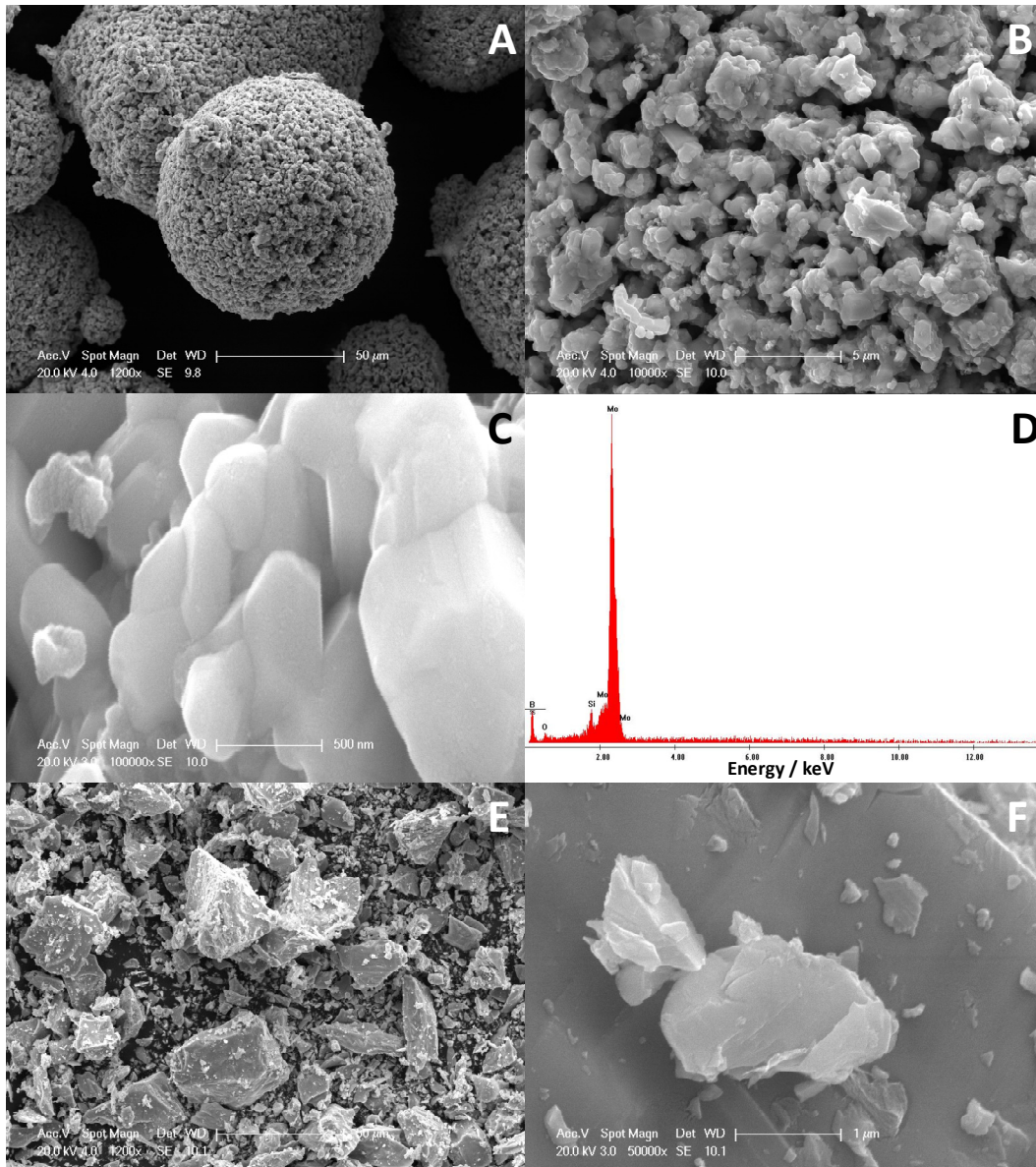


Figure 57: SEM images of  $\text{Mo}_2\text{B}_4$  obtained in quartz ampoule with a magnification of (A) 1200, (B) 10000, (C) 100000, and (D) EDX analysis and  $\text{Mo}_2\text{B}_4$  obtained in electric arc with a magnification of (E) 1200 and (F) 50000.

In the measurement of the superconductivity, no transition was observed down to 1.8 K (Figure 58). This finding is in accordance with the reports <sup>[56, 61]</sup> which mentioned that  $\text{Mo}_2\text{B}_4$  – previously called  $\text{Mo}_2\text{B}_5$  - is not superconducting.

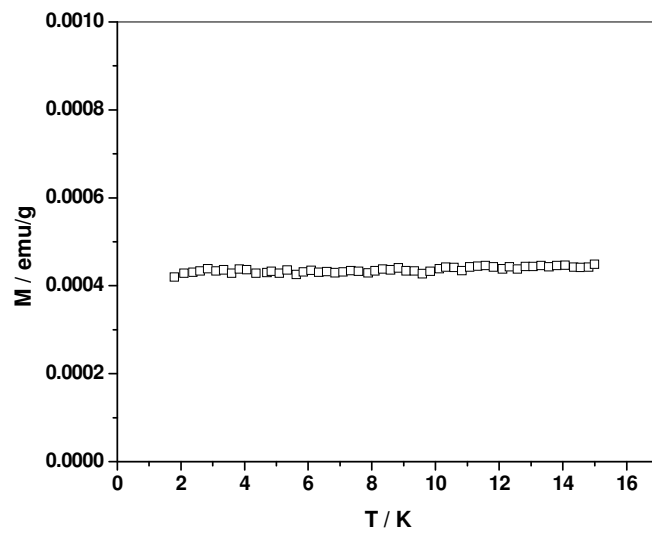


Figure 58: Superconductivity measurement (ZFC) for  $\text{Mo}_2\text{B}_4$ .

#### 4.5.7. Synthesis, structural characterization and superconductivity measurements of MoB<sub>2</sub>

MoB<sub>2</sub> is the high temperature phase of Mo<sub>2</sub>B<sub>4</sub>. The phase diagram shows a stability range between 1517 and 2375 °C. Samples were produced by arc melting, and the boron to molybdenum ratio was varied from 1.8:1 to 2.0:1. For the compositional ratio of 1.8:1, traces of the orthorhombic form of molybdenum monoboride were observed. For ratios like 1.9:1 or 2.0:1, Mo<sub>2</sub>B<sub>4</sub> was formed as the side phase (about 10 %) in addition to well-crystalline MoB<sub>2</sub> (Figure 59).

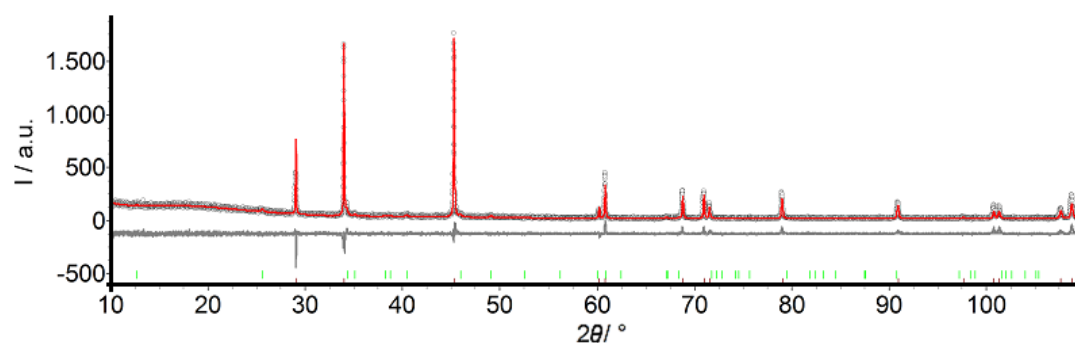


Figure 59: X-ray diffraction pattern of MoB<sub>2</sub> fitted using the Rietveld method. The black circles are the observed data, the red line is the calculated curve, and the gray curve is the difference curve between the observed and the calculated curves. The tickmarks with different colors at the bottom are representing the positions of the reflections for each phase. (brown = MoB<sub>2</sub>, green = Mo<sub>2</sub>B<sub>4</sub>)

The refinement of the unit cell parameters from the XRD data was done by using the Rietveld method based on the structure model from literature<sup>[62]</sup>. The information from literature was confirmed. Unit cell parameters and residuals of the refinement are given in Table 17.

Table 17: Unit cell parameters and residuals of the refinement of MoB<sub>2</sub>. Literature <sup>[44]</sup> values are given in brackets.

Phase	MoB <sub>2</sub>
Diffractometer	STOE Stadi-P-Diffractometer
Wavelength / Å	1.54056
Temperature / K	293
Max. 2θ / °	110
R <sub>exp</sub>	13.62
R <sub>wp</sub>	15.80
R <sub>p</sub>	11.45
GOF	1.16
Crystal system	hexagonal
Space group	<i>P6/mmm</i> (191)
<i>a</i> / Å	3.0425(1) – [3.039]
<i>c</i> / Å	3.0706(1) – [3.055]
<i>V</i> / Å <sup>3</sup>	24.616(1) – [24.43]
Calc. density / g cm <sup>-1</sup>	7.9307(3)
Sample code	MC022

Morphological analysis of the MoB<sub>2</sub> sample showed big particles with sharp edges. There was no agglomeration in the sample and the particles appeared to be compact. EDX analysis showed signals for molybdenum and boron and for oxygen as impurity (Figure 60).

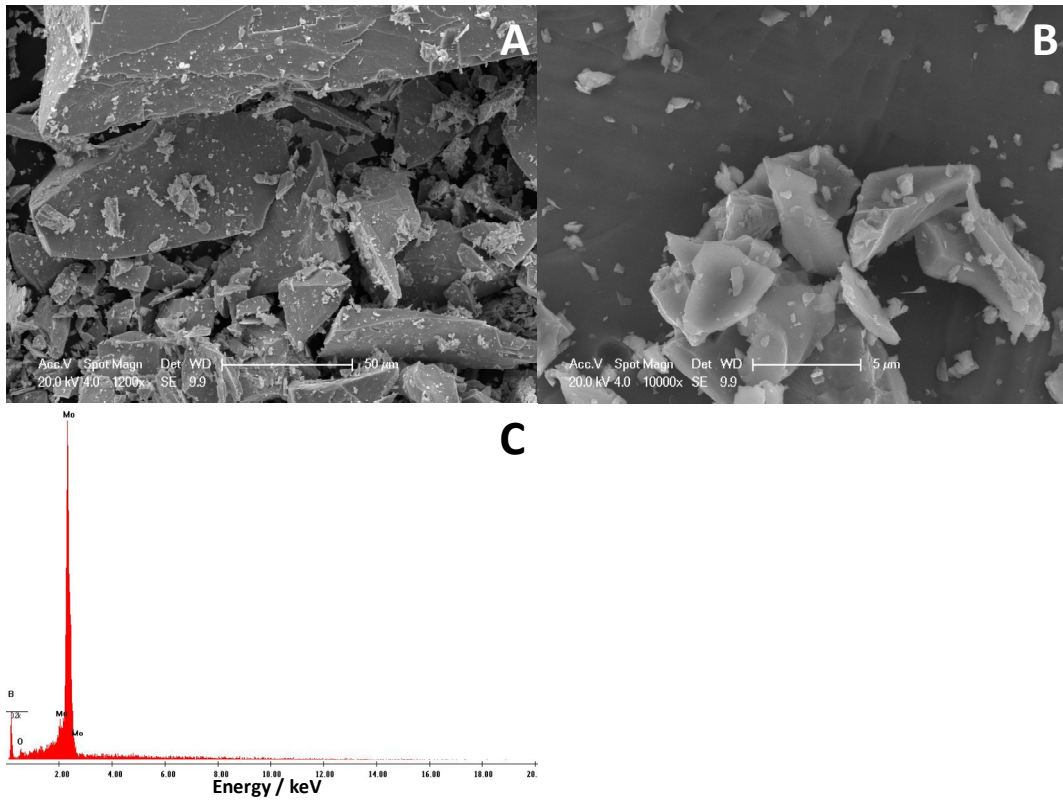


Figure 60: SEM images of MoB<sub>2</sub> with a magnification of (A) 1200, (B) 10000 and (C) EDX analysis.

Molybdenum diboride did not show any superconducting transition down to 1.8 K during a zero-field cooled measurement (Figure 61), similar to what Cooper<sup>[39, 61]</sup> reported for AlB<sub>2</sub>-type MoB<sub>2</sub> that contained less boron than the sample described here.

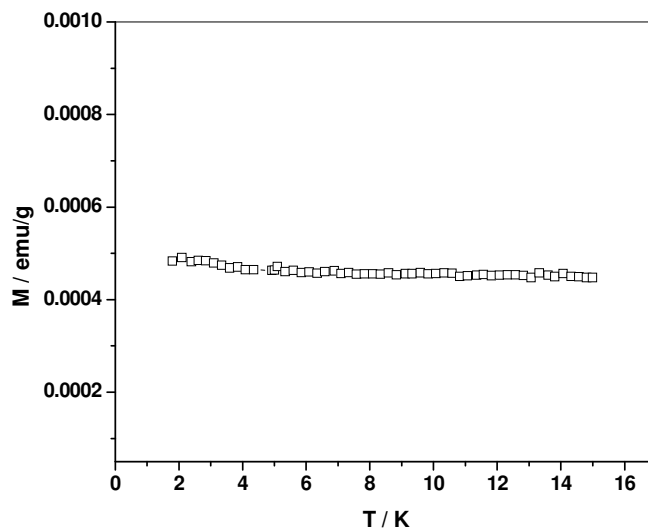


Figure 61: Superconductivity measurement (ZFC) for MoB<sub>2</sub>.

#### 4.5.8. Concluding remarks on Mo-B system

In the binary molybdenum – boron system Mo<sub>2</sub>B,  $\alpha$ -MoB,  $\beta$ -MoB, Mo<sub>2</sub>B<sub>4</sub> and MoB<sub>2</sub> were successfully synthesized. Mo<sub>2</sub>B and MoB<sub>2</sub> containing samples showed traces of side phases like  $\alpha$ -MoB or Mo<sub>2</sub>B<sub>4</sub>.

The samples obtained in arc melting for each phase showed big and compact particles which have sharp edges. There were clear differences in the morphologies of the samples produced in electric arc furnace and in sealed quartz ampoule. EDX analysis disproved the existence of any impurities in the sample, except for traces of oxygen.

The superconductivity measurements proved a transition at  $T_c = 5.85$  K for Mo<sub>2</sub>B which is in accordance with the literature data.  $\beta$ -MoB showed superconductivity with  $T_c = 2.4$  K, but the tetragonal modification of MoB did not show any superconductivity. Neither Mo<sub>2</sub>B<sub>4</sub> nor MoB<sub>2</sub> showed any superconductivity down to 1.8 K.

## 4.6. Tungsten-boron system

### 4.6.1. Phase diagram of the W-B system

The phase diagram of tungsten and boron (Figure 62) contains seven different phases including elemental tungsten and boron.

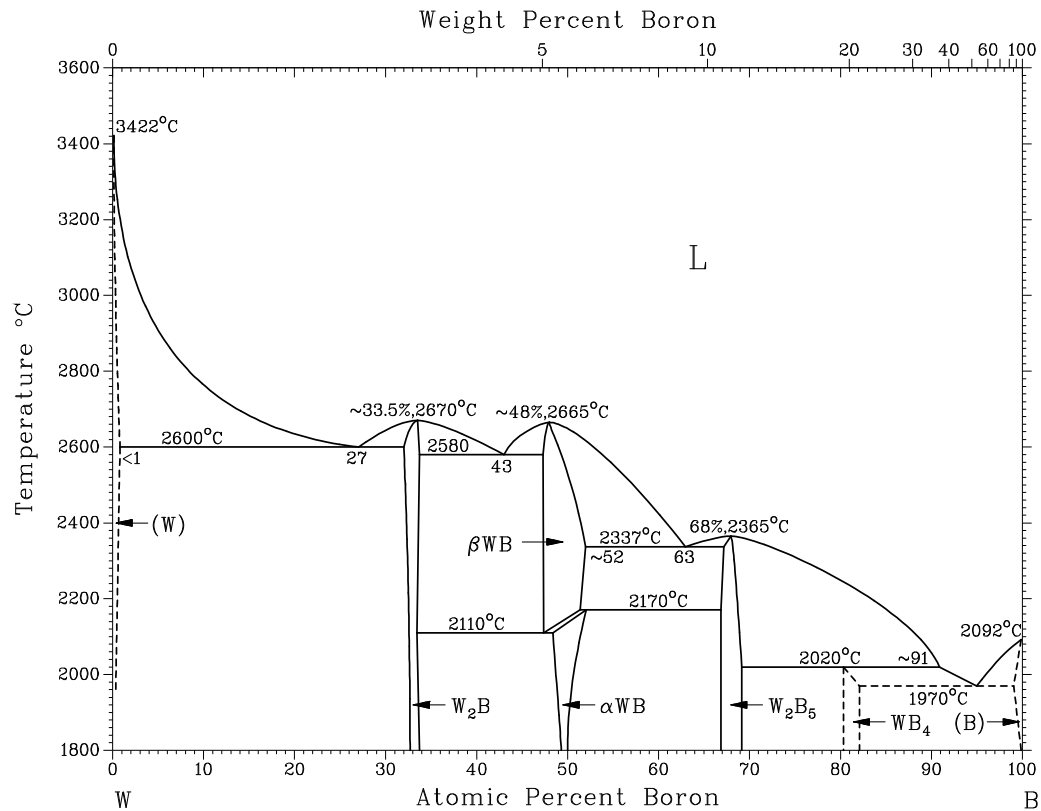


Figure 62: Binary phase diagram of the tungsten - boron system <sup>[32]</sup>.

The binary phases shown in the phase diagram are listed in Table 18. The binary system of tungsten and boron contains similar phases as the system of molybdenum and boron, for example  $W_2B$  and two different modifications of tungsten monoboride. But there is no  $M_3B_2$ . The compositional difference between the orthorhombic and the tetragonal modifications of monoboride is not big.  $\beta WB$  is the high-temperature variant.

Table 18: Binary phases known in the tungsten - boron system.

Phase	Composition at. % B	Space Group	Structure type
$W_2B$	33 to 34	$I4 / mcm$	$Al_2Cu$
$\alpha$ WB	47.5 to 51.5	$I4_1 / amd$	MoB
$\beta$ WB	48 to 52	$Cmcm$	CrB
$W_2B_4^*$	67.5 to 70.5	$P6_3 / mmc$	$WB_2$
$WB_4$	80 to 82.5	$P6_3 / mmc$	-

\*  $W_2B_4$  was known as  $W_2B_5$  previously <sup>[31]</sup>.

Although they are not mentioned in the phase diagram, there exist two other phases in the system with a metal to boron ratio of one to two. These two phases are reported to crystallize in the hexagonal  $AlB_2$ -type structure with space group  $P6/mmm$  <sup>[63]</sup> and in a rhombohedral structure with space group  $R\bar{3}m$  isotopic to  $Mo_2B_4$ . <sup>[64]</sup>

#### 4.6.2. Literature review

There are two different modifications of the monoboride of tungsten reported in literature. The first phase was described as  $\alpha$ -WB which is the low-temperature form by Kiessling in 1947 with a tetragonal crystal structure with space group  $I4_1/amd$  <sup>[56]</sup>. Crystal structure analysis was done from single crystal X-ray diffraction data. The high-temperature form  $\beta$ -WB was synthesized and the crystal structure was described for the first time in 1952 by Post and Glaser in the orthorhombic crystal system with space group  $Cmcm$  <sup>[65]</sup>. Crystal structure analysis was performed based on X-ray powder diffraction data. Both of the tetragonal and orthorhombic modifications of WB were reported in literature to be non-superconducting down to 1.8 K <sup>[36, 59]</sup>.

Similar to  $Mo_2B_4$ ,  $W_2B_4$  was known as  $W_2B_5$ .  $W_2B_4$  was firstly synthesized and characterized by Kiessling in 1947. Its crystal structure is of hexagonal symmetry (space group  $P6_3/mmc$ ) <sup>[56]</sup>. Structural information was obtained from single crystal X-ray diffraction data. Studies of Frotscher indicated that one boron atom site reported in literature is not occupied, thus changing the formula from  $W_2B_5$  to  $W_2B_4$ . Due to broad reflections in the diffraction pattern of Frotscher, the question could not be solved unambiguously <sup>[66]</sup>. The phase was reported by Hardy and Hulm to be non-superconducting down to 1.8 K <sup>[49]</sup>.

### 4.6.3. Synthesis, structural characterization and superconductivity measurements of $\beta$ -WB

The synthesis of the high-temperature modification of tungsten monoboride ( $\beta$ -WB) was possible by arc melting. An excess of boron of 10 % was used. The key point for obtaining the  $\beta$ -WB modification was controlling the cooling rate after heating the mixture. Immediately after the mixture formed a melt and a ball shape, the power of the arc was shut down and then argon was released into the chamber. At the end of the quick cooling process the sample was phase-pure and well-crystalline as can be seen in Figure 63.

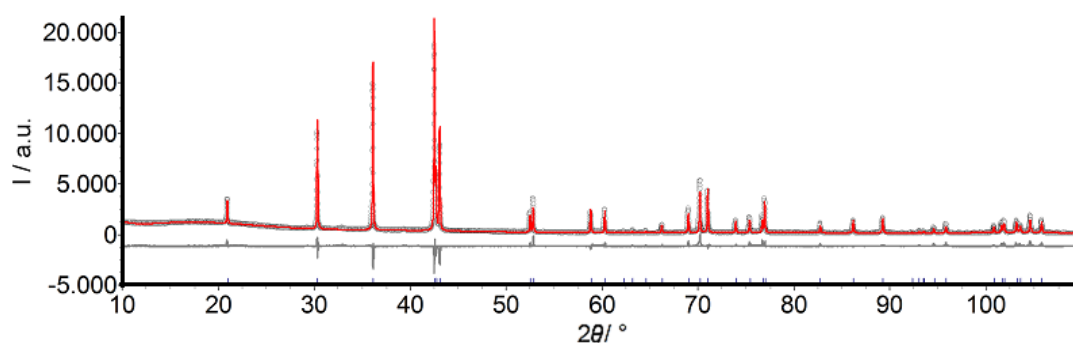


Figure 63: X-ray diffraction pattern of  $\beta$ -WB fitted using the Rietveld method. The black circles are the observed data, the red line is the calculated curve, and the gray curve is the difference curve between the observed and the calculated curves. The tickmarks at the bottom are representing the positions of the reflections for the  $\beta$ -WB.

The refinement of the unit cell parameters from the XRD data were done by using the Rietveld method based on the structure model in literature <sup>[65]</sup>. The information from literature was confirmed. Unit cell parameters and residuals of the refinement are given in Table 19.

Table 19:. Unit cell parameters and residuals of the refinement of the orthorhombic modification of WB. Literature <sup>[67]</sup> values are given in brackets.

Phase	WB
Diffractometer	STOE Stadi-P-Diffractometer
Wavelength / Å	1.54056
Temperature / K	293
Max. $2\theta$ / °	110
$R_{\text{exp}}$	4.20
$R_{\text{wp}}$	10.32
$R_{\text{p}}$	7.29
GOF	2.46
Crystal system	orthorhombic
Space group	<i>Cmcm</i> (63)
$a$ / Å	3.1353(1) - [3.19]
$b$ / Å	8.4542(1) - [8.40]
$c$ / Å	3.0659(1) - [3.07]
$V$ / Å <sup>3</sup>	81.265(2) - [82.26]
Calc. density / g cm <sup>-1</sup>	15.911(1)
Sample code	MK167

Morphological analysis of the  $\beta$ -WB sample showed big particles with sharp edges. There was no agglomeration in the sample and the particles looked compact. Since the sample was sputtered with gold in order to prevent charging of the sample, it was possible to see the signals of gold and oxygen as impurity in addition to the signals of tungsten and boron in EDX (Figure 64).

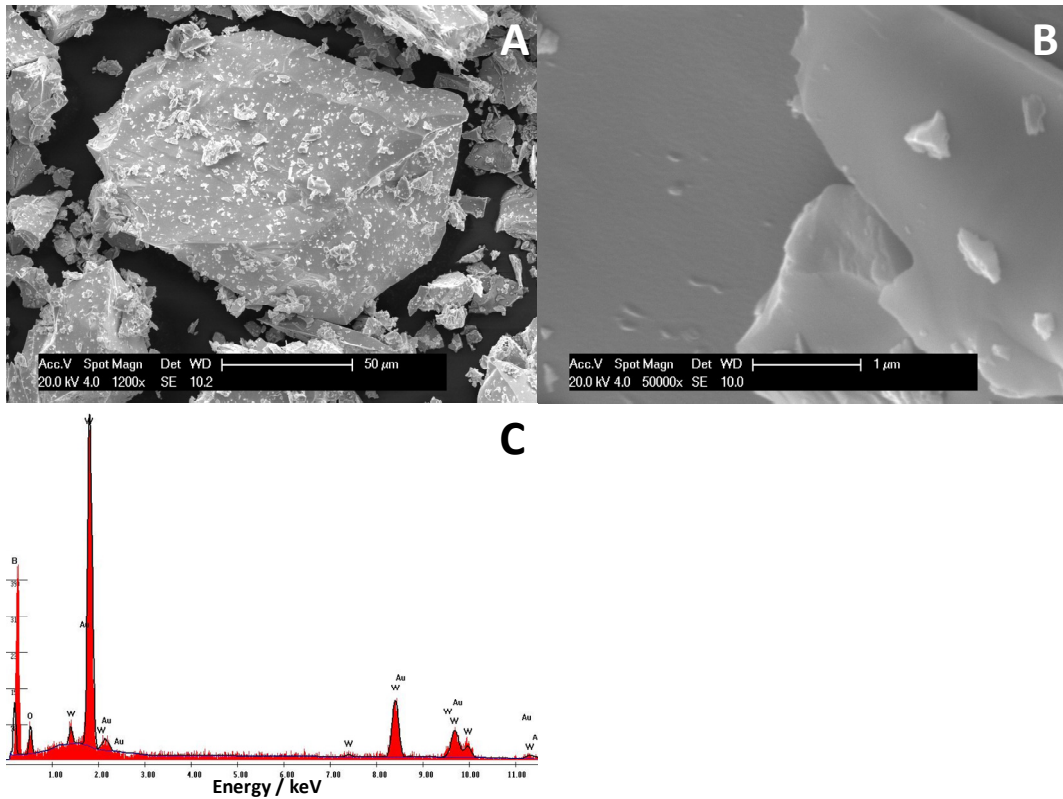


Figure 64: SEM images of  $\beta$ -WB with a magnification of (A) 1200, (B) 50000 and (C) EDX analysis.

A zero-field cooled measurement was done between 1.8 K and 15 K for  $\beta$ -WB. The superconductivity measurement showed a clear and sharp transition into a superconducting phase with an onset temperature of 2.0 K. Since the sample was not containing any other detectable phases or impurities, the sharp transition starting at 2.0 K indicates an unknown superconductivity of the  $\beta$ -WB (Figure 65). This is the first observation of superconductivity for  $\beta$ -WB.

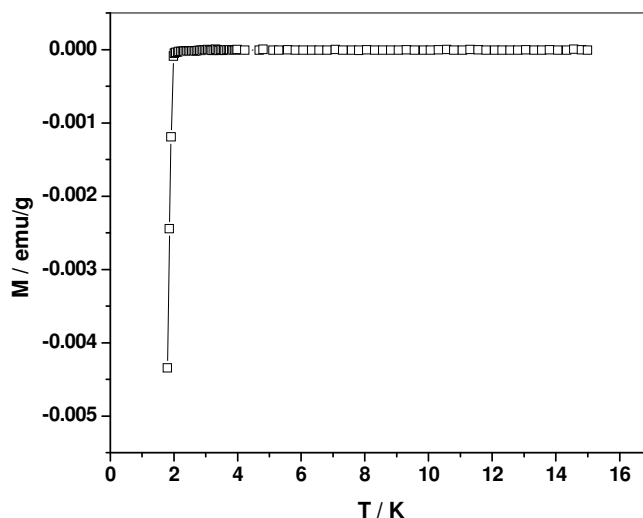


Figure 65: Superconductivity measurement (ZFC) for  $\beta$ -WB.

#### 4.6.4. Synthesis, structural characterization and superconductivity measurements of $\alpha$ -WB

The synthesis of the low-temperature modification of tungsten monoboride ( $\alpha$ -WB) was possible either in the electric arc with slow cooling rates or in quartz ampoules. A 10 % excess of boron was used for synthesis in quartz ampoules and a 15 to 20 % excess of boron for arc melting. As described for  $\beta$ -WB,  $\alpha$ -WB was obtained only when the cooling was controlled. Immediately after the mixture was molten, the sample was cooled down slowly by decreasing the power of the arc step by step and keeping the sample under vacuum for a while after the reaction was finished. In quartz ampoules (1050 °C, three days) a product was obtained of which the XRD pattern showed a mono-phasic sample of  $\alpha$ -WB. But the reflections in the pattern exhibited different kinds of peak profiles concerning half widths and intensities (Figure 66). In the sample which was produced by arc melting, the XRD pattern showed a much higher crystallinity for  $\alpha$ -WB. In addition to that highly crystalline  $\alpha$  phase, tiny traces of the high-temperature phase of WB were observable (Figure 67).

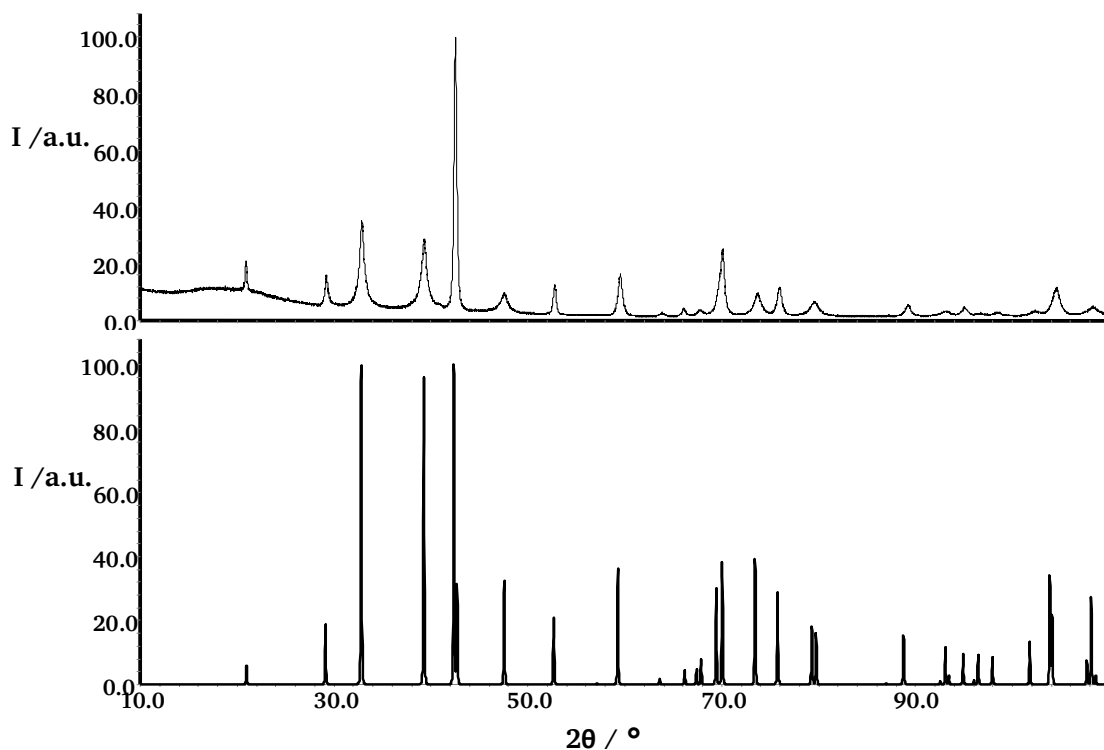


Figure 66: Experimental XRD pattern (top) and the theoretical pattern <sup>[56]</sup> (below) of the tetragonal modification of WB.

The Rietveld refinement on the XRD data of the sample produced in quartz ampoules was not successful because of the poor fit of the peak profiles. The observance of broad and sharper reflections with unexpected intensities can be an indication of stacking faults which are typical for the CrB-structure type. The sample produced by arc melting did not show an XRD pattern with broad reflections.

The refinement of the unit cell parameters from the XRD data was done by using the Rietveld method based on the structure model from literature <sup>[56]</sup>. The information from literature was confirmed. Unit cell parameters and residuals of the refinement are given in Table 20.

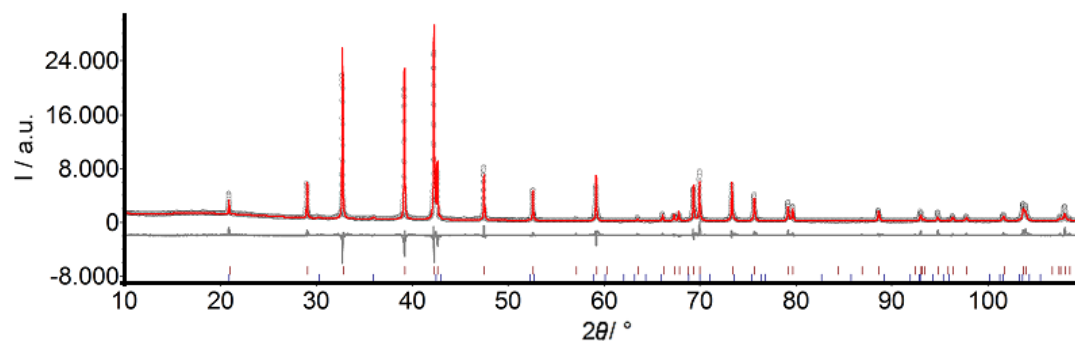


Figure 67: X-ray diffraction pattern of  $\alpha$ -WB fitted using the Rietveld method. The black circles are the observed data, the red line is the calculated curve, and the gray curve is the difference curve between the observed and the calculated curves. The tickmarks with different colors at the bottom are representing the positions of the reflections for each phase. (blue =  $\beta$ -WB, brown =  $\alpha$ -WB)

Table 20.: Unit cell parameters and residuals of the refinement of  $\alpha$ -WB. Literature <sup>[56]</sup> values are given in brackets.

Phase	WB
Diffractometer	STOE Stadi-P-Diffractometer
Wavelength / Å	1.54056
Temperature / K	293
Max. $2\theta$ / °	110
$R_{\text{exp}}$	3.78
$R_{\text{wp}}$	12.36
$R_{\text{p}}$	8.77
GOF	3.27
Crystal system	tetragonal
Space group	$I4_1/amd$ (141)
$a$ / Å	3.1171(1) - [3.115]
$c$ / Å	16.933(1) - [16.930]
$V$ / Å <sup>3</sup>	164.53(1) - [164.28]
Calc. density / g cm <sup>-1</sup>	15.718(1)
Sample code	MK113

Morphological analysis (SEM) of the  $\beta$ -WB sample obtained by arc melting showed big particles with sharp edges in SEM. There was no agglomeration in the sample and the particles looked compact. Since the sample was sputtered with gold in order to prevent charging of the sample, it was possible to see the signals of gold in addition to the signals of tungsten and boron (Figure 68). In EDX it was also possible to see the oxygen signal as impurity in the sample.

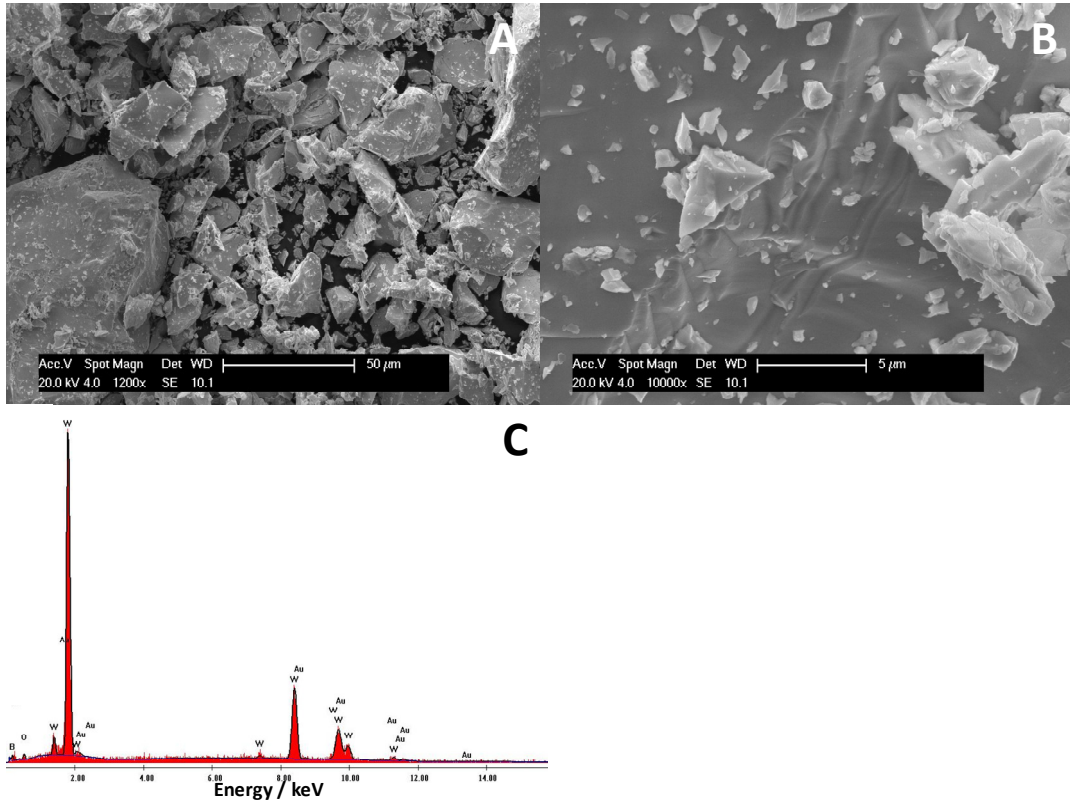


Figure 68: SEM images of  $\alpha$ -WB with a magnification of (A) 1200, (B) 10000 and (C) EDX analysis.

Both samples of  $\alpha$ -WB were analyzed in the SQUID to check whether they become superconducting or not. The different synthesis methods resulted in different particle sizes and unit cell parameters. Both of the samples showed a superconducting transition, but the onset of transition temperatures was different (Figure 69). For the sample synthesized at lower temperatures and in quartz ampoules,  $T_c$  equals 3.5 K, for the arc-melted sample  $T_c$  is 4.3 K (Figure 69). The magnitude of the change of magnetization is higher for the arc melted sample. This can be explained by a lower superconducting volume fraction. A previous report on the superconductivity of  $\alpha$ -WB claimed that this phase does not become superconducting above 1.8 K. Our results were reproduced for many samples. This is the first observation of superconductivity for tetragonal WB.

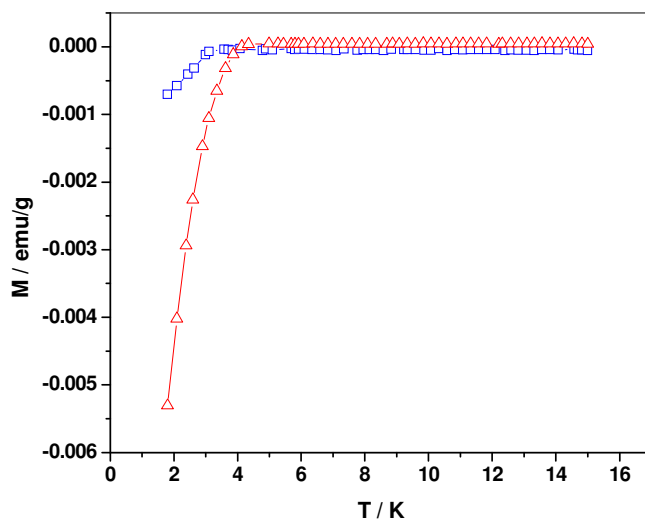


Figure 69: Comparison of superconductivity measurement datas of tetragonal WB produced in quartz ampoule (Blue squares) and in arc melting (red triangle).

#### 4.6.5. Synthesis, structural characterization and superconductivity measurements of $W_2B_4$

For the W:B ratio of 1:2 there were at least three different phases reported in the literature with different crystal structures <sup>[56, 63-64]</sup>. Two of those have very closely related crystal structures as shown in Figure 70. They crystallize in space group  $P6_3/mmc$ ,  $R\bar{3}m$  and  $P6/mmm$ . The first two exhibit planar and corrugated sheets, the latter is of the  $AlB_2$ -type.

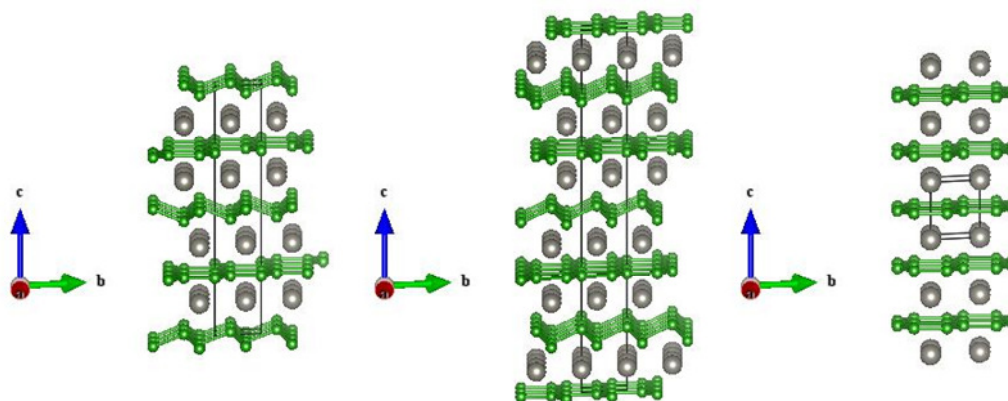


Figure 70: Structures of the three possible modifications of tungsten diboride (left :  $R\bar{3}m$  <sup>[64]</sup>, middle :  $P6_3/mmc$  <sup>[56]</sup>, right :  $P6/mmm$  <sup>[63]</sup>).

---

The difference between the structures that have been described in  $P6_3/mmc$  and  $R\bar{3}m$  is that the hexagonal variant has a larger unit cell with additional boron and metal atom layers.

In our study, only the hexagonal phase was obtained. Both reactions in quartz ampoules and arc melting gave successful results. The composition of the starting mixture was W:B = 1:2 and the sample described here was prepared in quartz ampoules (1050 °C, 3 days). The product was monophasic  $W_2B_4$  according to X-ray powder diffractometry. In the electric arc  $W_2B_4$  was obtained when using an excess of boron of 10 to 20 %.

As in  $Mo_2B_4$ , there was a question mark on the exact composition of  $W_2B_4$ . In literature <sup>[56]</sup> the structure was reported with four different boron atom positions per unit cell. The atom was described to be located in the center of the six-membered chair-like ring of boron atoms in chair conformation as shown in Figure 71.

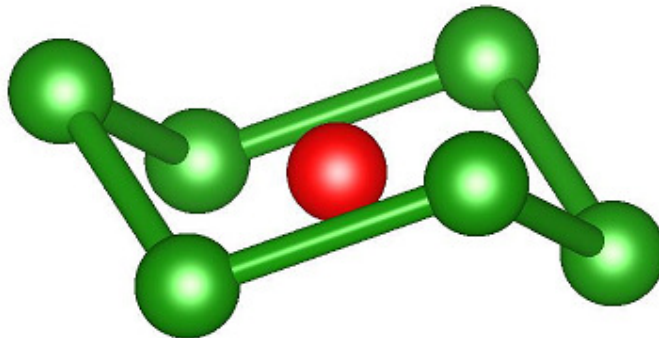


Figure 71: Section of the boron atom arrangement according to the literature <sup>[56]</sup>.

As described in the general part of this thesis, X-rays are diffracted at the periodic electron density distribution of a crystal. Since boron atoms have less electrons than tungsten atoms, the electron density caused by boron atoms in this case is not sufficient to determine the atomic positions of the boron atoms unambiguously. In order to determine the structure completely, neutron diffraction was used now.

For the neutron diffraction measurement, the sample had to be prepared by using isotopically pure  $^{11}\text{B}$  instead of natural boron powder, because of the high neutron absorption of the  $^{10}\text{B}$  isotope. The synthesis of the sample was done in the electric arc. No excess of boron was used. The metal to boron ratio was 1:1.95. The sample showed traces of  $\text{WB}_4$  in addition to  $\text{W}_2\text{B}_4$ .

Using the structure model from literature (space group  $P6_3/mmc$ ) the analysis of the X-ray diffraction data did not indicate any unindexed reflections and the Rietveld refinement of the crystal structure (without the boron atom in the center of the chair-like hexagon resulted) already in a reasonable fit. But in the refinement based on the neutron diffraction data using the same structure model <sup>[56]</sup> several unidentified small reflections were observed. With group-sub-group relationships a new structure model was derived. Transforming the space group and unit cell from  $P6_3/mmc$  into  $P6_3/mcm$  through a what is called “klassengleiche” transition of index 3 led to a new structural description that allows it to explain all of the reflections in the observed neutron diffraction pattern (Figure 72). The new unit cell  $a'$ ,  $b'$  and  $c'$  corresponds to  $2a-b$ ,  $-a+b$ ,  $c$  of the original description.

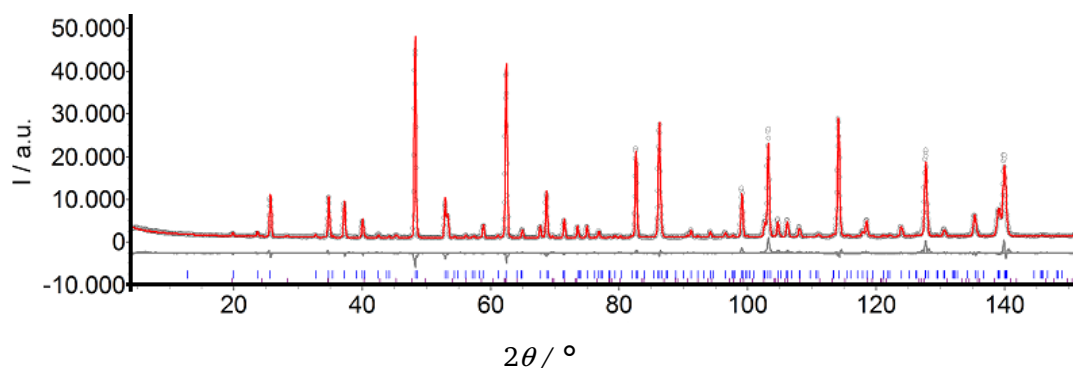


Figure 72: Rietveld refinement of the structure of  $\text{W}_2\text{B}_4$ , based on neutron diffraction data. The black circles are the observed data, the red line is the calculated curve, and the gray curve is the difference curve between the observed and the calculated curves. The tickmarks with different colors at the bottom are representing the positions of the reflections for each phase. (blue =  $\text{W}_3\text{B}_4$ , purple =  $\text{WB}_4$ )

The structure refinement in the new settings showed that – in addition to the missing atom in the center of the chair-like hexagon – the occupancy of one of the boron atom sites in the planar boron atom layer is much lower than in the original model. The final occupancy value for the boron atom labeled B1 is about 0.2 (Figure 73). All of the atomic

distances were investigated and it was seen that the B-B bond lengths are varying between 1.6833(1) Å and 1.8367(2) Å, which is in the acceptable range for B-B bond lengths.

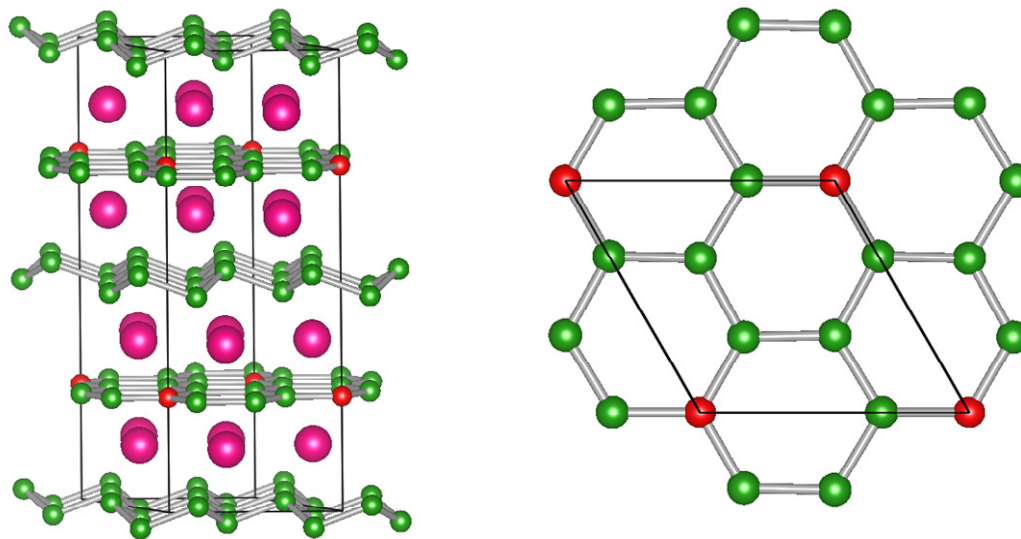


Figure 73: Unit cell of  $W_2B_4$  with the new structure model (left), planar layer in the unit cell with a view along c axis (right). (pink = W, green = boron, red = boron atom labeled as B1)

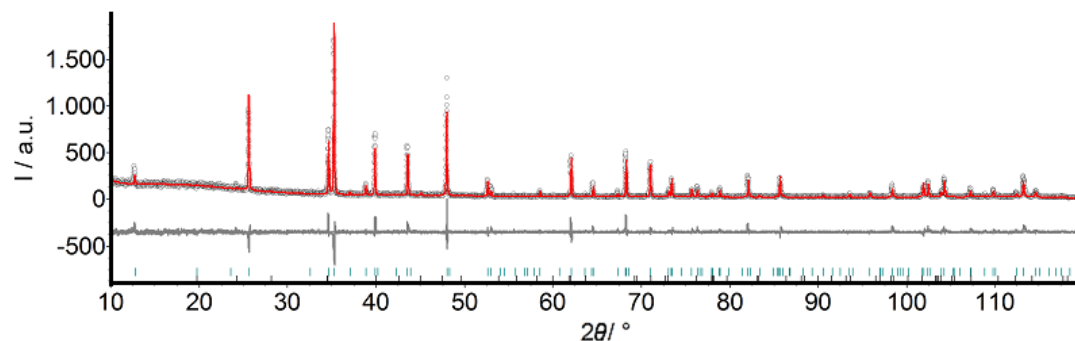


Figure 74: Rietveld refinement of the structure of  $W_2B_4$ , based on X-ray diffraction data. The black circles are the observed data, the red line is the calculated curve, and the gray curve is the difference curve between the observed and the calculated curves. The tickmarks with different colors at the bottom are representing the positions of the reflections for each phase. (blue =  $W_3B_4$ , purple =  $WB_4$ )

The new structure model is only an assumption of the real structure because the intensity of some of the smaller reflections are not fitted well concerning their intensity although their presence is allowed according to crystal symmetry. The X-ray powder diffraction data however fitted with satisfactory results when using the new structure model. Table

21 gives the results of both structure refinements based on neutron and X-ray diffraction. Based on the results from the neutron diffraction experiment the formula of the phase under discussion should be  $W_2B_{4-x}$ .

Table 21: Comparison of the unit cell parameters and the residuals of the refinements for the neutron and X-ray diffraction data sets.

Phase	$W_2B_4$	
Diffractometer	FRM II, SPODI beamline, Ge(551) monochromator, He- 3 counter	STOE Stadi-P-Diffractometer
Radiation source	Neutron	X-ray
Wavelength / Å	1.548160	1.54056
Temperature / K	293	293
Max. $2\theta$ / °	150	120
$R_{exp}$	2.08	12.41
$R_{wp}$	6.97	15.63
$R_p$	5.29	11.80
GOF	3.36	1.26
Crystal system	Hexagonal	
Space group	$P6_3/mcm$ (193)	
$a$ / Å	5.1742(1)	5.1761(1)
$c$ / Å	13.896(1)	13.900 (1)
$V$ / Å <sup>3</sup>	322.19(1)	322.52(1)
Calc. density / g cm <sup>-1</sup>	12.730(1)	12.936(1)
Sample code	MK271	

Table 22: Refined structural parameters obtained from neutron diffraction data of  $W_2B_{4-x}$ .

Atom	Wyck. Site	$x/a$	$y/b$	$z/c$	Occupancy	$B_{eq}$
<b>W1</b>	12k	0.6671(6)	0	0.3634(1)	1	0.21(3)
<b>B1</b>	2a	0	0	1/4	0.166(8)	0.12(4)
<b>B2</b>	4c	1/3	2/3	1/4	1	0.17(3)
<b>B3</b>	12k	0.6663(4)	0	0.5232(1)	1	0.11(2)
<b>B4</b>	6g	0.3253(6)	0	1/4	1	0.06(2)

Additionally, the detailed comparison of the diffraction patterns of samples produced by either solid-solid reaction at 1050 °C or via melts at several thousand °C showed reflections with significant differences in their characteristics. As shown in Figure 75,

reflections are much broader for lower synthesis temperatures, which of course is due to differences in particle sizes and crystallinity. All of the reflections shown in the upper trace belong to  $W_2B_4$ . Some of the smaller reflections (e.g. at approx.  $58$  and  $65^\circ 2\theta$ ) become invisible in the lower trace due to the broadening of the reflections.

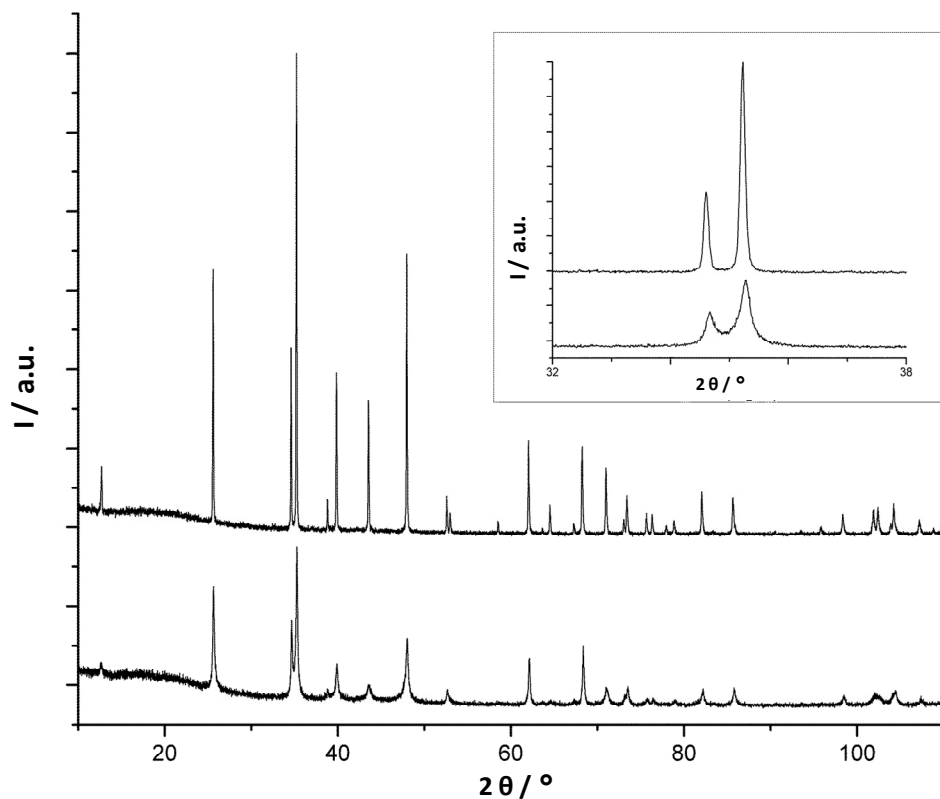


Figure 75: XRD patterns of  $W_2B_4$  synthesized at different temperatures (top: high temperature/electric arc; bottom: low temperature/quartz ampoule). The inset shows selected reflections to visualize the broadening [68].

To confirm morphological differences SEM images for two of the different samples are shown in Figure 76. Arc melting resulted in particles that appear to be more compact, bigger, and exhibiting sharper edges compared to the particles synthesized in quartz ampoules. Those were smaller and highly agglomerated. In SEM, it appears as if the agglomerates consist of grains of approx.  $40 - 100$  nm in diameter.

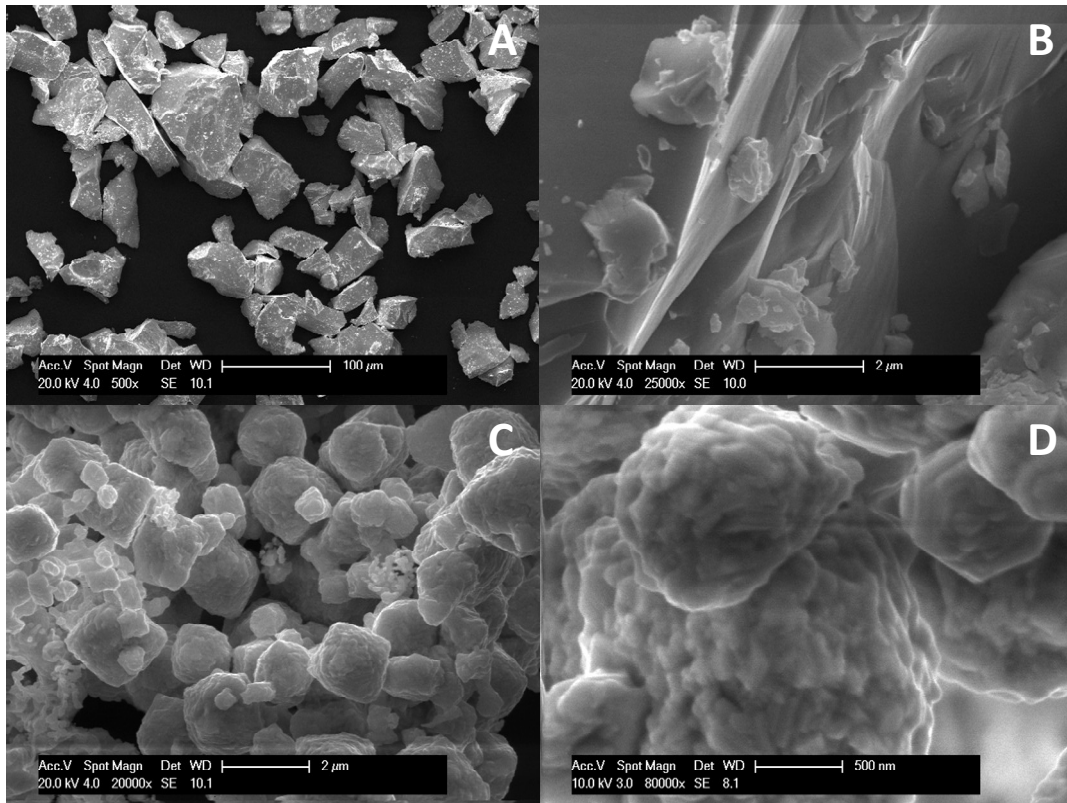


Figure 76 SEM images of  $W_2B_4$  obtained in electric arc with a magnification of (A) 500, (B) 25000 and  $W_2B_4$  obtained in quartz ampoule with a magnification of (C) 20000 and (D) 80000.

The differences in morphology are emphasized here because the superconductivity is observed to be sensitive to the particle size of  $W_2B_4$ . Some of the samples did not show any superconducting transition down to 1.8 K, other samples revealed superconducting behavior below 5.4 K (Figure 77). It was shown repeatedly that the observed effect depends on the morphology of the samples. Small particles did not show superconductivity down to temperatures as low as 2 K.

When the sample size comes into the same order of magnitude as the superconducting coherence length, superconductivity breaks down as described by the Anderson Criterion [69]. In this case, the coupling of electrons which is necessary for superconductivity is suppressed.

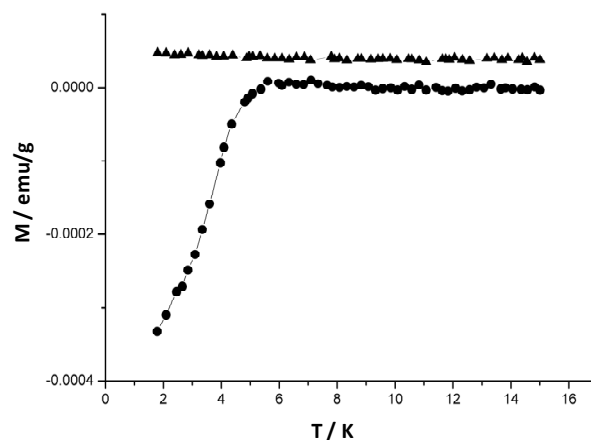


Figure 77: Comparison of superconductivity measurement datas of  $W_2B_4$  produced in quartz ampoule (triangles) and with arc melting (circles).

#### 4.6.6. Concluding remarks on the W-B system

The tungsten-boron system was very similar to the molybdenum-boron system in terms of which phases are found in the system as well as which synthesis conditions are needed to prepare those phases. Orthorhombic WB was synthesized successfully in monophasic form. Tetragonal WB was synthesized in two different variants, depending on the temperatures during the preparation. Those two methods resulted in slightly different unit cell parameters and different particle sizes. Tungsten diboride with  $AlB_2$ -type structure was not observed in any of our studies, but  $W_2B_4$  was successfully synthesized at two different temperatures.  $W_2B_4$  samples exhibit different morphological properties depending on the synthesis method.

A complete structural investigation was done for  $W_2B_4$  by using neutron diffraction data. The crystal structure of  $W_2B_4$  was described in space group  $P6_3/mcm$  with a unit cell volume larger than originally thought. A deficiency at a special boron atom position in the planar boron layer was observed.

Superconducting phase of orthorhombic WB was observed for the first time ( $T_C = 2.0$  K). In addition to that, tetragonal WB was found to show superconductivity below 3.5 K or 4.3 K, depending on the particle size of the samples. The same effect was observed for  $W_2B_4$ . Large particles of  $W_2B_4$  showed superconductivity below a  $T_C$  of 5.4 K. Small

---

particles did not show any superconductivity which was explained by the Anderson criterion.

## 4.7. Rhenium-boron system

### 4.7.1. The phase diagram of the Re-B system

The phase diagram of rhenium and boron (Figure 78) shows five different phases including elemental rhenium and boron.

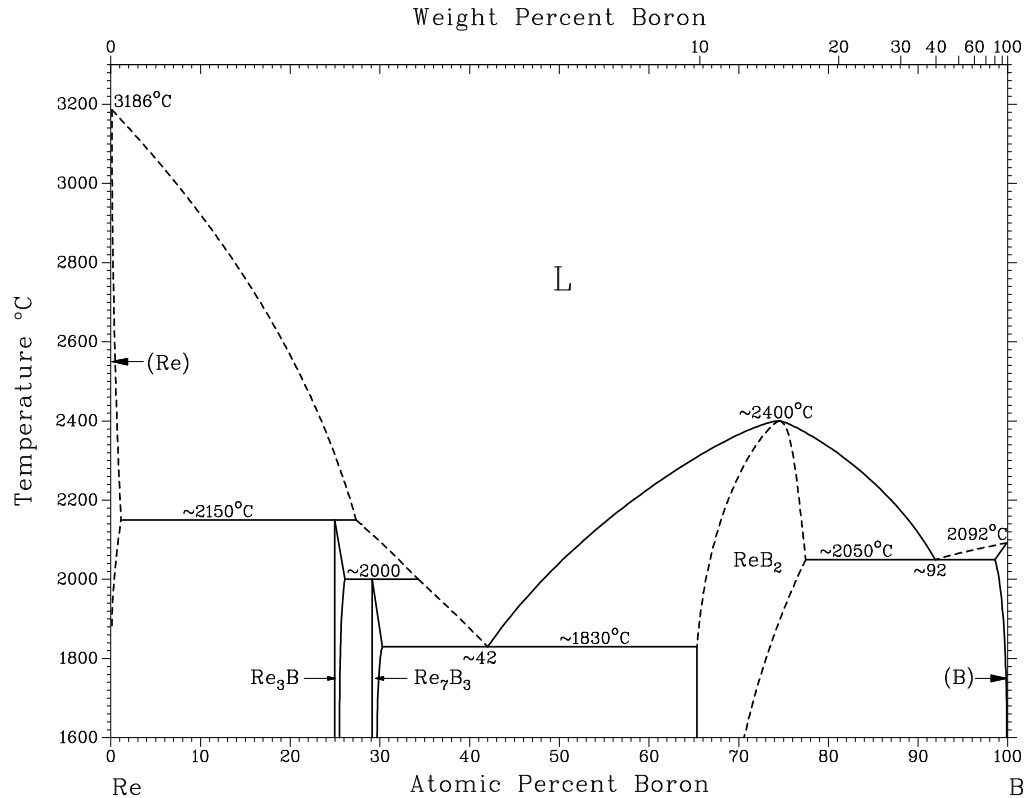


Figure 78: Binary phase diagram of the rhenium - boron system <sup>[32]</sup>.

The binary phases shown in the phase diagram are listed in Table 23. This system is completely different compared to the other metal boron systems included in this study.  $Re_3B$  is the most metal-rich phase. Differently from other systems, there is no  $M_2B$  phase, although there are some theoretical studies on the presence of  $Re_2B$  <sup>[70]</sup>.  $Re_7B_3$  is the phase that has the closest stoichiometry to  $M_2B$ . There is no monoboride of rhenium. The only phase that is common to other transition metal-boron systems is the diboride of rhenium.

Table 23: The binary phases known in the rhenium - boron system.

Phase	Composition at. % B	Space Group	Structure type
Re <sub>3</sub> B	25 to 26	<i>Cmcm</i>	Re <sub>3</sub> B
Re <sub>7</sub> B <sub>3</sub>	29 to 30	<i>P6<sub>3</sub>mc</i>	Th <sub>7</sub> Fe <sub>3</sub>
ReB <sub>2</sub>	65 to 77	<i>P6<sub>3</sub>/mmc</i>	ReB <sub>2</sub>

#### 4.7.2. Literature review

Re<sub>3</sub>B was synthesized and characterized for the first time by Aronsson in 1960<sup>[71]</sup>. The phase was found to crystallize in the orthorhombic crystal system with space group *Cmcm*. Structural characterization based on single crystal X-ray diffraction. Re<sub>3</sub>B was reported to become superconducting below 4.8 K<sup>[72] [73]</sup>.

Re<sub>7</sub>B<sub>3</sub> was described for the first time together with Re<sub>3</sub>B<sup>[71]</sup>. The structure was described with space group *P6<sub>3</sub>mc*. Its superconductivity was reported by Kawano *et al.* ( $T_c = 3.3$  K)<sup>[73]</sup>.

The diboride of rhenium and boron – ReB<sub>2</sub> – was reported by La Placa and Post for the first time in 1962 and described to crystallize in hexagonal symmetry with space group *P6<sub>3</sub>/mmc*. The structural characterization was done using X-ray powder diffraction data. The structure was confirmed by using neutron diffraction data by Frotscher *et al.* in 2010<sup>[74]</sup>. Although Strukova *et al.* and Lue *et al.* reported superconductivity around 4.5 K and 6.3 K<sup>[72, 75]</sup>, some other reports were claiming no superconductivity for ReB<sub>2</sub><sup>[76]</sup>.

#### 4.7.3. Synthesis and structural characterization of Re<sub>3</sub>B

The synthesis of Re<sub>3</sub>B was possible at different temperatures. Since the difference between atomic weights of metal and boron is large in comparison to other transition metals included in this work, was difficult to control experimental errors like weighing errors. The amount of boron that was used in the synthesis of Re<sub>3</sub>B was very low (4.8 mg – 5.1 mg) and this was close to the sensitivity limits of the balance which was used. Despite this, it was possible to conclude that, no excess or an excess up to 10 % of boron was sufficient to get monophasic Re<sub>3</sub>B. The products revealed to be monophasic in three different settings of synthesis. The XRD patterns of the samples produced by arc melting showed higher crystallinity with sharper peaks compared to samples obtained in the high

frequency induction furnace (2000 °C, 2 hours) or in quartz ampoules. In quartz ampoules iodine was added as mineralizer (1050 °C, one day) (Figure 78).

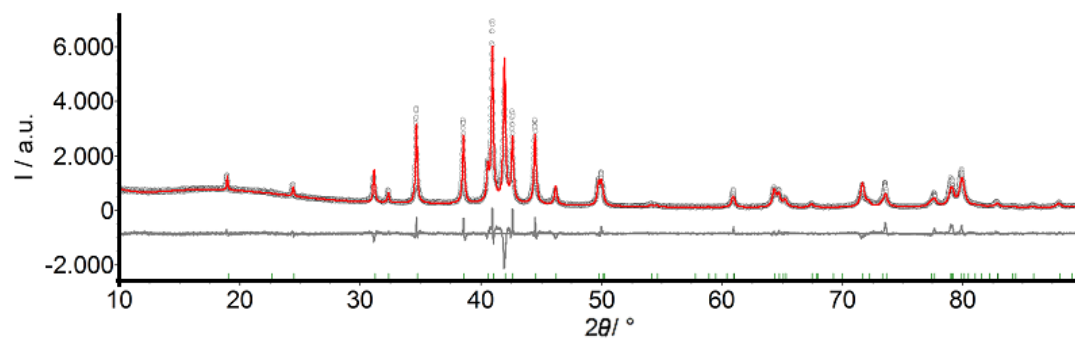


Figure 79: X-ray diffraction pattern of  $\text{Re}_3\text{B}$  fitted using the Rietveld method. The black circles are the observed data, the red line is the calculated curve, and the gray curve is the difference curve between the observed and the calculated curves. The tickmarks at the bottom are representing the positions of the reflections for  $\text{Re}_3\text{B}$ .

The refinement of the unit cell parameters based on XRD data were done by using the Rietveld method and the structure model from literature <sup>[71]</sup>. The information from literature was confirmed. Unit cell parameters and residuals of the refinement are given in Table 24.

Table 24: Unit cell parameters and residuals of the refinement of  $\text{Re}_3\text{B}$ . Literature <sup>[71]</sup> values are given in brackets.

Phase	$\text{Re}_3\text{B}$
Diffractometer	STOE Stadi-P-Diffractometer
Wavelength / Å	1.54056
Temperature / K	293
Max. $2\theta$ / °	90
$R_{\text{exp}}$	4.76
$R_{\text{wp}}$	9.58
$R_{\text{p}}$	6.92
GOF	2.01
Crystal system	orthorhombic
Space group	$Cmcm$ (63)
$a$ / Å	2.8911(1) - [2.890(1)]
$b$ / Å	9.3156(4) - [9.313(5)]
$c$ / Å	7.2618(3) - [7.258(4)]
$V$ / Å <sup>3</sup>	195.56(2) - [195.35]
Calc. density / g cm <sup>-1</sup>	19.339(2)
Sample code	TF015-2

#### 4.7.4. Synthesis, structural characterization and superconductivity measurements of $\text{Re}_7\text{B}_3$

$\text{Re}_7\text{B}_3$  has a slightly smaller thermal stability range than  $\text{Re}_3\text{B}$ . Although the compositional range is not narrower than that of  $\text{Re}_3\text{B}$ ,  $\text{Re}_7\text{B}_3$  is difficult to obtain in monophasic form. In all three synthetic approaches, it was possible to get  $\text{Re}_7\text{B}_3$  with traces of neighbor phases like  $\text{Re}_3\text{B}$  or  $\text{ReB}_2$ . In the induction furnace (1800 °C, two hours) a product was obtained that consisted of  $\text{Re}_7\text{B}_3$  being the major phase in addition to  $\text{Re}_3\text{B}$  and  $\text{ReB}_2$  in small amounts. In the absence of iodine as mineralizer,  $\text{Re}_7\text{B}_3$  did not form at lower temperatures. The product of arc melting was well-crystalline and only traces of  $\text{ReB}_2$  were observable according to the powder XRD pattern (Figure 80).

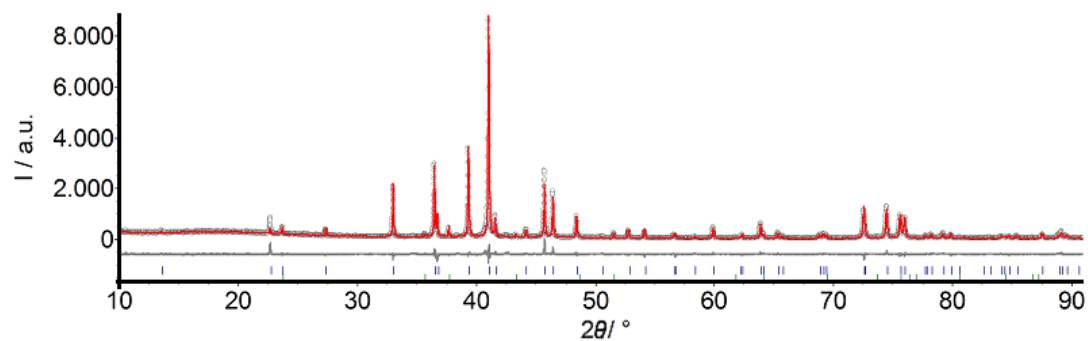


Figure 80: X-ray diffraction pattern of  $\text{Re}_7\text{B}_3$  fitted using the Rietveld method. The black circles are the observed data, the red line is the calculated curve for the structure, and the gray curve is the difference curve between the observed and the calculated curves for the sample. The tickmarks with different colors at the bottom are representing the positions of the reflections for (blue =  $\text{Re}_7\text{B}_3$  and green =  $\text{ReB}_2$ ).

The refinement of the unit cell parameters from the XRD data was done by using the Rietveld method based on the structure model from literature <sup>[71]</sup>. The information from literature was confirmed. Unit cell parameters and residuals of the refinement are given in Table 25.

Table 25: Unit cell parameters and residuals of the refinement of  $\text{Re}_7\text{B}_3$ . Literature <sup>[71]</sup> values are given in brackets.

Phase	$\text{Re}_7\text{B}_3$
Diffractometer	STOE Stadi-P-Diffractometer
Wavelength / Å	1.54056
Temperature / K	293
Max. $2\theta / ^\circ$	90
$R_{\text{exp}}$	7.51
$R_{\text{wp}}$	10.92
$R_{\text{p}}$	7.65
GOF	1.45
Crystal system	hexagonal
Space group	$P6_3mc$ (186)
$a / \text{Å}$	7.5043(1) – [7.504]
$c / \text{Å}$	4.8811(1) – [4.881]
$V / \text{Å}^3$	238.05(1) – [238.0]
Calc. density / $\text{g cm}^{-3}$	18.637(1)
Sample code	TF021

A zero-field cooled measurement was done between 1.8 K and 15 K for  $\text{Re}_7\text{B}_3$ , although the sample contained  $\text{ReB}_2$  as a minor phase. The measurement showed a clear transition to superconducting behavior with an onset temperature of 2.4 K.  $\text{Re}_7\text{B}_3$  becomes superconducting below 2.4 K (Figure 81). In literature the transition temperature for  $\text{Re}_7\text{B}_3$  was reported to be 3.3 K <sup>[73]</sup>. The reason for the lower transition temperature for our sample might be the presence of  $\text{ReB}_2$  in the sample.

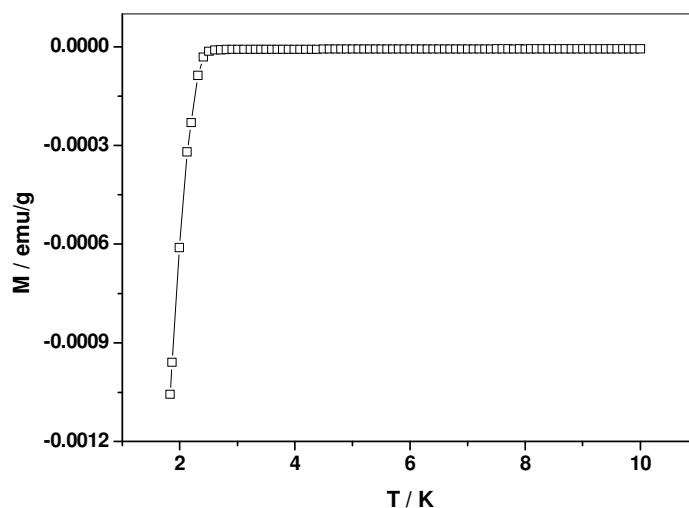


Figure 81: Superconductivity measurement (ZFC) for  $\text{Re}_7\text{B}_3$ .

#### 4.7.5. Synthesis, structural characterization and superconductivity measurements of $\text{ReB}_2$

The synthesis of  $\text{ReB}_2$  was possible in the high frequency induction furnace at 2400 °C. Monophasic  $\text{ReB}_2$  was obtained, but the temperature measurement could not retain its stability because of the evaporation of BN and glassy carbon crucible that covered the surface of the reaction chamber. So, the reaction duration was reduced to 30 minutes. Using arc melting, a 10 % excess of boron was used to get monophasic  $\text{ReB}_2$ . The sample was well-crystalline and did not contain any other phases (Figure 82).

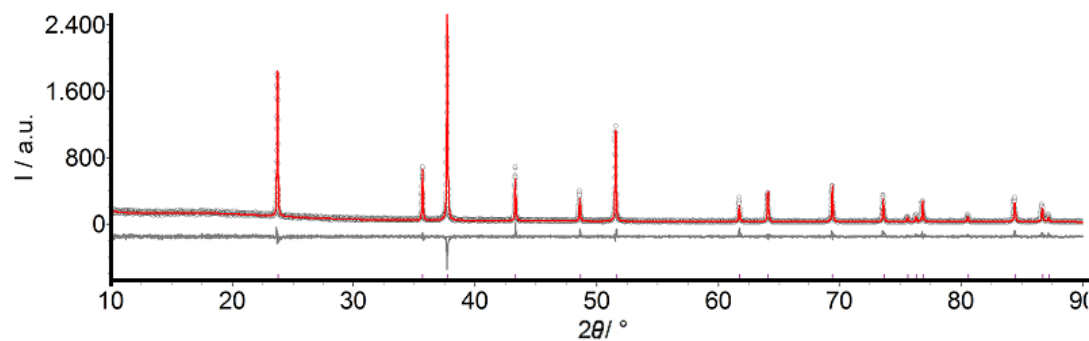


Figure 82: X-ray diffraction pattern of  $\text{ReB}_2$  fitted using the Rietveld method. The black circles are the observed data, the red line is the calculated curve for the structure, and the gray curve is the difference curve between the observed and the calculated curves for the sample. The tickmarks at the bottom are representing the positions of the reflections for  $\text{ReB}_2$ .

The refinement of the unit cell parameters from the XRD data was done by using the Rietveld method based on the structure model in literature <sup>[74]</sup>. The information from literature was confirmed. Unit cell parameters and residuals of the refinement are given in Table 26.

Table 26: Unit cell parameters and residuals of the refinement of  $\text{ReB}_2$ . Literature <sup>[74]</sup> values are given in brackets.

Phase	$\text{ReB}_2$
Diffractometer	STOE Stadi-P-Diffractometer
Wavelength / Å	1.54056
Temperature / K	293
Max. $2\theta / ^\circ$	90
$R_{\text{exp}}$	12.35
$R_{\text{wp}}$	12.97
$R_{\text{p}}$	10.01
GOF	1.05
Crystal system	hexagonal
Space group	$P6_3/mmc$ (194)
$a / \text{Å}$	2.9013(1) – [2.9005(1)]
$c / \text{Å}$	7.4797(2) – [7.4772(1)]
$V / \text{Å}^3$	54.526(2) – [54.47]
Calc. density / $\text{g cm}^{-3}$	12.658(1)
Sample code	MK098

---

ReB<sub>2</sub> was also checked for possible superconductivity with a zero field cooled measurement between 1.8 K and 10 K. In the magnetization versus temperature curve, no transition was observed down to 1.8 K (Figure 83). This finding is in accordance with the reports <sup>[76]</sup> that described ReB<sub>2</sub> being not superconducting.

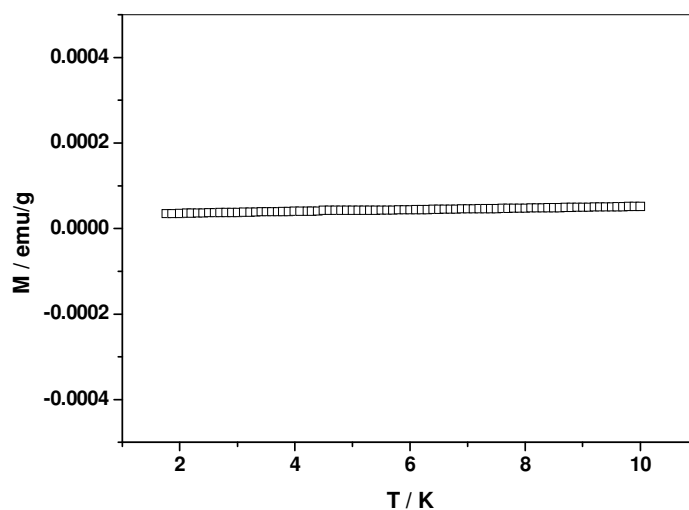


Figure 83: Superconductivity measurements (ZFC) for ReB<sub>2</sub>.

#### 4.7.6. Concluding remarks on the Re-B system

In the rhenium-boron binary system three different binary phases were obtained: Re<sub>3</sub>B, Re<sub>7</sub>B<sub>3</sub> and ReB<sub>2</sub>. All of those three phases were synthesized successfully. Only Re<sub>7</sub>B<sub>3</sub> contained traces of ReB<sub>2</sub> as a side phase.

Superconductivity measurements of Re<sub>7</sub>B<sub>3</sub> and ReB<sub>2</sub> confirmed the literature except for the small difference in T<sub>C</sub> for Re<sub>7</sub>B<sub>3</sub>. For ReB<sub>2</sub>, no transition was observed down to temperatures as low as 1.8 K.

Rhenium borides proved to be more air-sensitive than other transition metal borides investigated in this work.

---

#### 4.8. Correlation between the crystal structures and superconducting properties of diborides

In the light of the previous studies <sup>[42, 54]</sup> on the relationship between crystal structure and superconducting properties of NbB<sub>2</sub>, It appeared to be interesting to analyze if there is a more general correlation between structural and magnetic properties of diborides.

As described above, NbB<sub>2</sub> retains its crystal structure even if it is boron or niobium deficient. Thus NbB<sub>2</sub> shows different T<sub>C</sub> values and different unit cell parameters. It is possible that the unit cell dimensions and the composition correlate with the magnetic properties of NbB<sub>2</sub>.

Several diborides with varying boron content and unit cell parameters, both from literature and this work, were compared concerning their *a/c* ratio (Figure 84). It appeared that superconducting phases (MgB<sub>2</sub>, NbB<sub>2±x</sub>) have a large *c* and *a* values than those that were found to remain non-superconducting (TaB<sub>2±x</sub>, MoB<sub>2</sub>). One of the NbB<sub>2±x</sub> phases however exhibits no superconductivity despite its high *a* value.

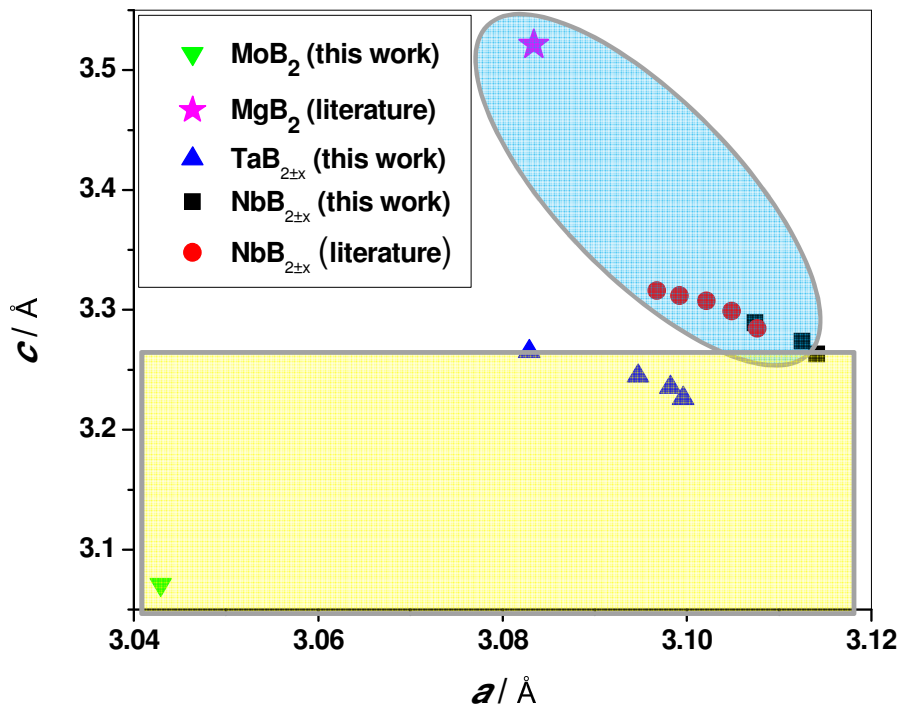


Figure 84: Unit cell parameters;  $c$  and  $a$  values for different diborides. Each symbol represents a sample. The blue area can be described as the superconducting zone and the compounds presented in the yellow rectangle do not show any superconductivity.

Other borides including one of the niobium diborides and all tantalum and molybdenum diborides which have lower  $a$  and  $c$  values compared to the other diborides are not showing any superconductivity down to 1.8 K. The superconducting samples are shown in the blue area and the samples which do not exhibit any superconductivity are appearing in the yellow area in Figure 84.

---

## 5. Summary and outlook

---

This work is a systematic investigation on five binary metal-boride systems of niobium, tantalum, molybdenum, tungsten and rhenium in terms of synthesis, characterization and superconducting properties.

Three different equipments were used in order to prepare samples of transition metal borides via high temperature solid state synthesis. Arc melting was used in order to reach temperatures higher than 3000 °C which is above the melting points of borides. In order to be able to control better the heating process up to 2000 °C and to apply heating and cooling ramps, a high frequency induction furnace was used. Especially for the synthesis of low temperature phases reactions were carried out under inert atmosphere in sealed quartz ampoules by conventional high temperature furnaces at 1050 °C. The aim was the synthesis of bulk materials as monophasic as possible.

The products obtained were characterized in terms of phase analysis and crystal structure analysis by X-ray powder diffraction and neutron diffraction. Crystal structural characterizations were performed by using the Rietveld method. Morphological analyses were done by using scanning electron microscopy. Magnetic measurements were done to obtained samples in order to see if the samples were superconducting at low temperatures down to 1.8 K.

In the niobium-boron system, Nb<sub>3</sub>B<sub>2</sub>, NbB, Nb<sub>5</sub>B<sub>6</sub> and different samples of NbB<sub>2</sub> with varying boron content were synthesized either monophasic or in a mixture. A complete crystal structure analysis for Nb<sub>5</sub>B<sub>6</sub> was done for the first time by using the Rietveld refinement method. Synthesis of monophasic or multi-phase samples was also possible for Ta<sub>2</sub>B, TaB, Ta<sub>3</sub>B<sub>4</sub>, TaB<sub>2+x</sub>, Mo<sub>2</sub>B, α-MoB, β-MoB, Mo<sub>2</sub>B<sub>4</sub>, MoB<sub>2</sub>, Re<sub>3</sub>B, Re<sub>7</sub>B<sub>3</sub>, ReB<sub>2</sub>, α-WB, β-WB, and W<sub>2</sub>B<sub>4</sub>.

The crystal structure of W<sub>2</sub>B<sub>4</sub> which crystallizes in hexagonal symmetry was investigated by using neutron diffraction data. A new structure model was derived for W<sub>2</sub>B<sub>4</sub> which explains better the diffraction pattern. The crystal structure of W<sub>2</sub>B<sub>4</sub> was described in space group *P6<sub>3</sub>/mcm* with an extended unit cell volume and a boron atom deficiency at a special boron position in the planar boron layer.

---

Magnetic measurements in a SQUID magnetometer down to temperatures as low as 1.8 K were performed to several of the products in order to see if the transition metal borides become superconducting at low temperatures, and the results were compared with data from literature. Superconducting properties were found for the following compounds: NbB<sub>2</sub> (T<sub>C</sub> = 3.5 K), β-MoB (T<sub>C</sub> = 2.4 K), β-WB (T<sub>C</sub> = 2.0 K), α-WB (T<sub>C</sub> = 4.3 K), W<sub>2</sub>B<sub>4</sub> (T<sub>C</sub> = 5.4 K), Re<sub>7</sub>B<sub>3</sub> (T<sub>C</sub> = 2.4 K).

A relationship between superconducting properties and the varying unit cell parameters of diborides was discussed. Also it was found that there is an influence of particle sizes on superconductivity for WB which crystallizes in tetragonal crystal system and W<sub>2</sub>B<sub>4</sub>.

---

## 6. References

---

- [1] S. Sen, I. Ozbek, U. Sen and C. Bindal, *Surface and Coatings Technology* **2001**, *135*, 173-177.
- [2] T. Mori and T. Nishimura, *Journal of Solid State Chemistry* **2006**, *179*, 2908-2915.
- [3] T. Mori in *Chapter 238 Higher Borides*, Handbook on the Physics and Chemistry of Rare Earths (Ed. K. A. Gschneidner, J. C. Bunzli, V. K. Pecharsky), Elsevier, **2007**, 105-173.
- [4] H.-y. Yan, Q. Wei, S.-m. Chang and P. Guo, *Transactions of Nonferrous Metals Society of China* **2011**, *21*, 1627-1633.
- [5] B. Albert and H. Hillebrecht, *Angewandte Chemie-International Edition* **2009**, *48*, 8640-8668.
- [6] T. Lundström in *Borides: Solid-State Chemistry*, Encyclopedia of Inorganic and Bioinorganic Chemistry, John Wiley & Sons, Ltd, **2011**.
- [7] R. A. Alfintseva, L. G. Bodrova and A. D. Verkhoturov, *Journal of the Less Common Metals* **1979**, *67*, 443-448.
- [8] W. N. Lipscomb, *Journal of the Less Common Metals* **1981**, *82*, 1-20.
- [9] D. Music and J. M. Schneider, *Scripta Materialia* **2005**, *52*, 29-31.
- [10] I. M. Ndassa, M. Gilleßen and B. P. T. Fokwa, *Solid State Sciences* **2013**, *17*, 14-20.
- [11] J. Nagamatsu, N. Nakagawa, T. Muranaka, Y. Zenitani and J. Akimitsu, *Nature* **2001**, *410*, 63-64.
- [12] B. Cristina and Y. Tsutomu, *Superconductor Science and Technology* **2001**, *14*, R115.
- [13] P. J. T. Joseph and P. P. Singh, *Physica C: Superconductivity* **2003**, *391*, 125-130.
- [14] H. Takagiwa, E. Nishibori, N. Okada, M. Takata, M. Sakata and J. Akimitsu, *Science and Technology of Advanced Materials* **2006**, *7*, 22-25.
- [15] H. Takeya, K. Togano, Y. S. Sung, T. Mochiku and K. Hirata, *Physica C: Superconductivity* **2004**, *408-410*, 144-145.
- [16] M. Panda, PhD thesis, Synthesis and characterization of alkali metal borides and closo-hydroborates, **2006**, Universität Hamburg.
- [17] D. Fofanov, PhD thesis, Synthesis, characterization and physical properties of metal borides, **2006**, Universität Hamburg.
- [18] T. Shishido, Y. Zheng, A. Saito, H. Horiuchi, K. Kudou, S. Okada and T. Fukuda, *Journal of Alloys and Compounds* **1997**, *260*, 88-92.
- [19] J. Ye, T. Shishido, T. Matsumoto and T. Fukuda, *Journal of Alloys and Compounds* **1998**, *275-277*, 76-80.
- [20] M. S. Islam, PhD thesis, Anhydrous phosphates of molybdenum and rhenium synthesis, crystallization, crystal structures, and spectroscopic investigations, **2011**, Rheinischen Friedrich-Wilhelms-Universität Bonn.
- [21] F. Stober, PhD thesis, Synthese, Charakterisierung und Untersuchung thermoelektrischer Eigenschaften ausgewählter Metallboride, **2012**, Technischen Universität Darmstadt.
- [22] N. Nayan, S. V. S. N. Murty, A. K. Jha, B. Pant, S. C. Sharma, K. M. George and G. V. S. Sastry, *Materials Science and Engineering: A* **2013**, *576*, 21-28.
- [23] Z.-G. Fan and C.-y. Li, *Journal of Alloys and Compounds* **2007**, *436*, 178-180.
- [24] Richie Burnett, <http://www.richieburnett.co.uk/indheat.html>, **12.05.2013**.
- [25] International Centre for Diffraction Data, PDF-2 Release 2001 Sets 1-51 plus 70-89, **2001**.
- [26] P. Scherrer, *Göttinger Nachrichten Gesell.* **1918**, *2*, 98.
- [27] A. L. Patterson, *Physical Review* **1939**, *56*, 978-982.
- [28] H. M. Rietveld, *Acta Crystallographica* **1966**, *20*, 508-513.
- [29] H. M. Rietveld, *Journal of Applied Crystallography* **1969**, *2*, 65-71.

- 
- [30] Walther-Meißner-Institute for Low Temperature Research, <http://www.wmi.badw.de/methods/squid.htm>, **16.05.2013**.
- [31] M. Frotscher, W. Klein, J. Bauer, C. M. Fang, J. F. Halet, A. Senyshyn, C. Baehtz and B. Albert, *Zeitschrift Fur Anorganische Und Allgemeine Chemie* **2007**, *633*, 2626-2630.
- [32] T. B. Massalski and ASM International. in *Binary alloy phase diagrams*, ASM International, Materials Park, Ohio, **1990**, 505-506.
- [33] H. Nowotny and A. Wittmann, *Monatshefte für Chemie und verwandte Teile anderer Wissenschaften* **1958**, *89*, 220-224.
- [34] W. Martienssen, H. Warlimont and SpringerLink (Online service) in *Springer Handbook of Condensed Matter and Materials Data*, Berlin, Heidelberg, Springer-Verlag, **2005**, 695-704
- [35] L. H. Andersson and R. Kiessling, *Acta Chemica Scandinavica*, **1950**, *4*, 160-164.
- [36] B. T. Matthias and J. K. Hulm, *Physical Review* **1952**, *87*, 799-806.
- [37] H. Bolmgren and T. Lundström, *Journal of the Less Common Metals* **1990**, *159*, L25-L27.
- [38] J. T. Norton, H. Blumenthal and S. J. Sindeband, *Transactions of the American Institute of Mining, Metallurgical and Petroleum Engineers* **1949**, *185*, 749-751.
- [39] A. S. Cooper, E. Corenzwil, L. D. Longinot, B. T. Matthias and W. H. Zacharia, *Proceedings of the National Academy of Sciences of the United States of America* **1970**, *67*, 313-319.
- [40] L. Leyarovska and E. Leyarovski, *Journal of the Less-Common Metals* **1979**, *67*, 249-255.
- [41] J. E. Schirber, D. L. Overmyer, B. Morosin, E. L. Venturini, R. Baughman, D. Emin, H. Klesnar and T. Aselage, *Physical Review B* **1992**, *45*, 10787-10788.
- [42] H. Takagiwa, E. Nishibori, N. Okada, M. Takata, M. Sakata and J. Akimitsu, *Science and Technology of Advanced Materials* **2006**, *7*, 22.
- [43] C. A. Nunes, D. Kaczorowski, P. Rogl, M. R. Baldissera, P. A. Suzuki, G. C. Coelho, A. Grytsiv, G. André, F. Boureé and S. Okada, *Acta Materialia* **2005**, *53*, 3679-3687.
- [44] E. B. Rudy, F.;Toth, L., *Zeitschrift fuer Metallkunde* **1963**, *54*, 345-353.
- [45] S. Okada, K. Hamano, T. Lundstrom and I. Higashi, *AIP Conference Proceedings* **1991**, *231*, 456-459.
- [46] H. Bolmgren, T. Lundström, L. E. Tergenius, S. Okada and I. Higashi, *Journal of the Less Common Metals* **1990**, *161*, 341-345.
- [47] R. Kiessling, *Acta Chemica Scandinavica* **1949**, *3*, 603-615.
- [48] E. E. Havinga, H. Damsma and P. Hokkeling, *Journal of the Less Common Metals* **1972**, *27*, 169-186.
- [49] G. F. Hardy and J. K. Hulm, *Physical Review* **1954**, *93*, 1004-1016.
- [50] K. I. Portnoi, V. M. Romashov and S. E. Salibekov, *Soviet Powder Metallurgy and Metal Ceramics* **1971**, *10*, 925-927.
- [51] P. P. Singh, *Physical Review B* **2004**, *69*, 094519.
- [52] D. Kaczorowski, A.J. Zaleski, O.J. Zogal and J. Klamut, *arXiv:cond-mat/0103571v2* **2012**.
- [53] V. A. Gasparov, N.S. Sidorov, I.I. Zver'kova and M. P. Kulakov, *arXiv:cond-mat/0104323v1* **2001**.
- [54] M. Mudgel, V. P. S. Awana, H. Kishan, I. Felner, D. G. A. Alvarez and G. L. Bhalla, *Journal of Applied Physics* **2009**, *105*, 07E313-313.
- [55] S. Okada, K. Kudou, I. Higashi and T. Lundström, *Journal of Crystal Growth* **1993**, *128*, 1120-1124.
- [56] R. Kiessling, *Acta Chemica Scandinavica* **1947**, *1*, 893-916.
- [57] S.-H. Cai and C.-W. Liu, *International Journal of Quantum Chemistry* **1997**, *64*, 459-472.

- 
- [58] J. J. Engelhardt, *Physical Review* **1969**, 179, 452-458.
- [59] W. T. Ziegler and R. A. Young, *Physical Review* **1953**, 90, 115-119.
- [60] J. K. Hulm and B. T. Matthias, *Physical Review* **1951**, 82, 273-274.
- [61] L. E. Muzzy, M. Avdeev, G. Lawes, M. K. Haas, H. W. Zandbergen, A. P. Ramirez, J. D. Jorgensen and R. J. Cava, *Physica C-Superconductivity and Its Applications* **2002**, 382, 153-165.
- [62] E. F. Bertaut and P. Blum, *Acta Crystallographica* **1951**, 4, 72.
- [63] H. P. Woods, F. E. Wawner and B. G. Fox, *Science* **1966**, 151, 75.
- [64] Y. B. Kuz'ma, I. Serebryakova and Plakhina A. M, *Russian Journal of Inorganic Chemistry* **1967**, 12, 288-289.
- [65] B. Post and F. W. Glaser, *Journal of Chemical Physics* **1952**, 20, 1050-1051.
- [66] M. Frotscher, PhD thesis, Struktur und Charakterisierung von borreichen Boriden und Übergangsmetallboriden, **2008**, Technische Universität Darmstadt.
- [67] H. Haschke, H. Nowotny and F. Benesovsky, *Monatshefte für Chemie und verwandte Teile anderer Wissenschaften* **1966**, 97, 1459-1468.
- [68] M. Kayhan, E. Hildebrandt, M. Frotscher, A. Senyshyn, K. Hofmann, L. Alff and B. Albert, *Solid State Sciences* **2012**, 14, 1656-1659.
- [69] P. W. Anderson, *Journal of Physics and Chemistry of Solids* **1959**, 11, 26-30.
- [70] H. Gou, Z. Wang, J. Zhang, S. Yan and F. Gao, *Inorganic Chemistry* **2008**, 48, 581-587.
- [71] B. Aronsson, M. Bacmann and S. Rundqvist, *Acta Chemica Scandinavica* **1960**, 14, 1001-1005.
- [72] G. K. Strukova, V. F. Degtyareva, D. V. Shovkun, V. N. Zverev, V. M. Kiiko, A. M. Ionov and A. N. Chaika, *arXiv:cond-mat/0105293v1* **2001**.
- [73] A. Kawano, Y. Mizuta, H. Takagiwa, T. Muranaka and J. Akimitsu, *Journal of the Physical Society of Japan* **2003**, 72, 1724-1728.
- [74] M. Frotscher, M. Hölzel and B. Albert, *Zeitschrift Fur Anorganische Und Allgemeine Chemie* **2010**, 636, 1783-1786.
- [75] C. S. Lue, Y. F. Tao and T. H. Su, *Physical Review B* **2008**, 78, 033107.
- [76] B. Andrzejewski, A. Kowalczyk, A. Jezierski, M. R. Lees and G. Chelkowska, *Journal of Alloys and Compounds* **2007**, 442, 225-227.

---

## Curriculum Vitae

### Personal Information

Name: Mehmet Kayhan

Date of Birth: May 4, 1982

Marital Status: Married with one daughter

Adress: Orhaniye Mah. Yagci Ibrahim Sok. No: 7 16400 Inegol-Bursa/TURKEY

### Work experience

- 2006 – 2007 Senior Study at Chemistry Department, Bilkent University, Ankara/Turkey
- 2005 – 2006 Summer Internship at Research and Development Department in Abdi Ibrahim Pharmaceuticals, Istanbul, Turkey
- 2005 – 2006 Internship in Chemistry Department, Bilkent University, Ankara/Turkey
- 2004 – 2005 Summer Internship in Eczacibasi Baxter Pharmaceuticals, Istanbul, Turkey

### Education

08/2013 – till date: Doktor rerum naturalium (Dr. rer. nat.)

“Transition Metal Borides; Synthesis, Characterization and Superconducting Properties”

Technische Universität Darmstadt, Darmstadt Germany

2007 – 2009 Master of Science in Chemistry Department, Middle East Technical University (METU), Ankara/Turkey

“Effects of Synthesis and Doping Methods on Thermoluminescence Glow Curves of Manganese Doped Lithium Tetraborate”

2000 – 2007 Bachelor of Science in Chemistry Department, Bilkent University, Ankara/Turkey

1997-2000 Kutahya Science High School, Kutahya/Turkey

1993-1997 Bursa Inegol Turgutalp Anatolian High School, Bursa/Turkey

1988-1993 Bursa Inegol Gazipasa Primary School, Bursa/Turkey



---

Mehmet Kayhan  
Kaupstrasse 47  
64289, Darmstadt

03/06/2013

### **Eidesstattliche Erklärung**

Ich erkläre hiermit an Eides Statt, dass ich meine Dissertation selbständig und nur mit den angegebenen Hilfsmitteln angefertigt habe.

Mehmet Kayhan

---

Mehmet Kayhan  
Kaupstrasse 47  
64289, Darmstadt

03/06/2013

### Erklärung

Ich erkläre hiermit, noch keinen Promotionsversuch unternommen zu haben.

Mehmet Kayhan